Cold molecular collisions: efficient methods for quantum calculations

JAMES FRANCIS EDWARD CROFT

Cold molecular collisions: efficient methods for quantum calculations

James Francis Edward Croft

Chemistry Department

Durham University

A thesis submitted in partial fulfillment of the requirements for the degree of Ph.D.

2012

Abstract

Multichannel Quantum Defect Theory (MQDT) is shown to be capable of producing quantitatively accurate results for low-energy atom-molecule scattering calculations. With a suitable choice of reference potential and short-range matching distance, it is possible to define a matrix that encapsulates the short-range collision dynamics. Multichannel quantum defect theory can provide an efficient alternative to full coupled-channel calculations for low-energy molecular collisions. However, the efficiency relies on interpolation of the $\boldsymbol{Y}$ matrix that encapsulates the short-range dynamics. It is shown how the phases of the MQDT reference functions may be chosen so as to remove such poles from the vicinity of a reference energy and dramatically increase the range of interpolation. For the test cases of Mg+NH and Li+NH, the resulting optimized $\boldsymbol{Y}$ matrix may be interpolated smoothly over an energy range of several Kelvin and a magnetic field range of over 1000 G. Calculations at additional energies and fields can then be performed at a computational cost that is proportional to the number of channels N and not to N^3. MQDT thus provides a promising method for carrying out low-energy molecular scattering calculations on systems where full exploration of the energy and the field dependence is currently impractical.

Declaration

The material contained within this thesis has not previously been submitted for a degree at the University of Durham or any other university. The research reported within this thesis has been conducted by the author unless indicated otherwise.

Acknowledgements

I would like to thank my supervisor Jeremy Hutson for all of his patience and guidance throughout my Ph.D. I would also like to thank Paul Julienne for his help navigating multichannel quantum defect theory, and the groups of John Doyle and John Bohn for their warm hospitality in Boston and Boulder respectively.

I am grateful to all the members of the Hutson group I have worked with; Jesus Aldegunde, Caroline Blackley, Daniel Brue, Maykel González-Martínez, Ruth Le Sueur, Jesse Lutz, Alisdair Wallis and Piotr Zuchowski.

Finally, I am grateful the EPSRC for funding.

Contents

List of Figures

Chapter 1

Introduction

Absolute zero is as intriguing as it is elusive. As temperatures approach absolute zero, reality becomes increasingly bizarre as quantum mechanics starts to take hold and particles become waves. In this realm, fluids defy gravity, electricity flows without resistance and light can be slowed to a halt (1). The quest to achieve ever lower temperatures has led to the discovery of many fascinating phenomena such as superconductivity (2, 3) and superfluidity (4, 5, 6).

Matter waves are characterized by a de Broglie wavelength which is inversely proportional to the square root of the absolute temperature. If these wavelengths become comparable to or longer than the size or separation of the particles then unique properties emerge. Exactly what happens in this regime is tied to a fundamental property of the particles: their spin. A particle with integer spin is a boson while one with half-integer spin is a fermion. An atom or molecule with an even number of nucleons and electrons is a composite boson and any with an odd number is a composite fermion. In a gas of weakly interacting bosons confined in an external potential, a large fraction of the particles occupy the

lowest quantum state; the wavefunctions of all the individual particles overlap creating a macroscopic quantum state (7, 8). In the corresponding case of weakly interacting fermions, only one particle can fill each state and they each fall to the lowest unoccupied energy state of the trap.

The creation of the first dilute atomic Bose-Einstein condensates (BECs) in 1995 (9, 10) and the corresponding Fermi condensate in 2003 (11, 12) have led to enormous advances in ultracold atomic physics. Trapped ultracold atoms are a quantum system that can be controlled and manipulated with great precision and flexibility. Ultracold atoms in optical lattices can be used as model systems allowing the study of analogue processes such as Anderson localization (13), superfluidity (14) and superconductivity (15). The understanding gained by modeling these processes in the clean controllable environment afforded by cold atoms has the potential to lead to technological advances such as high-temperature superconductors.

1.1 Applications of Cold Molecules

The nascent field of cold and ultracold molecules provides an exciting doorway to explore many varied fields of physics and chemistry.

Cold and ultracold molecules share the controllability and tunable interactions which have made cold atom studies such a fruitful research area, while the richer structure of molecules lend them to many new applications and research directions (16, 17). There is thus great interest in producing samples of cold molecules (at temperatures below 1 K) (18, 19, 20), as well as ultracold molecules (at temperatures below 1 mK) (21, 22, 23, 24).

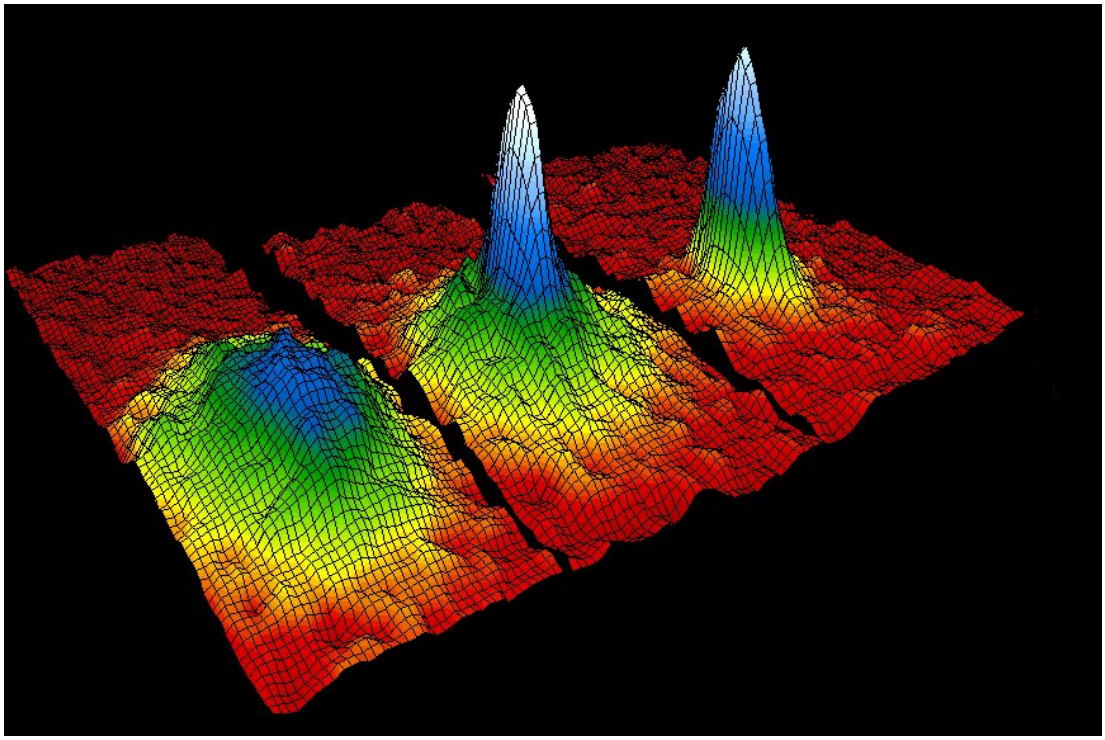

Figure 1.1: Formation of a BEC in a gas of Rb atoms (9). The left panel shows the velocity distribution just before the onset of Bose-Einstein condensation, the middle panel shows the appearance of the condensate, and the right hand panel shows a nearly pure BEC. The image on the right is thus a single macroscopically occupied quantum wave function. Figure taken from the NIST image gallery (http://bec.nist.gov/gallery.html).

Polar molecules are of particular interest since their electric dipole moment allows them to be easily manipulated by external fields. This strong response to a tunable parameter may lead to fully controlled chemistry (25) where every degree of freedom of the reaction can be tuned, thus allowing fundamental insights into chemical reaction processes. Reactions of ultracold $^{40}K^{87}Rb$ in its lowest electronic, vibrational, rotational, and hyperfine energy state have been studied (23) and it was seen that quantum statistics and quantum threshold laws play an important role in determining the rates of inelastic collisions.

The purity and precision control of cold molecular samples makes them an

ideal system for performing high-precision measurements. Cold OH radicals have been used to test predictions of the time-variation of the fine-structure constant (26) while cold YbF has been used to measure a bound on the value of the electric dipole moment of the electron (27). Measurements such as these have important consequences in fundamental physics (28, 29). The existence of an electric dipole moment of the electron would be evidence of a breakdown of time-reversal symmetry.

Cold molecules in a lattice provide a physical model of strongly interacting quantum particles, in which the interactions can be controlled. The interaction between cold polar molecules is both long-range and anisotropic and leads to fundamentally new condensed-matter phases unobservable in lattices of cold atomic gases (30). Cold molecules in a regular array also provide a testbed for quantum information processing and quantum computing (31). The development of a quantum computer would allow certain problems to be solved much faster than any classical computer (32).

1.2 Producing Cold Molecules

It was the advent of laser cooling in the 1980s that led to the production of cold and ultracold atomic samples (33, 34, 35). Laser cooling requires a closed absorption-emission cycle that limits its application to a selection of atomic species, predominantly within the group of alkali metals. The complex internal structure of other atoms and almost all molecules makes laser cooling all but impossible. Although there are exceptions such as strontium monoflouride (SrF) (36), this approach will probably never be applicable to the wide array of

molecules of interest.

The production of cold molecules therefore requires a new approach and progress has taken two main routes: direct and indirect cooling methods. Indirect methods seek to form cold molecules from an already cold atomic gas (21). This method has seen significant success, and in 2003 several groups succeeded in producing ultracold molecules from atomic gas samples by magneto-association (37, 38, 39, 40). Vibrational levels embedded in a continuum are quasi-bound and a Feshbach resonance (41) occurs when this quasi-bound molecular level crosses an atomic threshold as a function of the magnetic field. Magneto-association makes use of these Feshbach resonances to convert pairs of atoms in molecules. Coupled pairs of atoms are converted into molecules by sweeping the magnetic field adiabatically across the Feshbach resonance, as shown in figure 1.2.

While magneto-association has been the most successful method of producing cold molecules, the first successful approach actually used photoassociation (42). Photoassociation proceeds by exciting an unbound scattering state of two atoms to a bound excited molecular level. This unstable excited molecule then spontaneously decays into a stable ground state molecule (43). Weakly bound molecules formed by indirect methods require coherent laser techniques to transfer the molecules to their ground state (22, 44, 45).

Indirect methods have been successful, but they can only produce molecules comprised of atomic species that it is possible to cool to ultracold temperatures. Currently this is mostly limited to the alkali metals and alkaline earths (although this list is increasing all the time). It is therefore desirable to develop direct methods which take molecules of our own choosing and directly cool them. A number of such methods have been developed, including buffer-gas cooling, which takes

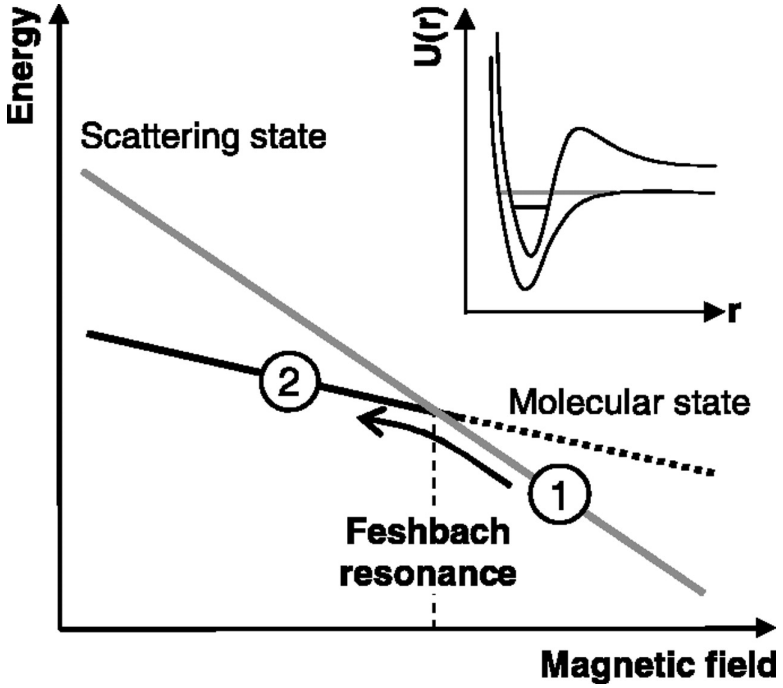

Figure 1.2: A Feshbach resonance occurs when the Zeeman energy of the atomic scattering state becomes equal to that of a molecular bound state as a function of magnetic field due to the difference in their magnetic moments. The threshold of the open channel is shown in grey while the bound state of closed channel is shown in black. Molecules can be created from the BEC by a sweep of the magnetic field across the resonance from high field to low field. The inset shows the potential energy, U, as a function of the interatomic distance, r, for the 2 states. Image from (38).

advantage of elastic collisions between a molecule of interest and cryogenic helium gas to cool a sample (46). Deceleration methods, such as Stark deceleration (47) and Zeeman deceleration (48), use inhomogeneous electric and magnetic fields respectively to slow molecules. These methods generally produce cold molecules with temperatures between 10 mK and 1 K, which means a second-stage cooling method is needed to bring the molecules into the ultracold regime.

Sympathetic cooling, in which the molecules are allowed to thermalize with a gas of ultracold atoms, is a promising second-stage cooling method (49). While

elastic collisions allow thermalization, inelastic collisions can cause trap loss (50). For many systems, inelastic collision rates are predicted to be too large for sympathetic cooling to succeed (51, 52, 53). Quantum-mechanical molecular collision calculations however can be computationally extremely expensive. This thesis investigates efficient methods of performing quantum calculations for cold molecular collisions.

Chapter 2

Scattering Theory

Understanding atomic and molecular interactions and collisions is essential to the study of cold and ultracold molecules. For example, methods such as buffer-gas cooling (46) and Stark deceleration (47) can produce cold molecules with temperatures between 10 mK and 1 K. However, a second-stage cooling method is needed to bring the molecules into the ultracold regime. Sympathetic cooling, in which the molecules are allowed to thermalize with a gas of ultracold atoms, is a promising second-stage cooling method (49). However, while elastic collisions allow thermalization, inelastic collisions can cause trap loss (50), and for many systems the inelastic collisions are predicted to be too large for sympathetic cooling to succeed (51, 52, 53). Scattering calculations are essential in order to identify systems for which sympathetic cooling has a good prospect of success. Once in the ultracold regime, the extent to which atomic and molecular interactions can be controlled again depends on a detailed understanding of their collisional properties.

Quantum molecular scattering calculations are usually carried out using the

coupled-channel method: the Schrödinger equation for scattering is converted into a set of coupled differential equations, which are then propagated across a range of values of the intermolecular distance r. The size of the problem is determined by the number of channels N (the number of coupled equations). The usual algorithms take a time proportional to N^3, since each step of the propagation requires an $\mathcal{O}(N^3)$ matrix operation.

Cold molecule scattering presents problems with a large number of channels for two reasons:

1. At very low energies, small splittings between molecular energy levels become important. This makes it necessary to include fine details of molecular energy level patterns, such as tunneling (52) and nuclear hyperfine splitting (51, 54). The extra degrees of freedom require additional basis functions; in particular, including nuclear spins can multiply the number of equations by a substantial factor (sometimes 100 or more).

2. Collisions in the presence of electric and magnetic fields are very important. In an applied field, the total angular momentum J is no longer a good quantum number (55, 56). Because of this, the large sets of coupled equations can no longer be factorized neatly into smaller blocks for each J as is possible in field-free scattering (57).

In addition, in cold molecule applications it is often necessary to repeat scattering calculations on a fine grid of energies and/or applied electric and magnetic fields, which adds greatly to the computational expense.

Cold atomic and molecular collisions and near-threshold bound states are conveniently described by a set of coupled equations. The Hamiltonian for an

interacting pair of atoms or molecules is of the form

$$-\frac{\hbar^2}{2\mu}\nabla^2 + \hat{H}_{\rm int}(\tau) + V(r,\tau), \tag{2.1}$$

where μ is the reduced mass, ∇^2 is the Laplacian for the intermolecular coordinates, and τ denotes all coordinates except the interparticle distance r. $\hat{H}_{\rm int}(\tau)$ represents the internal Hamiltonians of the two particles and $V(r,\tau)$ is the interaction potential. The total wavefunction is expanded

$$\Psi(r,\tau) = r^{-1}\sum_i \varphi_i(\tau)\psi_i(r), \tag{2.2}$$

where the N functions $\varphi_i(\tau)$ form a basis set for the motion in all coordinates, τ, except the intermolecular distance, and $\psi_i(r)$ is the radial wavefunction in channel i. Substituting this expansion into the total time-independent Schrödinger equation and projecting onto the basis function $\varphi_j(\tau)$ yields the usual coupled equations of scattering theory,

$$\left[-\frac{\hbar^2}{2\mu}\frac{d^2}{dr^2} - E\right]\psi_j(r) = -\sum_i W_{ji}(r)\psi_i(r), \tag{2.3}$$

where E is the energy. The coupling matrix $\boldsymbol{W}$ has elements

$$W_{ji}(r) = \int \varphi_j^*(\tau) \quad \left[\hat{H}_{\rm int}(\tau) + V(r,\tau) + \frac{\hbar^2 L_i(L_i+1)}{2\mu r^2}\right]\varphi_i(\tau)\, d\tau, \tag{2.4}$$

where L_i is the partial-wave quantum number for channel i. Equation 2.3 can

conveniently be written in matrix form,

$$\frac{\hbar^2}{2\mu}\frac{d^2\boldsymbol{\psi}}{dr^2} = [\boldsymbol{W}(r) - E\boldsymbol{I}]\boldsymbol{\psi}(r), \tag{2.5}$$

where $\boldsymbol{\psi}(r)$ is a column vector made up of the solutions $\psi_i(r)$ and $\boldsymbol{I}$ is the identity matrix.

For both bound states and collision calculations, the wavefunction must be regular at the origin. When $V(r) \gg 0$ as $r \to 0$, the short-range boundary condition is

$$\psi_i(r) \to 0 \quad \text{as} \quad r \to 0. \tag{2.6}$$

At any energy, there are N linearly independent solution vectors $\boldsymbol{\psi}(r)$ that satisfy these boundary conditions, and it is convenient to combine them to form the $N \times N$ wavefunction matrix $\boldsymbol{\Psi}$(r).

The coupled-channel approach propagates either the wavefunction matrix $\boldsymbol{\Psi}(r)$ and its derivative $\boldsymbol{\Psi}'(r)$, or the log-derivative matrix $\boldsymbol{L}(r) = \boldsymbol{\Psi}'[\boldsymbol{\Psi}]^{-1}$, outwards from $r = 0$ (or a point in the deeply classically forbidden region at short range) (58, 59). In scattering calculations, the propagation is continued to a point $r_{\max}$ at large r. The wavefunction or log-derivative matrix is then transformed into a representation where $\boldsymbol{W}$ is asymptotically diagonal (60), such that

$$W_{ji}(r) \overset{r\to\infty}{\longrightarrow} \left[E_i^\infty + \frac{\hbar^2 L_i(L_i+1)}{2\mu r^2}\right]\delta_{ij} + \mathcal{O}(r^{-n}), \tag{2.7}$$

where n is the power of the leading term in the potential expansion and E_i^∞ is the threshold of channel i. Each channel is either asymptotically open, $E \geq E_i^\infty$,

or asymptotically closed, $E < E_i^\infty$. The scattering boundary conditions are

$$\boldsymbol{\Psi} = \boldsymbol{J}(r) + \boldsymbol{N}(r)\boldsymbol{K}. \tag{2.8}$$

The matrices $\boldsymbol{J}$ and $\boldsymbol{N}$ are diagonal (59). The matrix elements of the open channels are Riccati-Bessel functions (61)

$$[J(r)]_{ij} = \delta_{ij} r k_j^{1/2} j_{L_j}(k_j r) \tag{2.9}$$

$$[N(r)]_{ij} = \delta_{ij} r k_j^{1/2} n_{L_j}(k_j r) \tag{2.10}$$

and the matrix elements for the closed channels are made up of modified spherical Bessel functions of the first and third kinds (61)

$$[J(r)]_{ij} = \delta_{ij} (r k_j)^{-1/2} I_{L_{j+\frac{1}{2}}}(k_j r) \tag{2.11}$$

$$[N(r)]_{ij} = \delta_{ij} (r k_j)^{-1/2} K_{L_{j+\frac{1}{2}}}(k_j r) \tag{2.12}$$

where k_i is the asymptotic wave vector,

$$k_i = \sqrt{\frac{2\mu}{\hbar^2}(E - E_i^\infty)}. \tag{2.13}$$

The Ricatti-Bessel functions and the modified spherical Bessel functions are solutions of equation 2.3 with no potential but including the centrifugal barriers. Therefore at sufficiently long-range once the potential has become negligible the propagated wavefunction ψ can be written as a linear combination as in equation 2.8. Using Bessel functions instead of sines and cosines includes the effect of the centrifugal terms in $\boldsymbol{W}(r)$ and allows the boundary conditions to be applied at

much shorter range. The asymptotic forms of Ricatti-Bessel functions are

$$J_{ij}(R) \overset{r\to\infty}{\longrightarrow} k_j^{-1/2} \sin(kr - \frac{L_j\pi}{2}), \tag{2.14}$$

$$N_{ij}(R) \overset{r\to\infty}{\longrightarrow} k_j^{-1/2} \cos(kr - \frac{L_j\pi}{2}). \tag{2.15}$$

Instead of expressing the boundary conditions in terms of trigonometric functions they can be expressed in terms of incoming (e^{ikR}) and outgoing waves (e^{-ikR}),

$$\xi_{ij} = J_{ij} - iN_{ij}, \tag{2.16}$$

$$\zeta_{ij} = J_{ij} + iN_{ij}. \tag{2.17}$$

Expressing the wavefunction in this way corresponds to the physical problem we are interested in. An incoming wave in a single channel j, corresponding to the incident particles, and outgoing waves in all open channels, corresponding to scattered particles. The asymptotic wavefunction can thus be expressed as

$$\Psi(r,\tau) \overset{r\to\infty}{\longrightarrow} r^{-1} \left[\phi_j(\tau) k_j^{-1/2} e^{-ik_j r + iL_j\pi/2} + \sum_i S_{ji}\phi_i(\tau) k_i^{-1/2} e^{-ik_j r + iL_j\pi/2}\right] \tag{2.18}$$

where the sum runs over open channels only. Equation 2.18 corresponds to a single incoming channel, but we can combine the set of solutions for each incoming channel into a single $\boldsymbol{S}$ matrix. Every physical property related to completed collisions can be obtained from the $\boldsymbol{S}$ matrix. The $\boldsymbol{S}$ matrix is an $N_\mathrm{o} \times N_\mathrm{o}$ complex symmetric matrix, where N_o is the number of open channels. It is unitary, that is, $\boldsymbol{S}\boldsymbol{S}^\dagger = \boldsymbol{I}$, where $\boldsymbol{S}^\dagger$ indicates the Hermitian conjugate and $\boldsymbol{I}$ is a unit matrix. The scattering $\boldsymbol{S}$ matrix is related to the open-open submatrix of

$\boldsymbol{K}$ by

$$\boldsymbol{S} = (1 + i\boldsymbol{K}_{\mathrm{oo}})^{-1}(1 - i\boldsymbol{K}_{\mathrm{oo}}). \tag{2.19}$$

The $\boldsymbol{S}$ matrix contains the coefficients of the outgoing wave. The fraction of the initial unit incoming flux from i leaving in channels $j \neq i$ is given by the T-matrix,

$$T_{ij} = \delta_{ij} - S_{ij}. \tag{2.20}$$

In cold collision studies, the scattering $\boldsymbol{S}$ matrix is often a fast function of collision energy E and magnetic field B, with extensive structure due to scattering resonances and discontinuous behavior at threshold. The entire propagation to long range must thus be repeated over a fine grid of energies and/or applied electric and magnetic fields, and this further multiplies the computational expense.

2.1 Scattering Cross-sections

The $\boldsymbol{S}$ matrix contains all the scattering information for the system. Observables of the collision process, e.g. state-to-state cross sections and rate constants, can be obtained from it.

For a collision of two particles initially in internal state i, where i specifies the states of both particles, the angle between the initial and final relative velocities v and v' is given by spherical polar coordinates Θ and Φ, where Θ is the deflection angle in the center of mass frame. The differential cross-section is defined as the ratio between the well-defined flux I_i of the incoming beam of particles in state

i with the flux I_j of particles in state j after the collision,

$$\frac{d\sigma_{ij}}{d\omega} = \frac{I_j}{I_i}, \tag{2.21}$$

where ω is an element of solid angle at deflection angle Θ. The flux I_j is a function of the deflection angle Θ and is different for each final state j. Integrating the differential cross section gives the integral scattering cross-section from state i to state j,

$$\sigma_{ij} = \int_0^{2\pi} \int_0^{\pi} \frac{d\sigma_{ij}}{d\omega} \sin\Theta d\Theta d\Phi. \tag{2.22}$$

There can be many channels i, with different orbital angular momentum L_i, which correspond to the same final state α of the colliding pair. We thus define a set of channels which all correspond to a single quantum state of the monomer as $i \in \alpha$. The integral cross-section for a transition from a molecule to go from state α to state β can be obtained from the $\boldsymbol{S}$ matrix elements,

$$\sigma_{\alpha\beta} = \frac{\pi}{k_i^2} \sum_{i\in\alpha, j\in\beta} g_i |\delta_{ij} - S_{ij}|^2. \tag{2.23}$$

The factor g_i is a function of the channel quantum numbers and the particular channel basis set in use.

2.2 Propagation Methods

There are many propagators that take account of the special properties of equation 2.3. A number of them were used to obtain the results contained within this thesis and those are discussed here.

2.2.1 Numerov

In the course of performing MQDT calculations single channel wavefunction solutions to equation 2.3 need to be obtained. The work in this thesis has used the Numerov method for this purpose (62, 63). Expanding $\psi(r)$ as a Taylor series we obtain

$$\psi_{i-1} + \psi_{i+1} = \sum_{k=0}^{\infty} \frac{2h^{2k}}{2k!} \psi_i^{[2k]}, \tag{2.24}$$

where the odd terms have canceled out and,

$$\psi^{[n]} = \frac{d^n \psi}{dr^n}. \tag{2.25}$$

The simplest method of propagation simply drops all terms above second order and substituting into equation 2.3 we obtain,

$$\psi_i = \frac{\psi_{i-1} + \psi_{i+1}}{h^2(W_i - E) + 2} + \mathcal{O}(h^4) \tag{2.26}$$

which has local error of fourth order in the step size, h. The Numerov method obtains a more accurate solution, with local error of sixth order in the step size by defining

$$X_i = \psi_i - \frac{h^2}{12} \psi^{[2]}. \tag{2.27}$$

Using equations 2.24 and 2.3 equation 2.27 can be written as,

$$X_i = [1 - \frac{h^2}{12}(W_i - E)]\psi_i \tag{2.28}$$

$$= [1 - T_i]\psi_i, \tag{2.29}$$

where $T_i = -\frac{h^2}{12}(W_i - E)$, we obtain the three term recurrence relation,

$$(1 - T_{n+1})\psi_{n+1} - (2 + 10T_n)\psi_i + (1 - T_{n-1})\psi_{n-1} = 0. \tag{2.30}$$

Using equation 2.28 this can be expressed explicitly in terms of ψ,

$$\psi_{i+i} = \frac{(2 - \frac{5h^2}{6}W_i)\psi_i - (2 - \frac{h^2}{12}W_{i-1})\psi_{i-1}}{1 + \frac{h^2}{12}W_{i+1}} + \mathcal{O}(h^6) \tag{2.31}$$

The Numerov method is the highest order three-point method possible and has local error of sixth order in the step size.

The derivative of the wave function at any point r_i is given by

$$\psi_i^{[1]} = h^{-1}[(1/2 - T_{n+1})\psi_{n+1} - (1/2 - T_{n-1})\psi_{n-1}], \tag{2.32}$$

with an error term of $\mathcal{O}(h^5)$ (64).

2.2.2 Renormalized Numerov

Methods, such as the Numerov method, which explicitly propagate the wavefunction become unstable in the classically forbidden region. The renormalized Numerov method avoids propagating the wavefunction, instead propagating the ratio of the wavefunction at neighboring points which does not grow exponentially in classically forbidden regions (63). Substituting 2.28 into 2.30 we obtain

$$X_{n+1} - U_n X_n + X_{n+1} = 0, \tag{2.33}$$

where

$$U_n = (1 - T_n)^{-1}(2 + 10T_n). \tag{2.34}$$

Defining the ratio between X_{n+1} and X_n as

$$R_n = X_{n+1}/X_n, \tag{2.35}$$

the three term recurrence relation can then be written as a two term recurrence relation

$$R_n = U_n - R_{n-1}^{-1}. \tag{2.36}$$

By propagating the ratio the wavefunction at successive points the renormalized Numerov method avoids propagating an exponentially growing function in classically forbidden regions. The actual wavefunction can be recovered by keeping track of the ratio and applying the correct normalizations at each point.

2.2.3 Log-derivative

Like the renormalized Numerov method the log-derivative method avoids propagating the actual wavefunction and instead propagates,

$$\boldsymbol{L}(r) = \boldsymbol{\Psi}'[\boldsymbol{\Psi}]^{-1} \tag{2.37}$$

which has the advantage of not growing exponentially in classically forbidden regions and thus being more numerically stable (59, 65, 66). Substituting 2.37

into 2.5 gives the first-order matrix Ricatti equation,

$$\boldsymbol{L}'(R) = \boldsymbol{W}(R) - E\boldsymbol{I} - \boldsymbol{L}^2(R). \tag{2.38}$$

The $\boldsymbol{K}$ matrix can be obtained from $\boldsymbol{L}$ asymptotically by solving the linear series of equations,

$$(\boldsymbol{LJ} - \boldsymbol{J}') = (\boldsymbol{LN} - \boldsymbol{N}')\boldsymbol{K}. \tag{2.39}$$

Chapter 3

Multichannel Quantum Defect Theory

Multichannel Quantum Defect Theory (MQDT) offers an alternative to full coupled-channel calculations. It was originally developed to provide a uniform treatment of bound and scattering states for problems involving the interaction of an electron with an ion core (67, 68), but was subsequently generalized to handle a range of other long-range potentials (68, 69, 70, 71, 72, 73). It has been successfully applied to scattering problems as diverse as negative ion photodetachment (74), near-threshold predissociation of diatomic molecules (71, 75) and predissociation of atom-diatom Van der Waals complexes (76, 77). More recently it has been applied to ultracold collisions between pairs of neutral atoms (78, 79, 80, 81, 82), between atoms and ions (83, 84), and between highly reactive molecules (85, 86, 87).

MQDT can be viewed in two different ways. The first tries to capture the important physics of collisions within a few analytic quantum defect parameters. The other views it as a method for solving the coupled equations of scattering

theory which offers substantial insights and advantages in efficiency. The common feature of the two approaches is to take advantage of the enormous difference in energy and length scales associated with separated collision partners and short-range potentials.

When MQDT is viewed as a numerical method for solving the coupled differential equations, the goal is to obtain a matrix $\boldsymbol{Y}(E, B)$ (70, 75, 80, 81) that completely describes the short-range dynamics and is insensitive to collision energy E and magnetic field B. This matrix can be obtained once and then used for calculations over a wide range of energies and fields, or obtained by interpolation from a few points. MQDT achieves this by defining $\boldsymbol{Y}(E, B)$ at relatively short range, as described below. The threshold behavior is accounted for from properties of single channels. Once the matrix $\boldsymbol{Y}(E, B)$ has been obtained, the time required for calculations at additional energies and fields is only proportional to N, not N^3.

Understanding threshold atomic physics in quantum defect terms is well developed (78, 79, 80, 88, 89). Threshold bound-state and scattering properties are determined mainly by the long-range potential, which can often be approximated as $-C_n/r^n$. For the case of the Van der Waals interaction, $-C_6/r^6$, the linearly independent pair of solutions for a single potential is known (90). An analytic approach to MQDT using these solutions has been developed (91, 92) and gives much insight into ultracold atom-atom collisions (93).

This thesis investigates the use of MQDT as a numerical method to study cold atom-molecule collisions. MQDT also begins by propagating the wavefunction or log-derivative matrix outwards from short range. However, instead of continuing to $r_{\max}$, matching takes place at a point r_{match}, at relatively short range. The

matching in MQDT treats the open and weakly closed channels on an equal footing; weakly closed channels are usually defined as those that are locally open, $E > W_{ii}(r)$, at some value of r, so are capable of supporting scattering resonances. Matching at short range produces a matrix $\boldsymbol{Y}(E, B)$ that is relatively insensitive to energy and applied field, as described below. $\boldsymbol{Y}$ also varies smoothly across thresholds, unlike $\boldsymbol{S}$ and $\boldsymbol{K}$. Provided the channels are uncoupled outside r_{match}, it is then possible to obtain the scattering $\boldsymbol{S}$ matrix from $\boldsymbol{Y}$ using the properties of individual uncoupled channels.

We consider a problem with N_{o} open channels and N_{c} weakly closed channels at some collision energy E and field B. For each such channel, $i = 1, N$, where $N = N_{\mathrm{o}} + N_{\mathrm{c}}$, MQDT requires a reference potential, $U_i^{\mathrm{ref}}(r)$, which asymptotically has similar behavior to $W_{ii}(r)$ in equation 2.7. This reference potential defines a linearly independent pair of reference functions $f_i(r)$ and $g_i(r)$,

$$\left[\frac{d^2}{dr^2} + K_i^2(r)\right] f_i(r) = 0, \tag{3.1}$$

and similarly for g_i, where the local wave vector $K_i(r)$ is

$$K_i(r) = \sqrt{\frac{2\mu}{\hbar^2}(E - U_i^{\mathrm{ref}}(r))}. \tag{3.2}$$

The regular solution f_i has the boundary condition $f_i \to 0$ as $r \to 0$. f_i and g_i are normalized to have Wentzel-Kramers-Brillouin (WKB) form, with amplitude $K_i(r)^{-1/2}$, at some point in the classically allowed region (70).

The $N \times N$ matrix $\boldsymbol{Y}$ is defined by matching at r_{match},

$$\boldsymbol{\Psi} = \boldsymbol{f}(r) + \boldsymbol{g}(r)\boldsymbol{Y}, \tag{3.3}$$

or in terms of the log-derivative matrix $\boldsymbol{L}$,

$$(\boldsymbol{Lf} - \boldsymbol{f'}) = (\boldsymbol{Lg} - \boldsymbol{g'})\boldsymbol{Y}, \tag{3.4}$$

where $\boldsymbol{f}$ and $\boldsymbol{g}$ are diagonal matrices containing the functions f_i and g_i and the primes indicate radial derivatives.

In order to relate $\boldsymbol{Y}$ to the physical scattering $\boldsymbol{S}$ matrix, the asymptotic forms of the reference functions f_i and g_i in each channel are required. To this end another pair of reference functions is defined for each channel. For open channels, these functions are asymptotically energy-normalized,

$$s_i(r) \overset{r\to\infty}{\longrightarrow} k_i^{-\frac{1}{2}} \sin\left(k_i r - \frac{L_i\pi}{2} + \xi_i\right), \tag{3.5}$$

$$c_i(r) \overset{r\to\infty}{\longrightarrow} k_i^{-\frac{1}{2}} \cos\left(k_i r - \frac{L_i\pi}{2} + \xi_i\right), \tag{3.6}$$

where ξ_i is the phase shift associated with reference potential i and k_i is the asymptotic wave vector,

$$k_i = \sqrt{\frac{2\mu}{\hbar^2}(E - E_i^\infty)}. \tag{3.7}$$

These asymptotically normalized functions are related to f_i and g_i through the quantum defect parameters C_i and $\tan\lambda_i$,

$$s_i(r) = C_i^{-1} f_i(r); \tag{3.8}$$

$$c_i(r) = C_i[g_i(r) + \tan\lambda_i f_i(r)]. \tag{3.9}$$

Thus C_i relates the amplitudes of the energy-normalised reference functions to WKB-normalised ones, while $\tan\lambda_i$ describes the modification in phase due to

threshold effects. Far from threshold, $C_i \approx 1$ and $\tan\lambda_i \approx 0$.

For each weakly closed channel, an exponentially decaying solution is defined,

$$\phi_i(r) \overset{r\to\infty}{\longrightarrow} \tfrac{1}{2} e^{-|k_i|r}\sqrt{|k_i|}. \tag{3.10}$$

This is related to the solutions f_i and g_i by a normalization factor $\mathcal{N}_i$, and an energy-dependent phase ν_i,

$$\phi_i(r) = \mathcal{N}_i \left[\cos\nu_i f_i(r) - \sin\nu_i g_i(r)\right]. \tag{3.11}$$

The phase ν_i is an integer multiple of π at each energy that corresponds to a bound state of the reference potential in channel i.

The $\boldsymbol{Y}$ matrix is converted into the $\boldsymbol{S}$ matrix of scattering theory using the quantum defect parameters C_i, $\tan\lambda_i$, $\tan\nu_i$ and ξ_i. First, the effect of coupling to closed channels is accounted for,

$$\overline{\boldsymbol{Y}} = \boldsymbol{Y}_{\mathrm{oo}} - \boldsymbol{Y}_{\mathrm{oc}}[\tan\boldsymbol{\nu} + \boldsymbol{Y}_{\mathrm{cc}}]^{-1}\boldsymbol{Y}_{\mathrm{co}}, \tag{3.12}$$

where $\tan\boldsymbol{\nu}$ is a diagonal matrix of dimension $N_{\mathrm{c}} \times N_{\mathrm{c}}$ containing elements $\tan\nu_i$. The $N_{\mathrm{o}} \times N_{\mathrm{o}}$ matrix $\overline{\boldsymbol{Y}}$ incorporates any resonance structure caused by coupling to closed channels through $\tan\boldsymbol{\nu}$. Unlike $\boldsymbol{Y}$ itself, $\overline{\boldsymbol{Y}}$ can be a rapidly varying function of energy and field. Secondly, threshold effects from asymptotically open channels are incorporated,

$$\overline{\boldsymbol{R}} = \boldsymbol{C}^{-1}\left[\overline{\boldsymbol{Y}}^{-1} - \tan\boldsymbol{\lambda}\right]^{-1}\boldsymbol{C}^{-1}, \tag{3.13}$$

where $\boldsymbol{C}$ and $\tan\boldsymbol{\lambda}$ are diagonal matrices of dimension $N_\mathrm{o} \times N_\mathrm{o}$, containing elements C_i and $\tan\lambda_i$. Finally, the $\boldsymbol{S}$ matrix is obtained from

$$\boldsymbol{S} = e^{i\boldsymbol{\xi}} \left[1 + i\overline{\boldsymbol{R}}\right] \left[1 - i\overline{\boldsymbol{R}}\right]^{-1} e^{i\boldsymbol{\xi}}. \tag{3.14}$$

This may be compared to equation 2.18 for the full coupled-channel method. The inclusion of the diagonal matrix $e^{i\boldsymbol{\xi}}$ accounts for the phase difference between the reference functions f_i and g_i used by MQDT and the Riccati-Bessel functions used by the full coupled-channel method.

The approach taken in this thesis is somewhat different from that in refs. (71, 80). There MQDT was approached as an exact representation of the full coupled-channel solution. The matrix $\boldsymbol{Y}$ was evaluated at a distance r_match large enough that it had become constant as a function of r_match. When this is done, MQDT gives the same (exact) results for any choice of reference potential $U_i^\mathrm{ref}(r)$, although constancy of $\boldsymbol{Y}$ may be achieved at different values of r_match for different choices. In our approach, r_match is chosen to ensure that $\boldsymbol{Y}$ is only weakly energy-dependent, and this may require matching in a region where $\boldsymbol{Y}$ is not yet independent of r_match. With this approach, MQDT provides an *approximate* solution whose quality depends on the choice of reference potentials.

3.1 Numerical evaluation of reference functions and quantum defect parameters

3.1.1 Open channels

For an open channel i, the reference function s_i is obtained by propagating a regular solution of 3.1 from a point inside r_{match} to a point $r_{\max}$ at long range and imposing the boundary condition 3.5 (or its Bessel function equivalent). This establishes the normalization of s_i and also gives the phase shift ξ_i, which is then used to obtain the function c_i at $r_{\max}$ from the boundary condition 3.6. The reference function c_i is then propagated inwards to r_{match}. The two remaining quantum defect parameters are obtained by applying (71)

$$C_i^{-2} = (s_i^2 K_i + s_i'^2/K_i) \tag{3.15}$$

and

$$\cot \lambda_i = \frac{K_i(\gamma_i - u_i)}{K_i^2 + \gamma_i u_i} \tag{3.16}$$

in the classically allowed region, where $\gamma_i = s_i'/s_i$ and $u_i = c_i'/c_i$. The primes indicate radial derivatives. Equations 3.8 and 3.9 then give the reference functions f_i and g_i.

3.1.2 Closed channels

For a weakly closed channel i, the reference function f_i is again obtained by propagating a regular solution of 3.1 outwards from a point inside r_{match}, but in

this case f_i is normalized in the classically allowed region such that

$$f_i^2(K_i^2 + \gamma_i^2) = K_i. \tag{3.17}$$

In the closed-channel case, g_i cannot be obtained directly from f_i at a single point. Instead, the reference function ϕ_i is obtained by using 3.10 as a long-range boundary condition and propagating a solution of 3.1 inwards towards $r = 0$. The normalization factor $\mathcal{N}_i$ of equation 3.11 is obtained by matching to

$$\mathcal{N}_i^2 = (\phi_i^2 K_i + \phi_i'^2/K_i). \tag{3.18}$$

in the classically allowed region. The quantum defect parameter $\tan\nu_i$ is then obtained from

$$\tan\nu_i = \frac{K_i(t_i - \gamma_i)}{K_i^2 + \gamma_i t_i}, \tag{3.19}$$

where $t_i = \phi_i'/\phi_i$. Finally, the function g_i is obtained from f_i and ϕ_i using equation 3.11.

3.2 Sources of Error

There are a number of sources of errors in MQDT calculations using our approach:

1. Interchannel couplings that occur outside r_{match}, which are not taken into account by equations 3.12 to 3.14;

2. Deviations between the reference potentials $U_i^{\text{ref}}(r)$ and $W_{ii}(r)$ outside r_{match};

3. Differences between the actual $\boldsymbol{Y}$ matrix at a given energy and field and

the $\boldsymbol{Y}$ matrix obtained by interpolation.

3.3 Rotating reference functions

The absolute phases chosen for the reference functions f_i and g_i are arbitrary, and different choices produce different $\boldsymbol{Y}$ matrices and different MQDT parameters. In particular, equation 3.3 shows that a pole in $\boldsymbol{Y}$ occurs whenever the propagated multichannel wavefunction in any channel i has no contribution from the reference function f_i. However, all phase choices produce the same physical $\boldsymbol{S}$ matrix. We are therefore free to choose the phase in order to produce a $\boldsymbol{Y}$ matrix with advantageous characteristics.

Rotating the reference functions f_i and g_i by an angle θ_i gives a new set of linearly independent reference functions $\bar{f}_i$ and $\bar{g}_i$,

$$\begin{pmatrix} \bar{f}_i \\ \bar{g}_i \end{pmatrix} = \begin{pmatrix} \cos\theta_i & -\sin\theta_i \\ \sin\theta_i & \cos\theta_i \end{pmatrix} \begin{pmatrix} f_i \\ g_i \end{pmatrix}. \tag{3.20}$$

These rotated reference functions define a new $\boldsymbol{Y}$ matrix and a new set of QDT parameters ($\bar{C}$, $\tan\bar{\lambda}$, $\bar{\xi}$ and $\tan\bar{\nu}$).

The rotated QDT parameters can be obtained from the unrotated QDT parameters and the rotation angle. In the open channels the reference functions are asymptotically related to Ricatti-Bessel functions $J_{L_i}(r)$ and $N_{L_i}(r)$ (59),

$$\begin{pmatrix} f_i \\ g_i \end{pmatrix} = \begin{pmatrix} C_i & 0 \\ -C_i\tan\lambda_i & C_i^{-1} \end{pmatrix} \begin{pmatrix} \cos\xi_i & \sin\xi_i \\ -\sin\xi_i & \cos\xi_i \end{pmatrix} \begin{pmatrix} J_{L_i} \\ N_{L_i} \end{pmatrix}. \tag{3.21}$$

In the weakly closed channels the reference functions are asymptotically

$$\begin{pmatrix} f_i \\ g_i \end{pmatrix} = \begin{pmatrix} \cos\nu_i & \sin\nu_i \\ -\sin\nu_i & \cos\nu_i \end{pmatrix} \begin{pmatrix} \phi_i \\ \gamma_i \end{pmatrix}, \tag{3.22}$$

where ϕ_i is the solution of equation 3.1 that decays exponentially at large r and γ_i is its linearly independent partner, which is exponentially growing. Combining equations 3.21, 3.22 and 3.20 gives

$$\bar{\xi}_i = \arctan\left[\frac{C_i^2 \sin\xi_i(\cos\theta_i + \tan\lambda_i \sin\theta_i) - \cos\xi_i \sin\theta_i}{C_i^2 \cos\xi_i(\cos\theta_i + \tan\lambda_i \sin\theta_i) + \sin\xi_i \sin\theta_i}\right], \tag{3.23}$$

$$\tan\bar{\lambda}_i = -\frac{2C_i^4 \tan\lambda_i \cos 2\theta_i + \left[1 + C_i^4\left(\tan^2\lambda_i - 1\right)\right]\sin 2\theta_i}{2\left(C_i^4 \cos^2\theta_i + \sin\theta_i\left[\sin\theta_i + C_i^4 \tan\lambda_i(2\cos\theta_i + \tan\lambda_i \sin\theta_i)\right]\right)}, \tag{3.24}$$

$$\begin{aligned} \bar{C}_i &= \left(\frac{\sin\xi_i \sin\theta_i}{C_i} + C_i \cos\xi_i(\cos\theta_i + \tan\lambda_i \sin\theta_i)\right) \\ &\times \sqrt{1 + \frac{\left(\cos\xi_i \sin\theta_i - C_i^2 \sin\xi_i(\cos\theta_i + \tan\lambda_i \sin\theta_i)\right)^2}{\left(\sin\xi_i \sin\theta_i + C_i^2 \cos\xi_i(\cos\theta_i + \tan\lambda_i \sin\theta_i)\right)^2}}, \end{aligned} \tag{3.25}$$

$$\bar{\nu}_i = \nu_i - \theta_i. \tag{3.26}$$

Far from threshold ($E \gg 1$ K), equations 3.23 to 3.26 simplify to $\bar{\xi}_i = \xi_i - \theta_i$, $\tan\lambda_i \approx 0$, $C_i \approx 1$ and $\bar{\nu}_i = \nu_i - \theta_i$. However, in the threshold region that is of interest in cold molecule studies, equations 3.23 to 3.26 must be evaluated explicitly. Figure 3.1 shows C^{-2} (upper panel) and $\tan\lambda$ (lower panel) as a function of θ obtained by the application of equations 3.25 and 3.24 respectively for representative QDT parameters at four different energies. Tuning θ_i by π tunes the reference function f_i through a shape resonance in channel i producing

a peak in the upper panel showing C^{-2}.

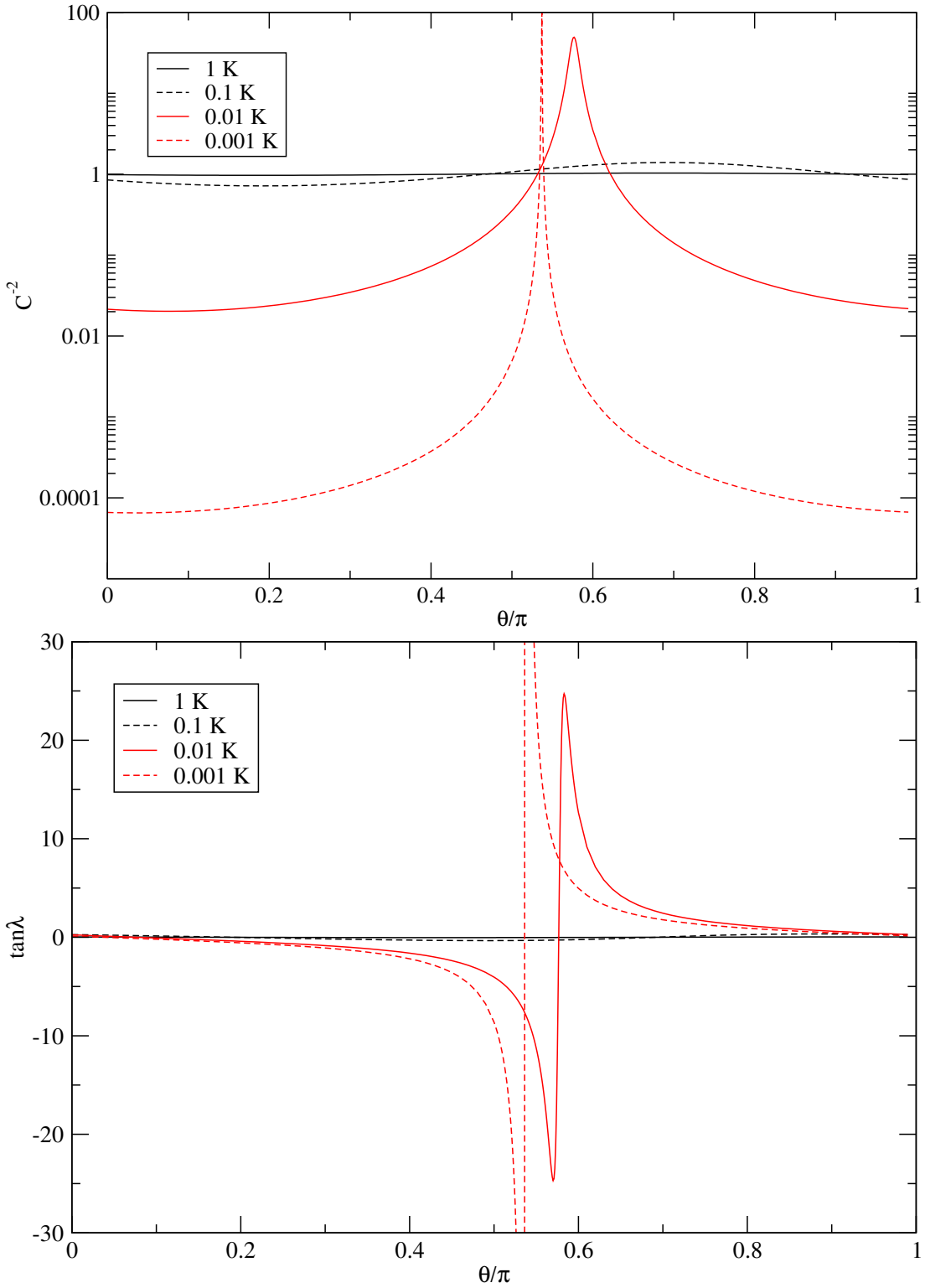

Figure 3.1: C^{-2} (upper panel) and $\tan\lambda$ (lower panel) as a function of θ obtained by the application of equations 3.25 and 3.24 respectively at four different energies.

Chapter 4

Collisions of ^1S Atoms with $^3\Sigma$ Molecules

To explore the application of MQDT to cold molecular collisions, we consider the prototype system Mg(^1S)+NH($^3\Sigma^-$). The internal Hamiltonian for collisions of ^1S atoms with $^3\Sigma$ molecules are described in this chapter. The Hamiltonian in Jacobi coordinates (r, θ) is

$$\hat{H} = -\frac{\hbar^2}{2\mu} r^{-1} \frac{d^2}{dr^2} r + \frac{\hat{L}^2}{2\mu r^2} + \hat{H}_{\rm mon} + \hat{H}_{\rm Z} + V(r, \theta), \tag{4.1}$$

where $\hat{L}^2$ is the space-fixed operator for end-over-end rotation, $\hat{H}_{\rm mon}$ is the Hamiltonian for the NH monomer, $\hat{H}_{\rm Z}$ is the Zeeman interaction and $V(R, \theta)$ is the intermolecular potential. In all the work in this thesis the NH molecule is treated as a rigid rotor. This simplification is valid as the low collision energies considered in this thesis are orders of magnitude smaller than the energy separation of vibrational levels of the NH molecule. The monomer Hamiltonian for NH is

therefore given by

$$\hat{H}_{\text{mon}} = \hbar^{-2} b_{\text{NH}} \hat{N}^2 + \hat{H}_{\text{SN}} + \hat{H}_{\text{SS}}, \tag{4.2}$$

where $b_{\text{NH}} = 16.343$ cm^{-1} is the rotational constant of NH in its ground vibrational level (94). The spin-rotation operator is given by

$$\hat{H}_{\text{SN}} = \gamma \hat{N} \cdot \hat{S}. \tag{4.3}$$

The spin-spin operator written in space-fixed coordinates is given by

$$\hat{H}_{\text{SS}} = \frac{2}{3} \lambda_{\text{SS}} \left[\frac{4\pi}{5} \right]^{\frac{1}{2}} \sqrt{6} \sum_q (-1)^q Y_{2-q}(\hat{r}) \left[S \otimes S \right]_q^{(2)}, \tag{4.4}$$

where $\hat{N}$ and $\hat{S}$ are the rotational and spin angular momenta operators. The numerical values for the spin-rotation and spin-spin constants are $\gamma = -0.0055$ cm^{-1} and $\lambda_{\text{SS}} = 0.920$ cm^{-1} (95).

In this work two basis sets are used to expand the eigenfunctions of Eq. (4.1), referred to as the *coupled* and *uncoupled* basis sets. Common to both schemes the end-over-end rotation of the collision partners is represented by quantum numbers $|LM_L\rangle$, where L is the rotational quantum number and M_L is its projection onto the space-fixed Z axis.

In the uncoupled representation, we use basis functions $|nm_n\rangle|sm_s\rangle|LM_L\rangle$, where the quantum numbers n and s describe the rotation and electron spin of the NH molecule. The corresponding m quantum numbers are the projections onto the space-fixed Z axis. In the coupled representation, we use basis functions $|nsjm_j\rangle|LM_L\rangle$, where j is the vector sum of n and s and m_j is the projection of j onto the space-fixed Z axis.

4.1 Matrix elements of the Hamiltonian

The matrix elements shown in this section are given in (60). In both basis sets the matrix elements of $\hat{L}^2$ and the rotational part of the monomer Hamiltonian are diagonal, and are simply given by $\hbar^2 L(L+1)$ and $b_{\mathrm{NH}} n(n+1)$ respectively. The other matrix elements of the NH monomer Hamiltonian in both the *coupled* and *uncoupled* basis sets are as follows.

4.1.1 Spin-rotation interaction

The matrix elements for the interaction between the magnetic moments caused by the molecular rotation and the electron spin are given by

$$\begin{aligned}
\langle s m_s | \langle n m_n | \hat{H}_{\mathrm{SN}} | n' m_n' \rangle | s m_s' \rangle &= \delta_{nn'} \delta_{m_n m_n'} \delta_{m_s m_s'} \gamma m_n m_s \qquad (4.5)\\
&+ \left(\delta_{nn'} \delta_{m_n m_n' \pm 1} \delta_{m_s m_s' \mp 1} \right) \frac{\gamma}{2} \left[n(n+1) - m_n'(m_n' \pm 1) \right]^{\frac{1}{2}} \\
&\times \left[s(s+1) - m_s'(m_s' \mp 1) \right]^{\frac{1}{2}} , \\
\langle n s j m_j | \hat{H}_{\mathrm{SN}} | n' s j' m_j' \rangle &= \delta_{nn'} \delta_{jj'} \delta_{m_j m_j'} \gamma (-1)^{n+j+s} \left[n(n+1)(2n+1) s(s+1)(2s+1) \right]^{\frac{1}{2}} \\
&\times \begin{Bmatrix} s & n & j \\ n & s & 1 \end{Bmatrix} . \qquad (4.6)
\end{aligned}$$

4.1.2 Spin-spin interaction

The matrix elements for the interaction between the two unpaired electrons in a $^3\Sigma$ molecule are given by

$$\begin{aligned}\langle sm_s|\langle nm_n|\hat{H}_{\rm SS}|n'm'_n\rangle|sm'_s\rangle &= \frac{2\sqrt{30}}{3}\lambda_{\rm SS}(-1)^{s-m_s-m_n} \\ &\times [(2n+1)(2n'+1)]^{\frac{1}{2}}\,[s(s+1)(2s+1)] \\ &\times \begin{pmatrix} n & 2 & n' \\ 0 & 0 & 0 \end{pmatrix} \begin{Bmatrix} 1 & 1 & 2 \\ s & s & s \end{Bmatrix} \\ &\times \sum_q (-1)^q \begin{pmatrix} n & 2 & n' \\ -m_n & -q & m'_n \end{pmatrix} \begin{pmatrix} s & 2 & s \\ -m_s & q & m'_s \end{pmatrix}, \end{aligned} \tag{4.7}$$

$$\begin{aligned}\langle nsjm_j|\hat{H}_{\rm SS}|n'sj'm'_j\rangle &= \delta_{jj'}\delta_{m_jm'_j}\frac{2\sqrt{30}}{3}\lambda_{\rm SS}(-1)^{j+n'+n+s}\,[(2n+1)(2n'+1)]^{\frac{1}{2}} \\ &\times \begin{pmatrix} n & 2 & n' \\ 0 & 0 & 0 \end{pmatrix} \begin{Bmatrix} s & n' & j \\ n & s & 2 \end{Bmatrix}. \end{aligned} \tag{4.8}$$

4.1.3 Zeeman splitting

The interaction between the NH molecule and the magnetic field is given by

$$\hat{H}_{\rm Z} = g_{\rm e}\mu_{\rm B}\hat{B}\cdot\hat{S}, \tag{4.9}$$

where $g_{\rm e}$ is the g-factor for the electron, $\mu_{\rm B}$ the Bohr magneton and $\hat{B}$ is the magnetic field vector. Rotational and anisotropic spin terms have been neglected (96). The matrix elements of this operator in the uncoupled representation are

diagonal

$$\langle sm_s|\langle nm_n|\hat{H}_{\rm Z}|n'm'_n\rangle|sm'_s\rangle = \delta_{nn'}\delta_{m_n m'_n}\delta_{m_s m'_s} g_{\rm e}\mu_{\rm B} B m_s, \tag{4.10}$$

and off-diagonal in the coupled representation

$$\begin{aligned}\langle nsjm_j|\hat{H}_{\rm Z}|n'sj'm'_j\rangle &= \delta_{nn'}\delta_{m_j m'_j} g_{\rm e}\mu_{\rm B} B(-1)^{n+s-m_j+1} \\ &\times [s(s+1)(2s+1)(2j+1)(2j'+1)]^{\frac{1}{2}} \\ &\times \begin{pmatrix} j & 1 & j' \\ -m_j & 0 & m_j \end{pmatrix} \begin{Bmatrix} s & j' & n \\ j & s & 1 \end{Bmatrix}.\end{aligned} \tag{4.11}$$

The magnetic field direction has been chosen as the Z axis and B is the field strength.

4.1.4 Expansion of the Potential

The potential energy surface for the NH molecule and the Mg atom can be expanded in terms of Legendre polynomials,

$$V(r,\theta) = \sum_{\lambda} V_\lambda(r) P_\lambda(\cos\theta). \tag{4.12}$$

This expansion is convenient since the matrix elements of the Legendre polynomials in the coupled and uncoupled basis sets are given by

$$\begin{aligned}\langle LM_L|\langle nsjm_j| \quad P_\lambda(\cos\theta) \quad |n'sj'm'_j\rangle|L'M'_L\rangle \qquad (4.13)\\ = \quad [(2n+1)(2n'+1)(2j+1)(2j'+1)(2L+1)(2L'+1)]^{\frac{1}{2}}\\ \times \quad \begin{pmatrix} n & \lambda & n' \\ 0 & 0 & 0 \end{pmatrix} \begin{pmatrix} L & \lambda & L' \\ 0 & 0 & 0 \end{pmatrix} \sum_{m_\lambda} (-1)^{s+j+j'+\lambda+m_\lambda-M_L-m_j}\\ \times \quad \begin{pmatrix} L & \lambda & L' \\ -M_L & -m_\lambda & M'_L \end{pmatrix} \begin{pmatrix} j & \lambda & j' \\ -m_j & m_\lambda & m'_j \end{pmatrix} \begin{Bmatrix} j & j' & \lambda \\ n' & n & s \end{Bmatrix}\end{aligned}$$

and

$$\begin{aligned}\langle LM_L|\langle sm_s|\langle nm_n| \quad P_\lambda(\cos\theta) \quad |n'm'_n\rangle|sm'_s\rangle|L'M'_L\rangle \qquad (4.14)\\ = \quad \delta_{m_s m'_s}\,[(2n+1)(2n'+1)(2L+1)(2L'+1)]^{\frac{1}{2}}\\ \times \quad \begin{pmatrix} n & \lambda & n' \\ 0 & 0 & 0 \end{pmatrix} \begin{pmatrix} L & \lambda & L' \\ 0 & 0 & 0 \end{pmatrix} \sum_{m_\lambda} (-1)^{m_\lambda-M_L-m_n}\\ \times \quad \begin{pmatrix} L & \lambda & L' \\ -M_L & -m_\lambda & M'_L \end{pmatrix} \begin{pmatrix} n & \lambda & n' \\ -m_n & m_\lambda & m'_n \end{pmatrix}.\end{aligned}$$

these are off-diagonal in both representations.

Chapter 5

Multichannel quantum defect theory for cold molecular collisions

To explore the application of MQDT to cold molecular collisions, we consider the prototype system Mg+NH($^3\Sigma^-$). The potential energy surface for this system is moderately anisotropic (97) and provides substantial coupling between channels. The system is topical because Wallis and Hutson (98) have shown that sympathetic cooling of cold NH molecules by ultracold Mg atoms has a good prospect of success. The NH radical is a polar, paramagnetic, and chemically reactive species with two stable isotopes, fermionic ^{14}NH and bosonic ^{15}NH.

The energy levels of NH in a magnetic field, shown in figure 5.1, are most conveniently described using Hund's case (b), in which the molecular rotation n couples to the spin s to produce a total monomer angular momentum j. In zero field, each rotational level n is split into sublevels labeled by j. In a magnetic

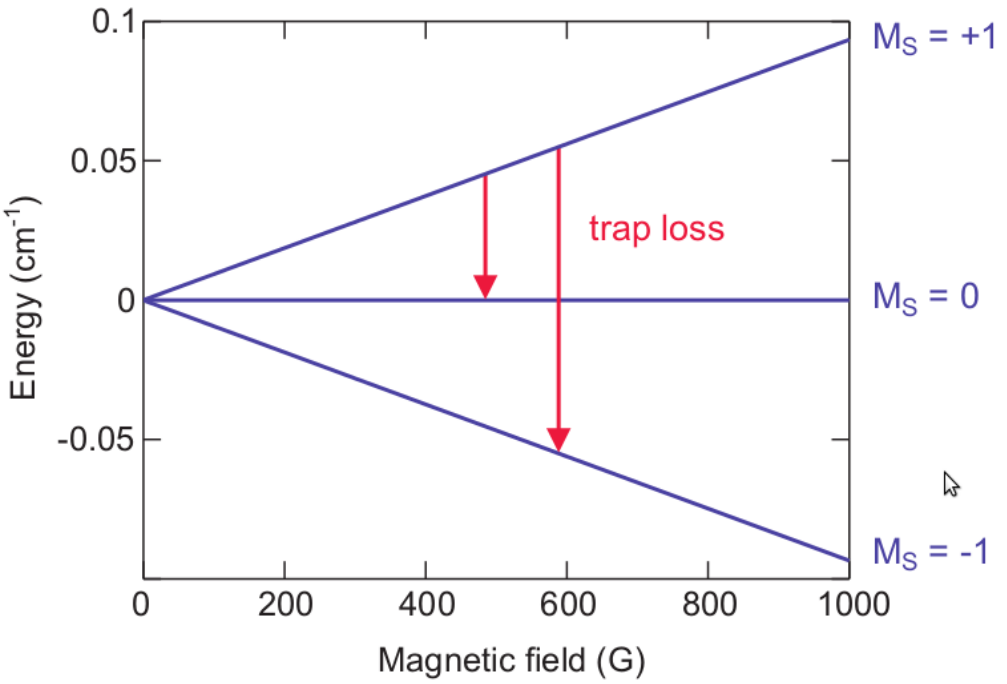

Figure 5.1: the Zeeman diagram for the triplet ground state of NH. The low-field-seeking $m_j = +1$ state is magnetically trappable while the states with $m_j = 0$ or 1 cannot be confined in the trap. Figure taken from (99).

field, each sublevel splits further into $2j + 1$ levels labeled by m_j, the projection of j onto the axis defined by the field. For the $n = 0$ levels that are of most interest for cold molecule studies, there is only a single zero-field level with $j = 1$ that splits into three components with $m_j = +1$, 0 and -1.

The coupled equations are constructed in a partly coupled basis set $|nsjm_j\rangle|LM_L\rangle$, where L is the end-over-end rotational angular momentum of the Mg atom and the NH molecule about one another and M_L is its projection on the axis defined by the magnetic field. Hyperfine structure is neglected. The matrix elements of the total Hamiltonian in this basis given in chapter 4. The only good quantum

numbers during the collision are the parity $p = (-1)^{n+L+1}$ and the total projection quantum number $M = m_j + M_L$. The calculations in the present work are performed for $p = -1$ and $M = 1$. This choice includes s-wave scattering of NH molecules in initial state $m_j = +1$, which is magnetically trappable, to $m_j = 0$ and -1, which are not. The basis set used included all functions up to $n_{\max} = 1$ and $L_{\max} = 3$. This unconverged basis set is sufficient for the purpose of comparing MQDT results with full coupled-channel calculations.

5.1 Numerical methods

The coupled-channel calculations required for both MQDT and the full coupled-channel approach were carried out using the MOLSCAT package (100), as modified to handle collisions in magnetic fields (60). The coupled equations were solved numerically using the hybrid log-derivative propagator of Alexander and Manolopoulos (66), which uses a fixed-step-size log-derivative propagator in the short-range region ($r_{\min} \leq r < r_{\mathrm{mid}}$) and a variable-step-size Airy propagator in long-range region ($r_{\mathrm{mid}} \leq r \leq r_{\max}$). The full coupled-channel calculations used $r_{\min} = 2.5$ Å, $r_{\mathrm{mid}} = 50$ Å and $r_{\max} = 250$ Å (where 1 Å $= 10^{-10}$ m). MQDT requires coupled-channel calculations only from $r_{\min}$ to r_{match} (which is less than r_{mid}), so only the fixed-step-size propagator was used in this case.

The MQDT reference functions and quantum defect parameters were obtained as described in section 3.1, using the Numerov propagator (62) to solve the 1-dimensional Schrödinger equations. Use of the renormalized Numerov method (63) was not found to be necessary in the present case. The MQDT $\boldsymbol{Y}$ matrix was then obtained by matching to the log-derivative matrix extracted from the

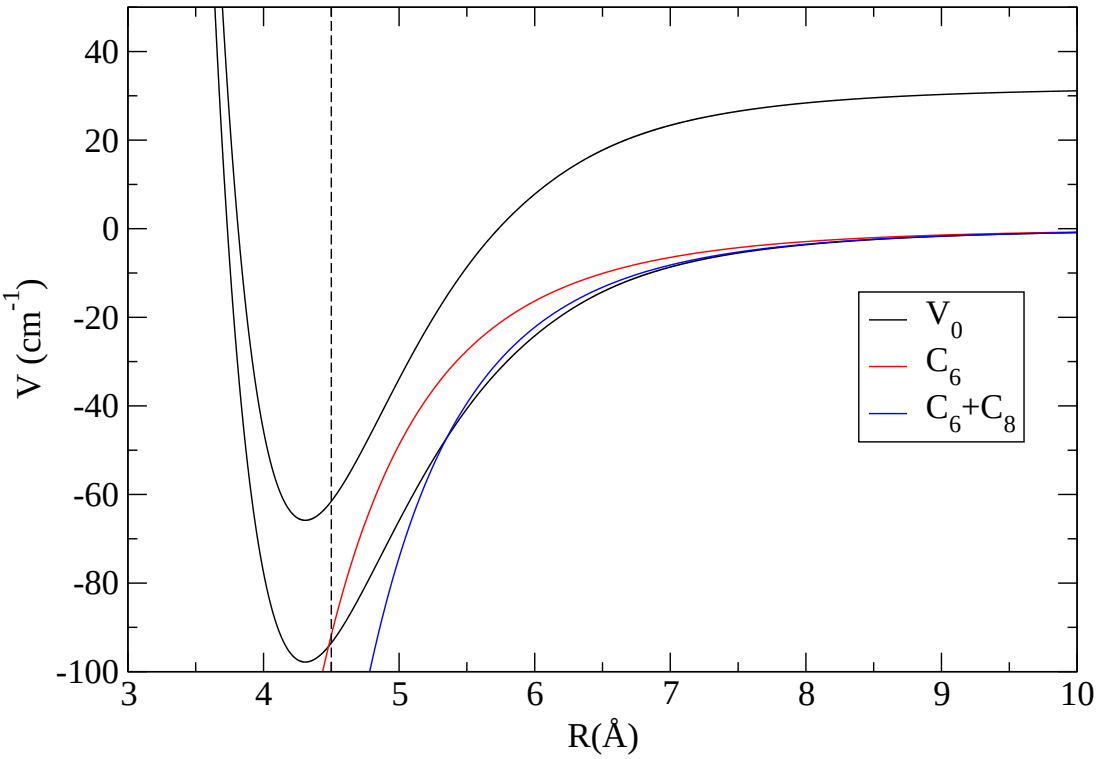

Figure 5.2: Zero-field reference potentials. For the V_0 reference potential the first rotational excited state is also shown ($n = 1$). The hard wall at $r = 4.5$ Å is shown as a dashed line.

coupled-channel propagation at a distance r_{match}.

The potential energy surface used in this work was calculated by Soldán *et al.* using SAPT(DFT) (97).

5.2 Comparison of full coupled-channel and MQDT results

5.2.1 Choice of r_{match} and reference potential

One of the goals of MQDT is to obtain a matrix $\boldsymbol{Y}(E, B)$ in such a way that it is only weakly dependent on energy E and magnetic field B. However, the actual form of $\boldsymbol{Y}(E, B)$ is strongly dependent on the distance at which it is defined and the reference potentials used. In the present work we consider three different reference potentials, as shown in Figure 5.2. First we define a reference potential containing a pure C_6 long-range term, which has been used with great success in cold atom-atom collisions,

$$U_i^{\mathrm{ref},C_6}(r) = -\frac{C_6}{r^6} + \frac{\hbar^2 L_i(L_i+1)}{2\mu r^2} + E_i^{\infty}, \tag{5.1}$$

where $C_6 = 7.621 \times 10^5$ Å^6 cm^{-1} for Mg+NH (97). Secondly we define a reference potential containing an additional C_8 term,

$$U_i^{\mathrm{ref},C_{6,8}}(r) = -\frac{C_6}{r^6} - \frac{C_8}{r^8} + \frac{\hbar^2 L_i(L_i+1)}{2\mu r^2} + E_i^{\infty}, \tag{5.2}$$

where $C_8 = 9.941 \times 10^6$ Å^8 cm^{-1} (97). Finally we define

$$U_i^{\mathrm{ref},V_0}(r) = V_0(r) + \frac{\hbar^2 L_i(L_i+1)}{2\mu r^2} + E_i^{\infty}, \tag{5.3}$$

where $V_0(r)$ is the isotropic part of the interaction potential. Each reference potential contains a hard wall at $r = r_i^{\mathrm{wall}}$, so that $U_i^{\mathrm{ref}}(r) = \infty$ for $r < r_i^{\mathrm{wall}}$. This

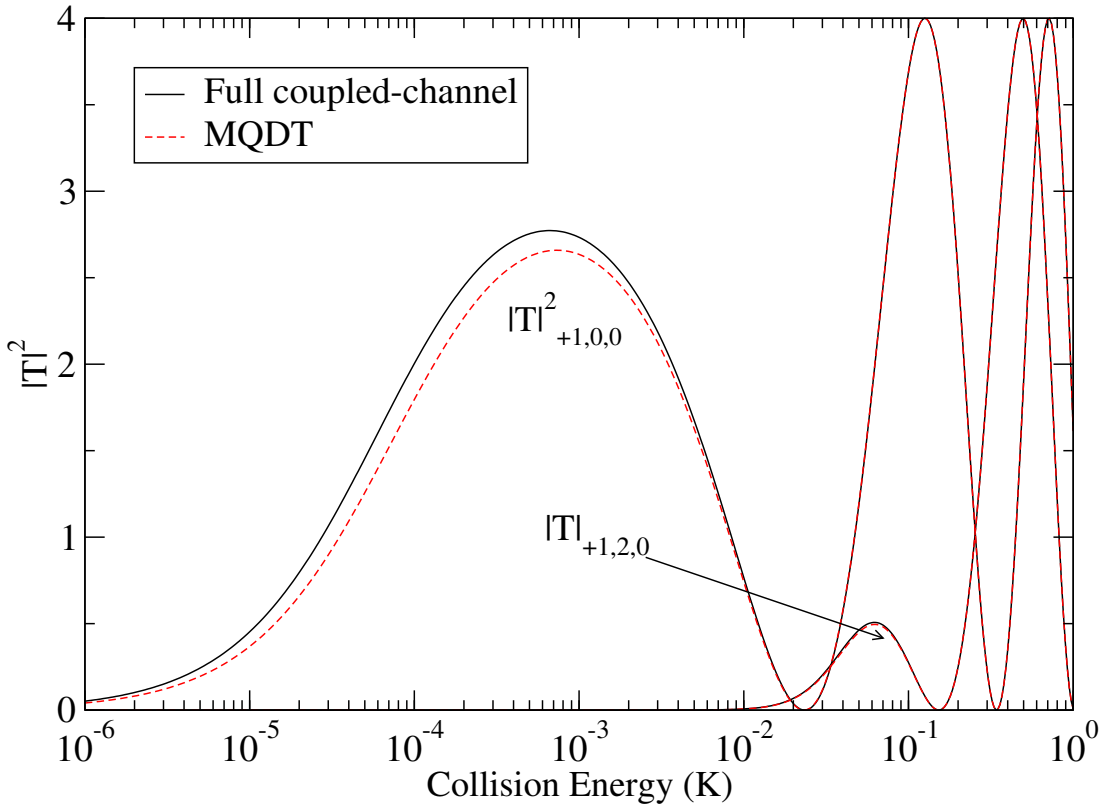

Figure 5.3: The squares of diagonal T-matrix elements in the incoming channels for $m_j = +1$, $L = 0$ and 2 at $B = 10$ G, obtained from full coupled-channel calculations (solid, black) and MQDT with the C_6 reference potential and $r_{\mathrm{match}} = 20$ Å (dashed, red). T-matrix elements are labeled with quantum numbers m_j, L, M_L.

allows the phase ξ_i of the reference functions in each channel to be adjusted if required.

It is convenient to compare MQDT and coupled-channel results at the level of T-matrix elements, $T_{ij} = \delta_{ij} - S_{ij}$. In general we label elements $T_{\alpha,L,M_L \to \alpha',L',M_L'}$, where $|\alpha\rangle = |nsjm_j\rangle$. However, the collisions considered here are all among the $n = 0, j = 1$ levels and so α is simply abbreviated to m_j. The spin-changing cross sections are quite small except near resonances, so we focus mostly on diagonal elements, for which we suppress the second set of labels.

Figure 5.3 compares diagonal T-matrix elements $|T_{ii}|^2$ obtained from full

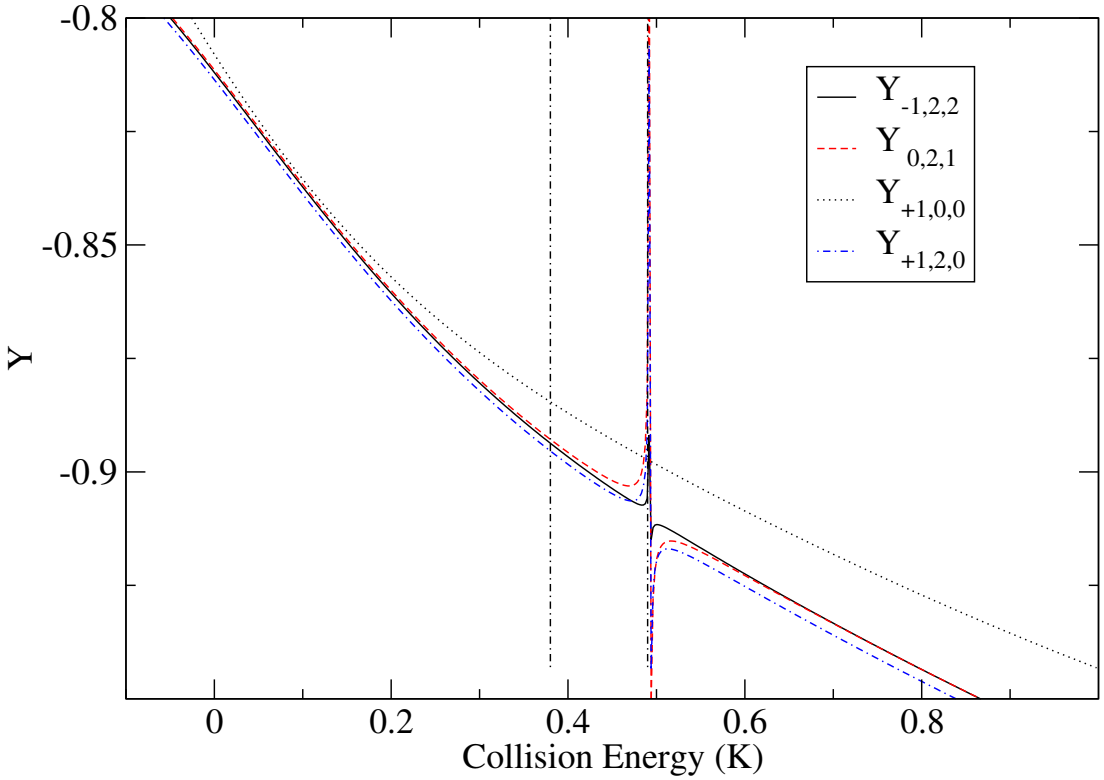

Figure 5.4: Diagonal $\boldsymbol{Y}$ matrix elements as a function of collision energy at $B = 10$ G for the C_6 reference potential with $r_{\mathrm{match}} = 20$ Å. The dashed vertical lines show the positions of quasibound states as described in the text.

coupled-channel calculations with those from the MQDT method for the pure C_6 reference potential of equation 5.1, with a matching distance of $r_{\mathrm{match}} = 20$ Å. The $\boldsymbol{Y}$ matrix was recalculated at every energy at which full coupled-channel calculations were performed. The MQDT results reproduce the coupled-channel results almost exactly at collision energies $E/k_{\mathrm{B}} > 10$ mK. However, at lower energies the results start to differ noticeably. It may be noted that $|U_i^{\mathrm{ref},C_6} - W_{ii}|/k_{\mathrm{B}} \approx 0.6$ mK at $r_{\mathrm{match}} = 20$ Å.

Figure 5.4 shows the diagonal $\boldsymbol{Y}$ elements corresponding to Figure 5.3. They vary smoothly across most of the energy range, and are continuous across the threshold at zero energy, but exhibit occasional sharp structures as a function of

energy. These sharp features are close to the energies of quasibound states, as shown by carrying out bound-state calculations using the BOUND package (101), with the same basis set as the MOLSCAT calculations. The resulting bound-state energies are shown in Figure 5.4 as dashed vertical lines. The broad feature near $E/k_{\mathrm{B}} = 0.5$ K is due to a quasibound state (Feshbach resonance) with quantum numbers $n = 1$, $j = 0$, $m_j = 0$, $L = 3$.

For MQDT to be more efficient than full coupled-channel calculations, it needs to produce results in agreement with full coupled-channel calculations from an energy-insensitive $\boldsymbol{Y}$ matrix that can be assumed to be constant or can be obtained by interpolation from a few energies, instead of being recalculated at every energy. However, the $\boldsymbol{Y}$ matrix elements in Figure 5.4 do not meet this requirement: the resonant features prevent reliable interpolation over useful ranges of energy.

The energy sensitivity of the $\boldsymbol{Y}$ matrix in Figure 5.4 is due to the value used for r_{match}. When r_{match} is large, resonance features due to quasibound states may be present in the log-derivative matrix from which $\boldsymbol{Y}$ is obtained. In this case the open and closed-channel blocks of $\boldsymbol{Y}$ are uncoupled, so that $\bar{\boldsymbol{Y}} \approx \boldsymbol{Y}_{\mathrm{oo}}$, and the resonances appear through the $\boldsymbol{Y}_{\mathrm{oo}}$ term in Eq. 3.12 rather than through $\tan\boldsymbol{\nu} + \boldsymbol{Y}_{\mathrm{cc}}$ (102). However, if r_{match} is small enough, the resonance features are shifted to high energies, out of the region of interest. It is usually desirable to obtain $\boldsymbol{Y}$ at a value of r_{match} that is in or near the classically allowed region for all weakly closed channels. However it must be remembered that the MQDT method neglects interchannel couplings that occur outside r_{match}, so there is always a tradeoff between choosing a value that minimizes the energy-dependence and one that takes account of coupling at relatively long range. This is particularly important

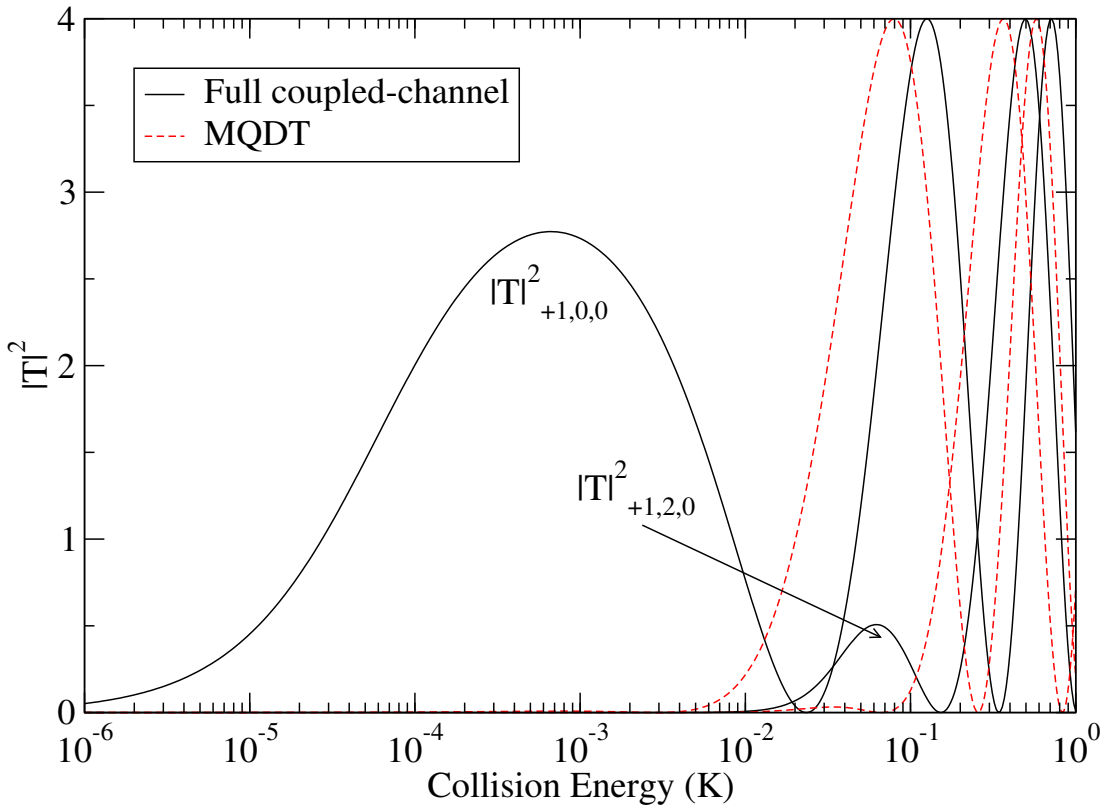

Figure 5.5: The squares of diagonal T-matrix elements in the incoming channels for $m_j = +1$, $L = 0$ and 2 at $B = 10$ G, obtained from full coupled-channel calculations (solid, black) and MQDT with the C_6 reference potential and $r_{\mathrm{match}} = 6.8$ Å (dashed, red).

in molecular scattering, where the anisotropy of the interaction potential often provides substantial couplings at long range.

It is convenient to consider lengths and energies in ultracold scattering in relation to the Van der Waals characteristic length and energy, defined by (103)

$$r_{\mathrm{VdW}} = \frac{1}{2}\left(\frac{2\mu C_6}{\hbar^2}\right)^{\frac{1}{4}} \quad \text{and} \quad E_{\mathrm{VdW}} = \frac{\hbar^2}{2\mu r_{\mathrm{VdW}}^2}. \tag{5.4}$$

For Mg+NH, $r_{\mathrm{VdW}} = 12.7$ Å and $E_{\mathrm{VdW}}/k_{\mathrm{B}} = 11$ mK. In atomic systems, it is common to place r_{match} close to r_{VdW}. However, the quasibound state responsible

for the broad feature in Figure 5.4 is due to an $n = 1$ state, with an outer turning point around 5.7 Å. The resonant feature therefore does not shift in energy significantly until r_{match} is around 7 Å. In addition, it is not enough simply to move r_{match} to short range with the same reference function. Figure 5.5 shows diagonal T-matrix elements obtained by MQDT with the C_6 reference function, as in Figure 5.3, but with $r_{\mathrm{match}} = 6.8$ Å. This does indeed produce a $\boldsymbol{Y}$ matrix without poles in the energy region of interest, but the MQDT results are no longer in agreement with the full coupled-channel results at any of the energies considered. This is because the difference between the reference potential and the diagonal $\boldsymbol{W}$ matrix elements at $r_{\mathrm{match}} = 6.8$ Å is $|U_i^{\mathrm{ref},C_6} - W_{ii}|/k_{\mathrm{B}} \approx 4$ K, as seen in Figure 5.2. Alternatively, in terms of the approach of Mies and Raoult (80), 6.8 Å is too short a distance for the $\boldsymbol{Y}$ matrix evaluated with the C_6 reference potential to have reached its asymptotic value.

This problem may be remedied by using a better reference potential. Figure 5.6 shows results obtained using the reference potentials of equations 5.2 and 5.3, again for $r_{\mathrm{match}} = 6.8$ Å. The $C_6 + C_8$ reference potential gives a marked improvement over the pure C_6 reference potential. The $\boldsymbol{T}$ matrix elements it produces follow the form of the full coupled-channel results but become worse at energies much below 1 K: at $r_{\mathrm{match}} = 6.8$ Å, $|U_i^{\mathrm{ref},C_6+C_8} - W_{ii}|/k_{\mathrm{B}} \approx 0.35$ K. However, the results obtained with the V_0 reference potential are more accurate, and can scarcely be distinguished from the full coupled-channel results in Figure 5.6.

Even the V_0 reference potential does not produce exact results. Figure 5.7 shows the ratio of the MQDT T-matrix elements for this reference potential to the full coupled-channel results. The poles in the ratio arise simply because MQDT

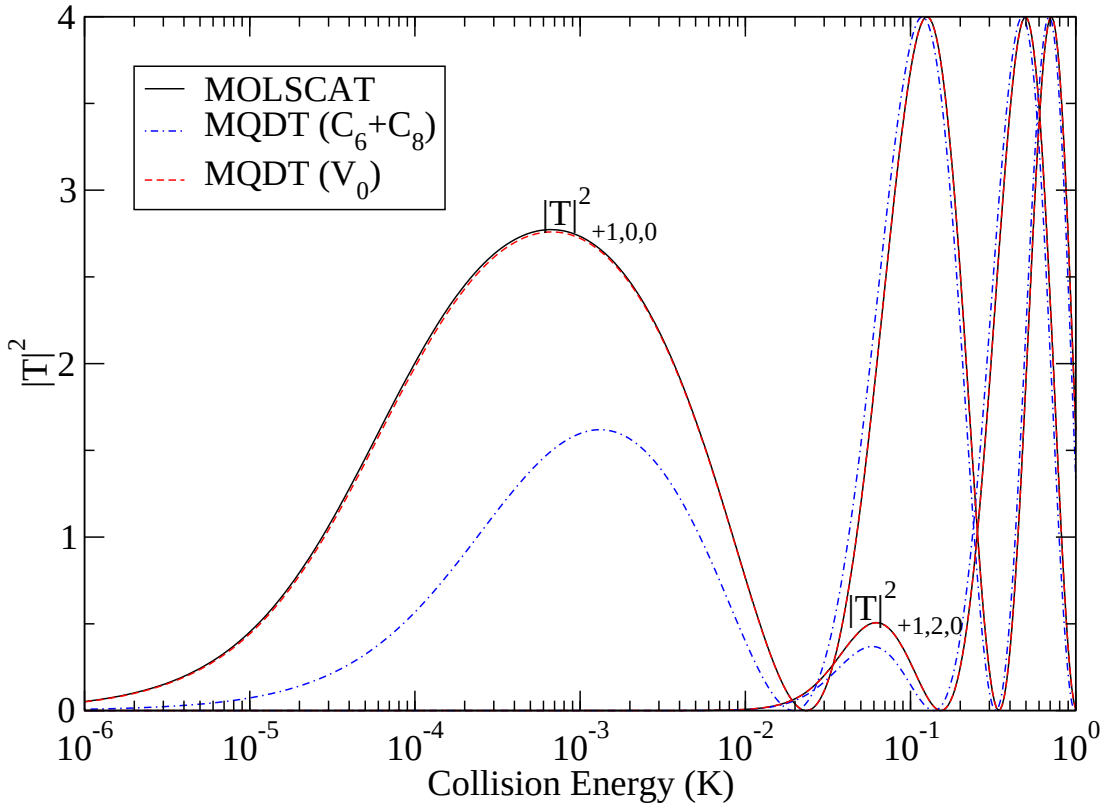

Figure 5.6: The squares of diagonal T-matrix elements in the incoming channels for $m_j = +1$, $L = 0$ and 2 at $B = 10$ G, obtained from full coupled-channel calculations (solid, black) and MQDT with the $C_6 + C_8$ (dot-dashed, blue) and V_0 (dashed, red) reference potentials and $r_{\mathrm{match}} = 6.8$ Å.

places the zeroes in $|T|^2$ (where the phase shift is an integer multiple of π) at very slightly different collision energies. However, at very low energies (below about 1 mK) the MQDT results underestimate the squared T-matrix elements by up to 3%. This probably arises because the "best" reference potential would be one that takes account of adiabatic shifts due to mixing in excited rotational levels. For the $n = 0$ channels, the shift due to $n = 1$ channels may be estimated from 2nd-order perturbation theory to be about 0.012 cm^{-1} (equivalent to 17 mK) at $r_{\mathrm{match}} = 6.8$ Å. This will cause residual errors in the MQDT C functions that are responsible for the small errors visible in Figure 5.7.

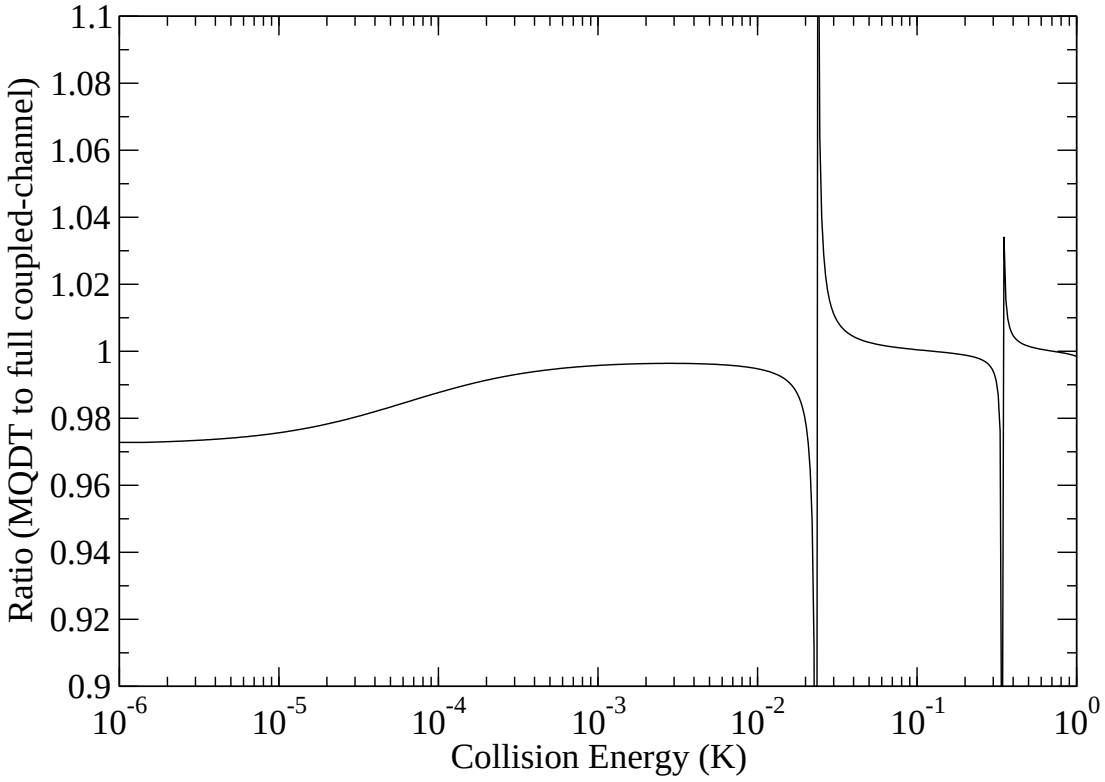

Figure 5.7: Ratio of the square of the diagonal $\boldsymbol{T}$ matrix element for $m_j = +1$, $L = 0$ at $B = 10$ G for MQDT, with the V_0 reference potential and $r_{\mathrm{match}} = 6.8$ Å, to that from full coupled-channel calculations.

Figure 5.8 shows representative matrix elements of $\boldsymbol{Y}$ obtained at $r_{\mathrm{match}} = 6.8$ Å, with the V_0 reference potential, as a function of energy. It may be seen that they are nearly linear in energy. The other matrix elements of $\boldsymbol{Y}$ show similar behavior. While the actual values of matrix elements vary substantially, they are all nearly linear in energy for $r_{\mathrm{match}} = 6.8$ Å.

It should be noted that when the reference functions are obtained numerically, as in the present work, there is no significant difference in computer time for different choices of reference potential. Using the full V_0 reference potential is just as inexpensive as using a simpler one.

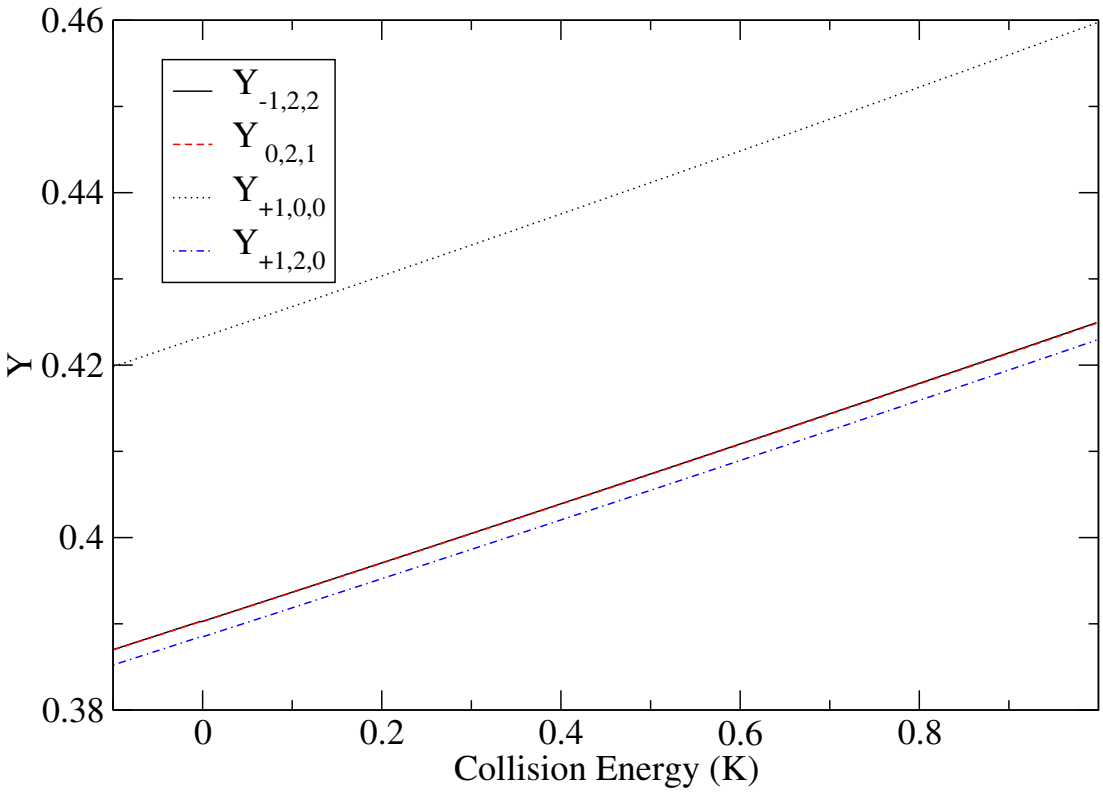

Figure 5.8: Diagonal $\boldsymbol{Y}$ matrix elements as a function of energy at $B = 10$ G, for the V_0 reference potential with $r_{\text{match}} = 6.8$ Å.

5.2.2 Feshbach resonances

Magnetic fields have important effects on cold molecular collisions, and in particular magnetically tunable low-energy Feshbach resonances provide mechanisms by which the collisions may be *controlled*. It is therefore important to establish whether the $\boldsymbol{Y}$ matrices obtained from MQDT are smooth functions of magnetic field as well as energy and can be used to characterize Feshbach resonances. If they are, it will offer substantial computational efficiencies.

Figure 5.9 shows how the diagonal $\boldsymbol{Y}$ matrix elements vary as a function of magnetic field for Mg+NH collisions over the range from 0 to 2500 G for a collision energy of 400 mK. It may be seen that the matrix elements are indeed

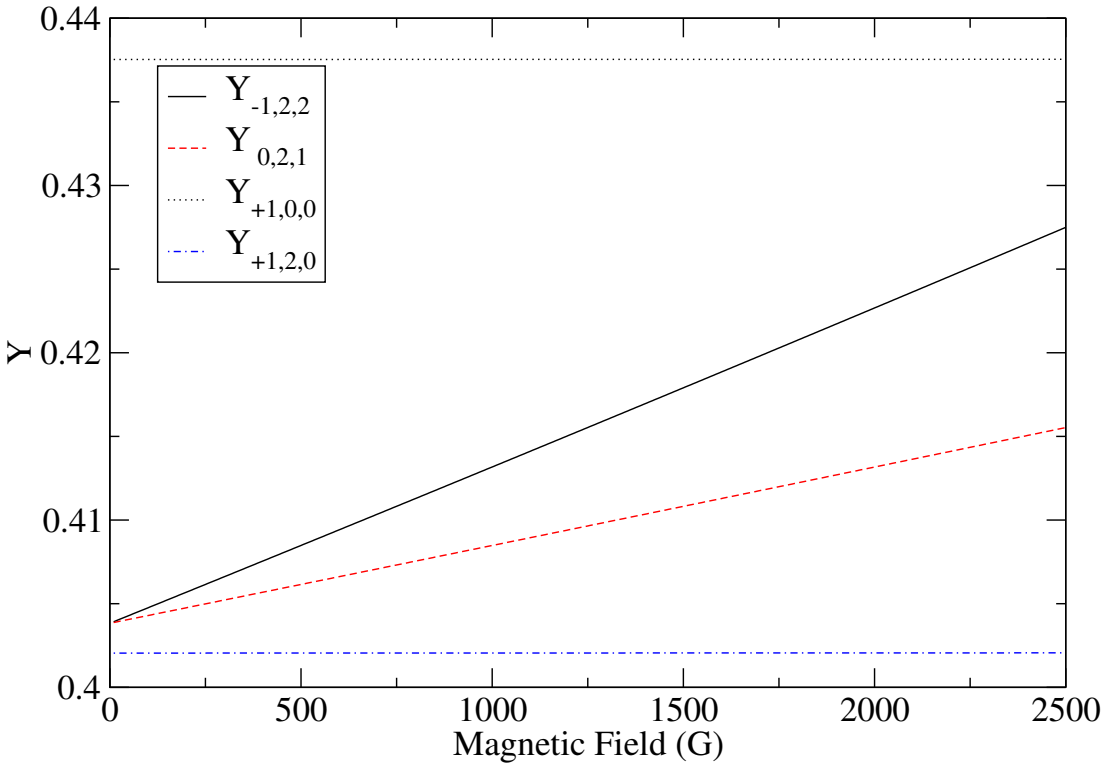

Figure 5.9: Diagonal $\boldsymbol{Y}$ matrix elements as a function of magnetic field at $E/k_{\mathrm{B}} = 400$ mK, for the V_0 reference potential with $r_{\mathrm{match}} = 6.8$ Å.

very nearly linear, as required for efficient interpolation.

In Mg+NH, there is a Feshbach resonance due to the $n = 1$, $j = 0$, $m_j = 0$, $L = 3$ state shown in Figure 5.4 that tunes down towards the $n = 0$, $m_j = +1$ threshold with increasing field. Figure 5.10 shows the comparison between MQDT and full coupled-channel calculations for a selection of diagonal and off-diagonal $\boldsymbol{T}$ matrix elements as the magnetic field is tuned across this resonance at energies of 400 mK and 1 mK. At each energy, MQDT results were obtained both by recalculating the $\boldsymbol{Y}$ matrix at every field and by linear interpolation between two points separated by 100 G. In both cases, the interpolated MQDT results are indistinguishable from the full MQDT results even for this long interpolation.

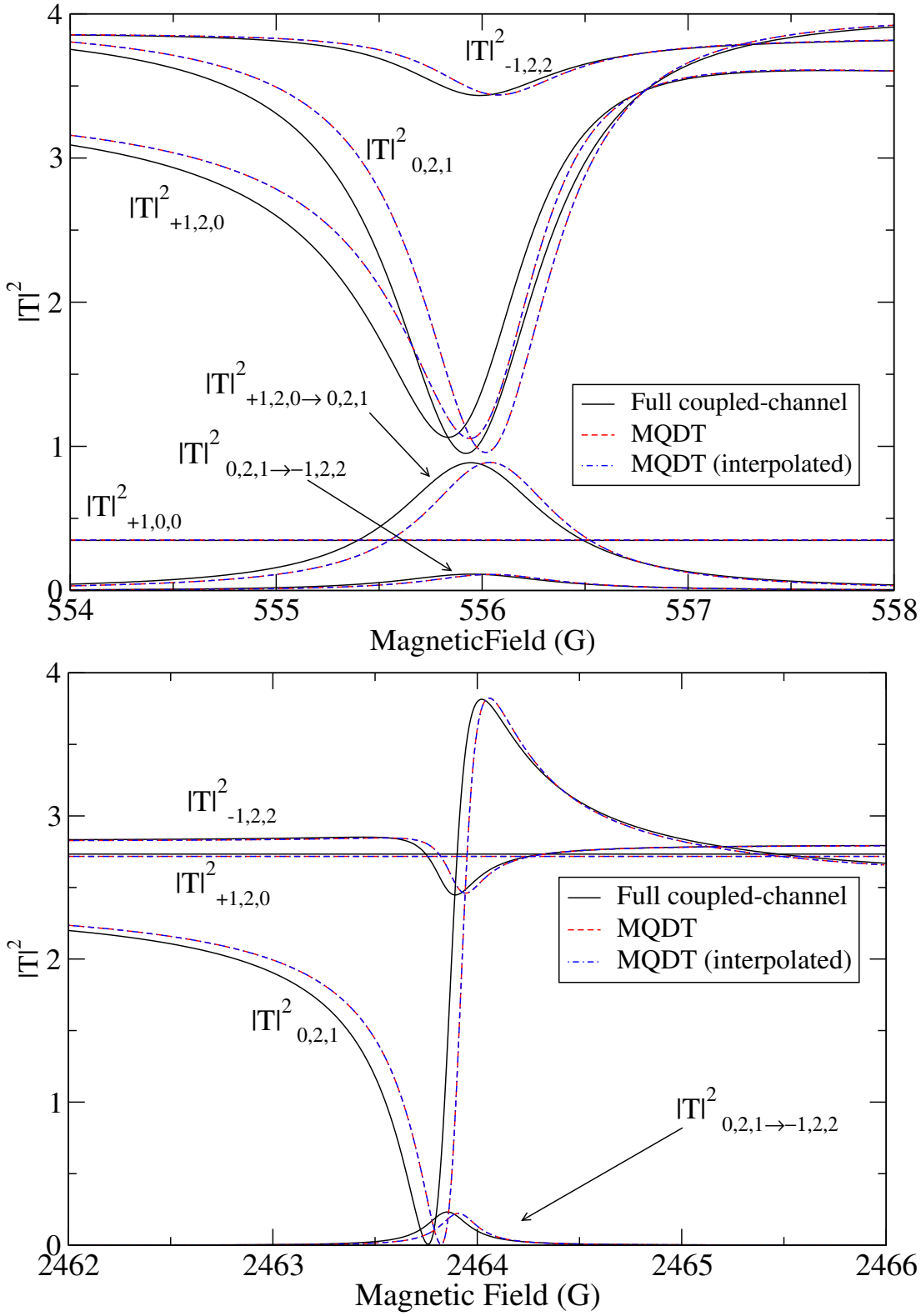

Figure 5.10: Squares of diagonal and off-diagonal T-matrix elements as the field is tuned across a Feshbach resonance at $E/k_{\mathrm{B}} = 400$ mK (upper panel) and 1 mK (lower panel). The MQDT results are obtained with the V_0 reference potential at $r_{\mathrm{match}} = 6.8$ Å.

However, there is also a residual error of of 0.1 to 0.2 G in the resonance position even for the full MQDT results, which is not very different at the two collision energies considered. This is again likely to be due to the effect as described in Section 5.2.1: the V_0 reference potential neglects couplings between channels outside r_{match}, and for the small value of r_{match} used here these couplings are sufficient to shift the resonance positions slightly. Apart from these small shifts, however, both the elastic and the inelastic scattering around the resonances are very well described at both energies.

The linearity of the $\boldsymbol{Y}$ matrix with both energy and applied magnetic field is an extremely promising result, and suggests that MQDT will provide very efficient ways of performing cold collision calculations as a function of energy and magnetic field, without needing to repeat the expensive coupled-channel part of the calculation on a fine grid.

5.3 Conclusions

It has been shown that Multichannel Quantum Defect Theory (MQDT) can be applied to low-energy molecular collisions in applied magnetic fields. MQDT provides a matrix $\boldsymbol{Y}$, defined at a distance r_{match} at relatively short range, which encapsulates all the short-range dynamics of the system. For the prototype Mg+NH system, we have shown that MQDT can provide numerical results that are in quantitative agreement with full coupled-channel calculations if the MQDT reference functions are defined appropriately.

The effect of different choices of reference potential and values of r_{match} has been investigated. For cold atom-molecule collisions, unlike cold atom-atom col-

lisions, calculations are likely to be needed over a significant range of collision energy, perhaps 1 K or so. If r_{match} is placed at too long a range, there is a significant likelihood of resonant features within the energy range that prevent simple interpolation of $\boldsymbol{Y}$. This may be circumvented by carrying out the matching at a smaller distance r_{match}. However, when this is done, a pure C_6 reference potential may not be sufficient. For Mg+NH, the most satisfactory procedure is to perform matching at fairly short range (inside 7 Å) and use a reference potential that is defined to be the same as the true diagonal potential in the incoming channel.

The major strength of MQDT for molecular applications is that, if the the matching to obtain $\boldsymbol{Y}$ is carried out at relatively short range, the matrix is only weakly dependent on collision energy and magnetic field. This allows very considerable computational efficiencies, because the expensive calculation to obtain $\boldsymbol{Y}$ needs to be carried out at only one or a few combinations of collision energy and field. The remaining calculations to obtain scattering properties on a fine grid of energies and fields are then computationally inexpensive, varying only linearly with the number of channels N. Full coupled-channel calculations, by contrast, scale as N^3.

MQDT is a promising alternative to full coupled-channel calculations for cold atom-molecule collisions, particularly when fine scans over collision energy and magnetic field are required. In future work, we will investigate further the choice of reference functions to optimize the accuracy and to minimize the dependence of $\boldsymbol{Y}$ on collision energy and field. We will also investigate how the results for Mg+NH transfer to more strongly anisotropic systems, with stronger long-range anisotropy and more closed channels that are capable of producing scattering resonances.

Chapter 6

Optimized multichannel quantum defect theory for cold molecular collisions

As shown in the previous chapter and (104) Multichannel Quantum Defect Theory (MQDT) (68, 70, 75, 80, 81, 105) provides an attractive alternative to full coupled-channel calculations. MQDT attempts to represent the scattering properties in terms of a matrix $\boldsymbol{Y}(E, B)$ (70, 75, 80, 81) that is a smooth function of E and B. If this can be achieved, the matrix can be obtained once and then used for calculations over a wide range of energies and fields, or obtained by interpolation from a few points. Once the matrix $\boldsymbol{Y}(E, B)$ has been obtained, the time required for calculations at additional energies and fields is only proportional to N, not N^3.

One problem with MQDT is that the $\boldsymbol{Y}$ matrix may have poles as a function of E and B, and these limit the range over which it can be interpolated. In

cold molecular collision studies, calculations are typically needed over an energy range of order 1 K above threshold, and for magnetic fields up to a few thousand gauss. This contrasts with the situation for collisions of ultracold atoms, where the energy range of interest is commonly a few μK and the fields are typically a few hundred gauss.

In this chapter, we show how MQDT $\boldsymbol{Y}$ matrices can be defined to allow smooth interpolation over substantial ranges of collision energy and applied field. This will allow the use of MQDT to provide substantial savings in computer time (106).

The coupled-channel calculations required for both MQDT and the full coupled-channel approach were carried out using the MOLSCAT package (107), as described in chapter 5 section 5.1 using exactly the same input parameters.

The MQDT reference functions and quantum defect parameters were obtained as described in section 3.1, using the renormalized Numerov method (63) to solve the 1-dimensional Schrödinger equations for the reference potentials. The MQDT $\boldsymbol{Y}$ matrix was then obtained by matching to the log-derivative matrix extracted from the coupled-channel propagation at a distance r_{match}. In this chapter all MQDT calculations use the reference potential

$$U_i^{\mathrm{ref}}(r) = V_0(r) + \frac{\hbar^2 L_i(L_i+1)}{2\mu r^2} + E_i^{\infty}, \tag{6.1}$$

where $V_0(r)$ is the isotropic part of the interaction potential. This reference potential was shown, in the previous chapter, to produce quantitatively accurate results when $\boldsymbol{Y}$ is reevaluated at each collision energy and magnetic field. However, such reevaluation relinquishes most of the computational savings that

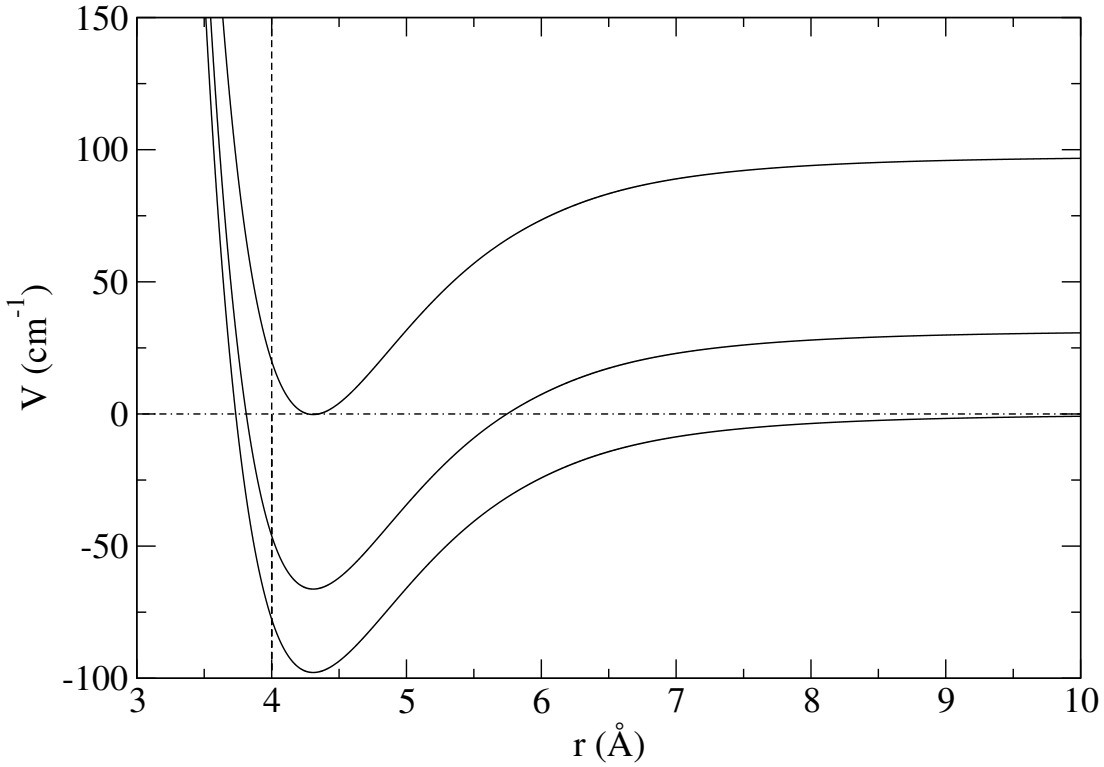

Figure 6.1: The V_0 reference potentials for Mg + NH. The first and second rotational excited state are also shown ($n = 1, 2$). The hard wall at $r = 4.0$ Å is shown as a vertical dashed line. The dot-dashed horizontal line corresponds to zero energy.

MQDT is intended to achieve.

The reference potential contains a hard wall at $r = r_i^{\text{wall}}$, so that $U_i^{\text{ref}}(r) = \infty$ for $r < r_i^{\text{wall}}$. In the present chapter we take $r_i^{\text{wall}} = 4.0$ Å. Figure 6.1 shows the reference potentials for the lowest three rotational states. All channels with $n \geq 2$ were treated as strongly closed and thus not included in the MQDT part of the calculation, but were included in the log-derivative propagation.

6.1 Results and discussion

Figure 6.2 shows a single diagonal element of the $\boldsymbol{Y}$ matrix, $Y_{-1,8+2}$, as a function of the matching distance and energy, obtained with unrotated reference functions. $Y_{-1,8,+2}$ is a representative element of $\boldsymbol{Y}$ with poles at the same locations as the other elements, chosen to give a good visual representation of the pole structure. There are many poles visible, which prevent polynomial interpolation over energies of more that 0.5 K for any value of r_{match} (and much less than this for some choices of r_{match}). The energies of the poles become independent of r_{match} at long range.

The presence of low-energy poles in $\boldsymbol{Y}$ for some values of r_{match} is a serious problem. For MQDT to be efficient, r_{match} must be chosen *without* solving the coupled equations at many different energies. The calculations needed to produce contour plots such as those in Fig. 6.2 are feasible for a test case such as Mg+NH, but would be prohibitively expensive for a very large system.

Figure 6.3 shows the same element of the $\boldsymbol{Y}$ matrix as a function of the matching distance and energy for reference functions rotated by $\theta_i = \pi/2$. The poles are in quite different places, but once again there are many of them. The combination of the top and center panels demonstrates that, for any arbitrary choice of rotation angle, poles will appear in the $\boldsymbol{Y}$ matrix, preventing simple interpolation for most choices of r_{match}. This will be true in any MQDT problem with a large density of resonances. The contour plots do however show that the position of poles is strongly dependent on the rotation angle, even at large values of r_{match}. This suggests that it will be possible to optimize the rotation angle in order to move the poles away from the energy range of interest. It is emphasized

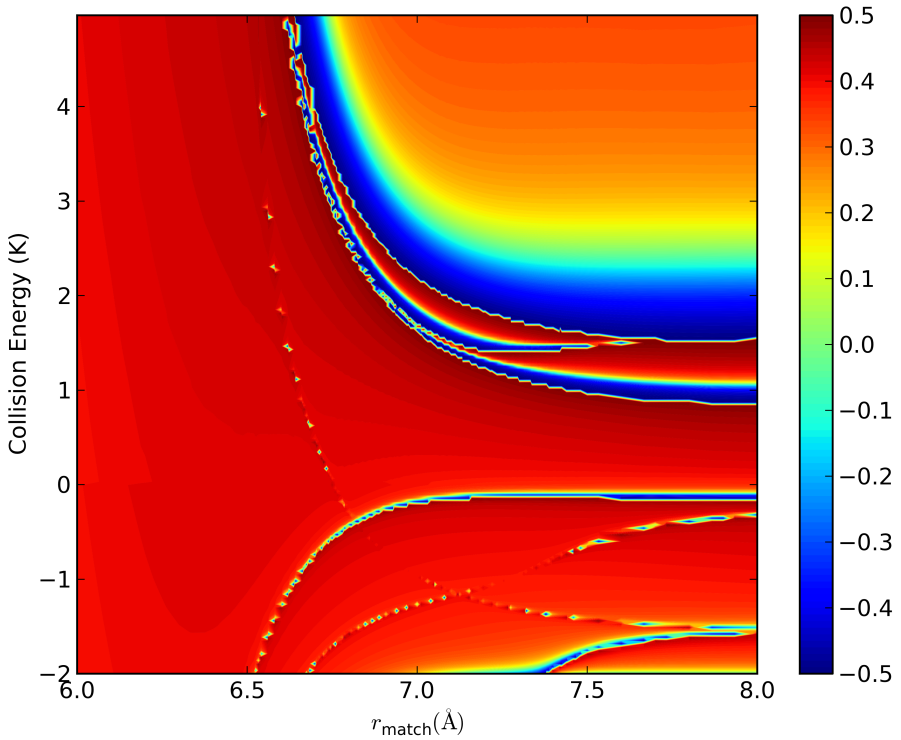

Figure 6.2: Contour plot of $\arctan Y_{ii}/\pi$ for a representative diagonal $\boldsymbol{Y}$ matrix element, $Y_{-1,8,+2}$, as a function of energy and r_{match} at $B = 10$ G. Obtained with unrotated reference functions ($\theta_i = 0$). The arctangent is show for clarity of plotting: it maps the real numbers, $\mathbb{R}$, to the domain $-\pi/2$ to $\pi/2$, thus allowing all magnitudes of $\boldsymbol{Y}$ matrix elements to be seen on a single plot.

that the $\boldsymbol{S}$ matrices obtained from the $\boldsymbol{Y}$ matrices shown in figures 6.2, 6.3 and 6.4 are identical.

We now consider how to rotate the reference functions to maximize the pole-free range over which $\boldsymbol{Y}$ can be interpolated. Y_{ii} as a function of θ_i is given by

$$Y_{ii} = \tan(\theta_i + \delta_i), \tag{6.2}$$

where δ_i is the phase shift between the unrotated reference function f_i and the

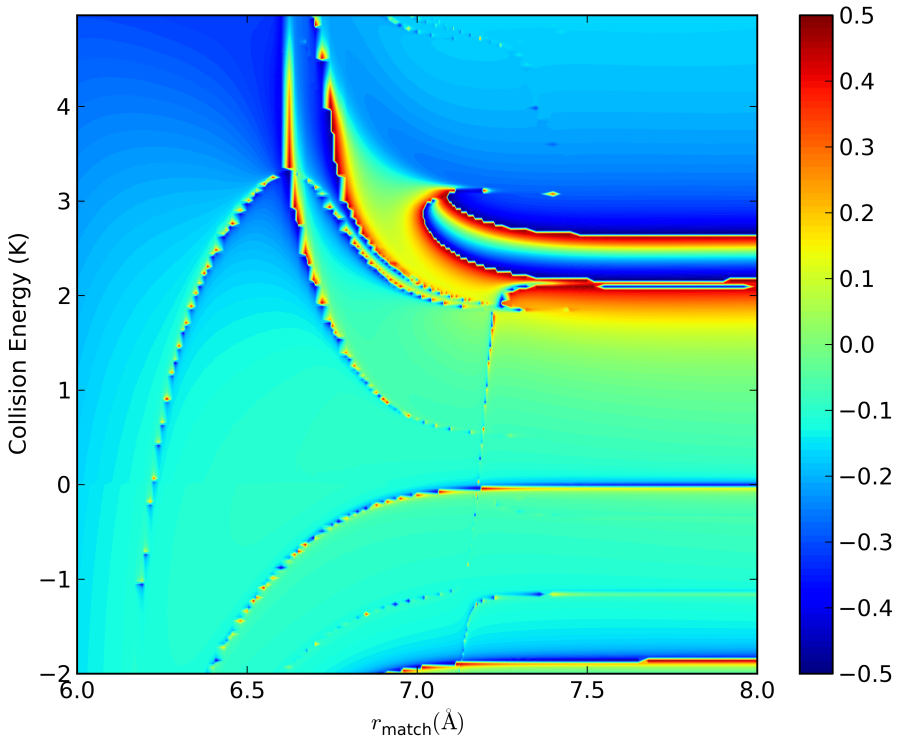

Figure 6.3: Contour plot of $\arctan Y_{ii}/\pi$ for a representative diagonal $\boldsymbol{Y}$ matrix element, $Y_{-1,8,+2}$, as a function of energy and r_{match} at $B = 10$ G. Obtained with reference functions rotated by $\theta_i = \pi/2$. The arctangent is show for clarity of plotting: it maps the real numbers, $\mathbb{R}$, to the domain $-\pi/2$ to $\pi/2$, thus allowing all magnitudes of $\boldsymbol{Y}$ matrix elements to be seen on a single plot.

propagated multichannel wavefunction in channel i. There is a pole in Y_{ii} when $\theta_i + \delta_i = \pi/2$ and a zero when $\theta_i + \delta_i = 0$. We thus set $\theta_i^{\mathrm{opt}} = -\delta_i$ at one choice of r_{match}, E and B, so that the propagated multichannel wavefunction and the reference wavefunctions are almost in phase and the resulting $\boldsymbol{Y}$ matrix in that region is pole-free.

Because the channels are coupled, rotating the reference functions in one channel affects the other elements of the $\boldsymbol{Y}$ matrix. In this work we loop over the channels sequentially, setting each diagonal element to 0 in turn. By repeatedly

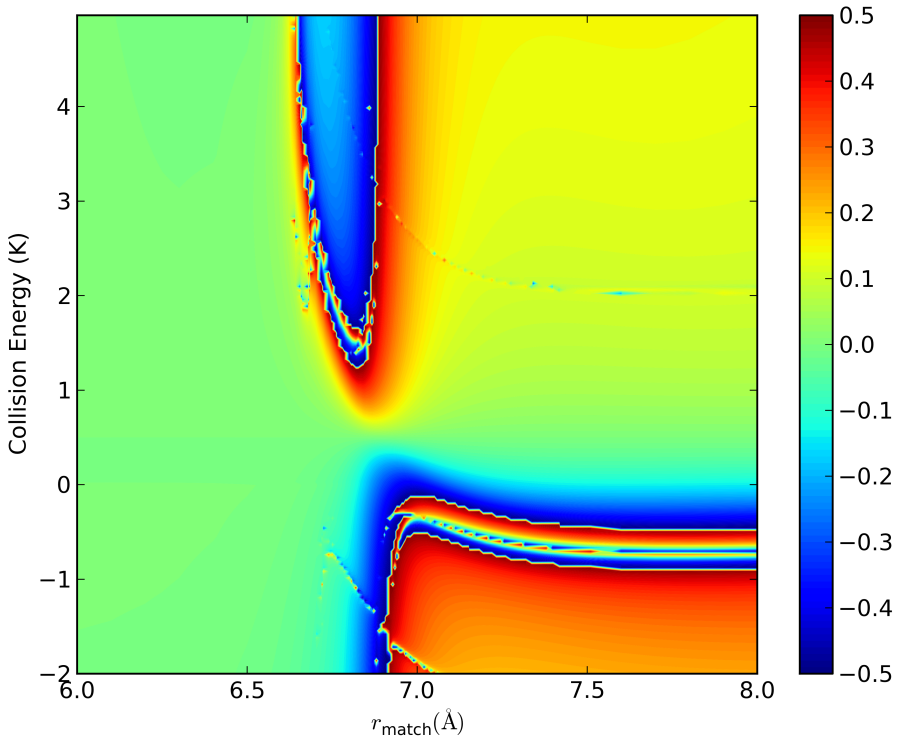

Figure 6.4: Contour plot of $\arctan Y_{ii}/\pi$ for a representative diagonal $\boldsymbol{Y}$ matrix element, $Y_{-1,8,+2}$, as a function of energy and r_{match} at $B = 10$ G. Obtained with optimized reference functions with $\theta_i = \theta_i^{\text{opt}}$ in all channels. The arctangent is show for clarity of plotting: it maps the real numbers, $\mathbb{R}$, to the domain $-\pi/2$ to $\pi/2$, thus allowing all magnitudes of $\boldsymbol{Y}$ matrix elements to be seen on a single plot.

looping over all channels, all the diagonal $\boldsymbol{Y}$ matrix elements are set to 0. For Mg+NH it was sufficient to loop over the channels twice. In a more strongly coupled system it is expected that this would need to be repeated more times. This approach allows a set of optimized θ_i to be obtained from a single multichannel propagation.

Rotated reference functions have previously been used to transform $\boldsymbol{Y}$ matrices in the study of atomic spectra (108, 109, 110, 111, 112) and atomic collisions (113). Adjusting θ_i at each energy such that $Y_{ii} = 0$ was shown to produce

a weak energy dependence of off-diagonal $\boldsymbol{Y}$ matrix elements across thresholds (113). However, this approach required propagating the full multichannel wavefunction many times at different energies, which is precisely what the present work tries to avoid.

Figure 6.4 shows how the representative element $Y^{\mathrm{opt}}_{-1,8,+2}$ varies as a function of the matching distance and energy. All the θ_i values are optimized as described above at $E = 0.5$ K and $B = 10$ G for each value of r_{match}, but are *not* reoptimised at each energy. Comparison of this with the figures 6.2 and 6.3 shows the effectiveness of optimizing the reference functions. Without optimization, there were no choices of r_{match} for which $\boldsymbol{Y}$ was pole-free and thus suitable for interpolation over the energy range of interest. After optimization, $\boldsymbol{Y}^{\mathrm{opt}}$ is pole-free over a substantial range, of about 1 K, for any choice of $r_{\mathrm{match}} < 8$ Å. For values of $r_{\mathrm{match}} < 6.5$ Å, $\boldsymbol{Y}^{\mathrm{opt}}$ is pole-free over many Kelvin. Beyond 6.5 Å, poles start to enter $\boldsymbol{Y}^{\mathrm{opt}}$ in the energy range of interest. Once the poles have settled at their asymptotic values at $r_{\mathrm{match}} > 7.5$ Å, we find that positive energies up to about 2 K are pole-free. However, at larger values of r_{match} the linearity of $\boldsymbol{Y}^{\mathrm{opt}}$ over the pole-free region decreases. This is due to negative energy poles in the $\boldsymbol{Y}$ matrix which our procedure cannot move significantly. There is one particularly bad choice of r_{match} at ≈ 6.8 Å, but provided this unlucky choice of r_{match} is avoided, $\boldsymbol{Y}^{\mathrm{opt}}$ can be interpolated smoothly over the positive energy range from 0 to > 2 K for any choice of r_{match}.

Figure 6.5 compares diagonal T-matrix elements $|T_{ii}|^2$ (where $T_{ij} = \delta_{ij} - S_{ij}$) obtained from full coupled-channel calculations with those from the MQDT method, with a matching distance of $r_{\mathrm{match}} = 6.5$ Å, using reference functions optimized at 0.5 K. MQDT results were obtained both by recalculating the $\boldsymbol{Y}$

matrix at every energy and by interpolating $\boldsymbol{Y}^{\mathrm{opt}}$ linearly between two points separated by 1 K. The MQDT results with $\boldsymbol{Y}$ recalculated at each energy can scarcely be distinguished from the full coupled-channel results. The MQDT results obtained by interpolation are also very similar to the full coupled-channel results except around the resonance feature at $E \approx 0.1$ K. The interpolated result could of course be improved simply by performing coupled-channel calculations to obtain $\boldsymbol{Y}^{\mathrm{opt}}$ at one or two extra energies across the range, to allow for a higher-order interpolation, or by using a linear interpolation over a smaller energy range.

In this work we use θ_i to rotate our short-range reference functions f_i and g_i. In principle, we could rotate the reference functions by varying the asymptotic phase shifts ξ_i instead of the short-range phases θ_i. However Figure 6.6 shows why this is not desirable. Due to the highly nonlinear relationship between ξ_i and θ_i, obtaining the optimum rotation angle of the short-range reference functions f_i and g_i by varying the angle ξ_i would be laborious at very low collision energies.

6.1.1 Magnetically tunable Feshbach resonances

The effects of magnetic fields on cold molecular collisions are very important, since collisions can be controlled by taking advantage of magnetically tunable low-energy Feshbach resonances. We are therefore interested in how $\boldsymbol{S}$ matrix elements behave as a function of magnetic field across Feshbach resonances. It is thus important that the $\boldsymbol{Y}$ matrix is weakly dependent on magnetic field in such regions.

Figure 6.7 shows the diagonal elements of the optimized $\boldsymbol{Y}$ matrix as a func-

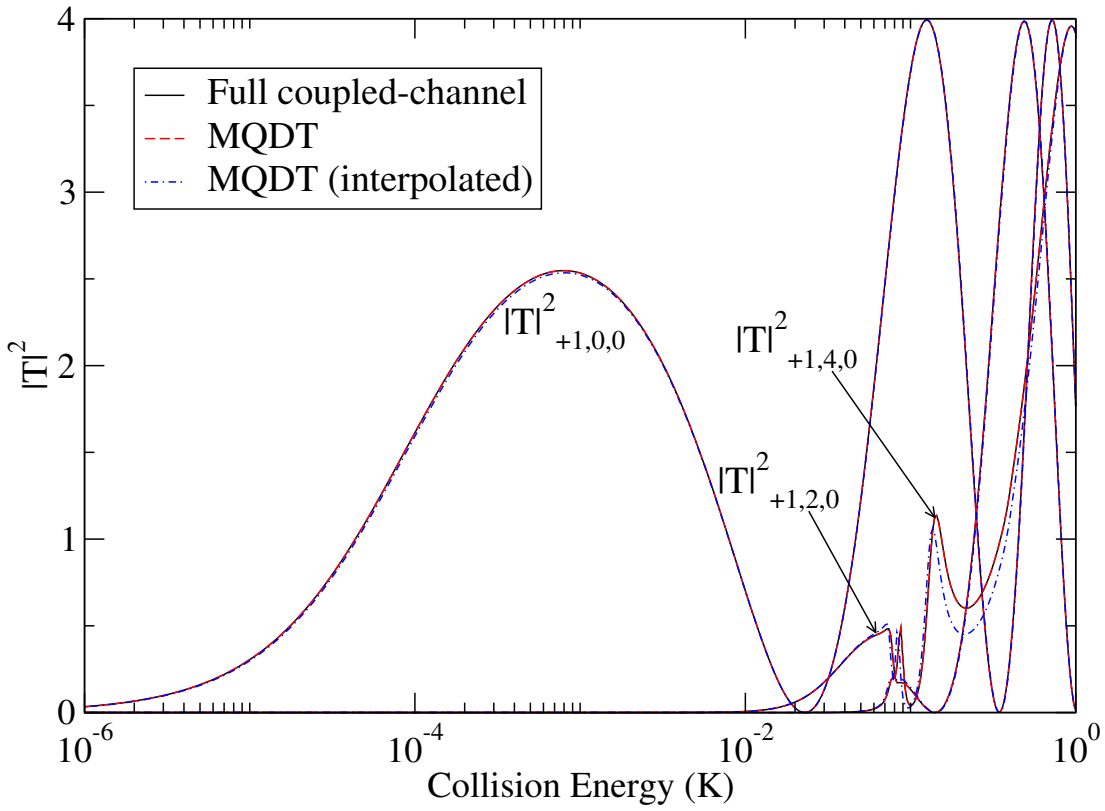

Figure 6.5: The squares of diagonal T-matrix elements T_{m_j,L,M_L} in the incoming channels for $m_j = +1$ and $L = 0$, 2 and 4 at $B = 10$ G, obtained from full coupled-channel calculations (solid, black) and MQDT with optimized reference functions for $r_{\mathrm{match}} = 6.5$ Å, both with (dot-dash, blue) and without (dashed, red) interpolation.

tion of magnetic field for Mg + NH collisions over the range from 10 G to 5000 G for a collision energy of 1 mK. This range of fields tunes across 6 Feshbach resonances. The reference functions were optimized at 10 G and 1 mK. The elements of $\boldsymbol{Y}^{\mathrm{opt}}$ are smoothly curved over the entire 5000 G range and could be well represented by a low-order polynomial.

Figure 6.8 shows the comparison between optimized MQDT and full coupled-channel calculations for a selection of diagonal and off-diagonal T-matrix elements as the magnetic field is tuned at 1 mK. The reference functions were optimized at

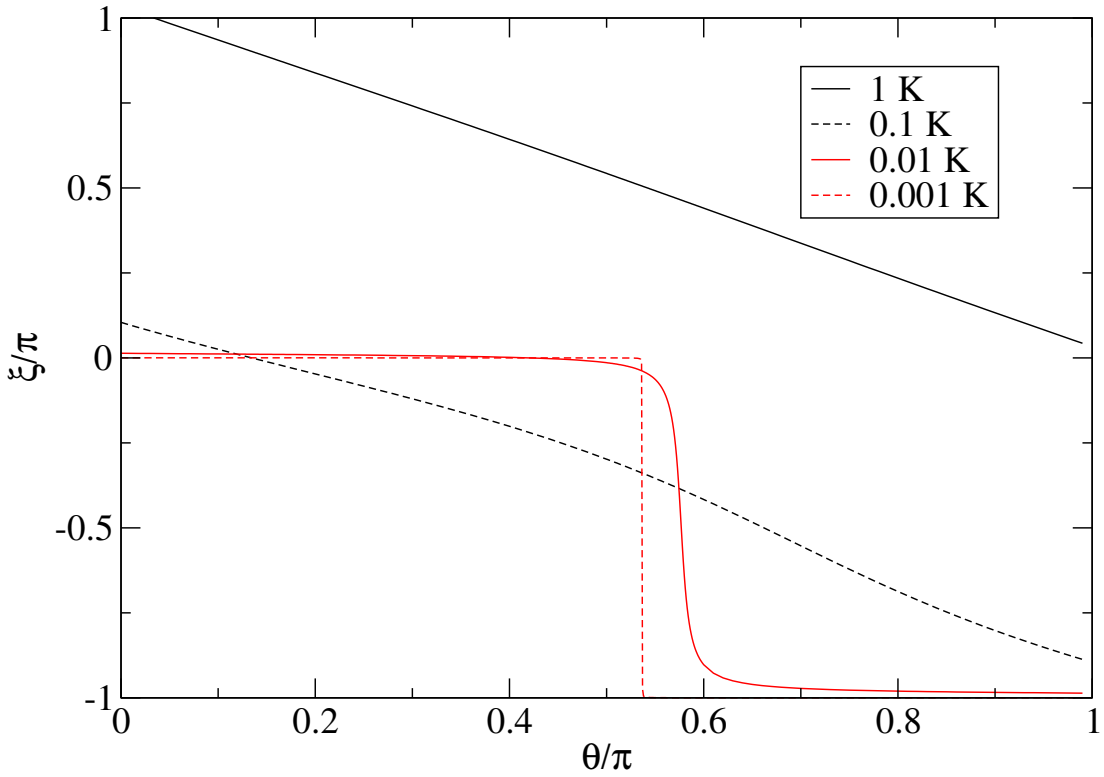

Figure 6.6: The asymptotic phase shift $\bar{\xi}_i$ as a function of the rotation angle θ for the incoming d-wave channel $(+1, 2, 0)$.

10 G and 1 mK and MQDT results were obtained by linear interpolation of $\boldsymbol{Y}^{\mathrm{opt}}$ between two points separated by 1000 G and by 5000 G. Interpolation over 1000 G gives resonance features that are in very good agreement with the full coupled-channel calculation to better than 1 G. Interpolation over 5000 G gives resonance features of the correct shape, with positions that are still within about 10 G of the full coupled-channel results. The difference between the interpolated result and the full coupled-channel calculation is a result of both the choice of r_{match} and the interpolation. The quality of the interpolation could be improved by considering a few more fields across the range to allow for higher-order polynomial interpolation or by using linear interpolation over a smaller field range.

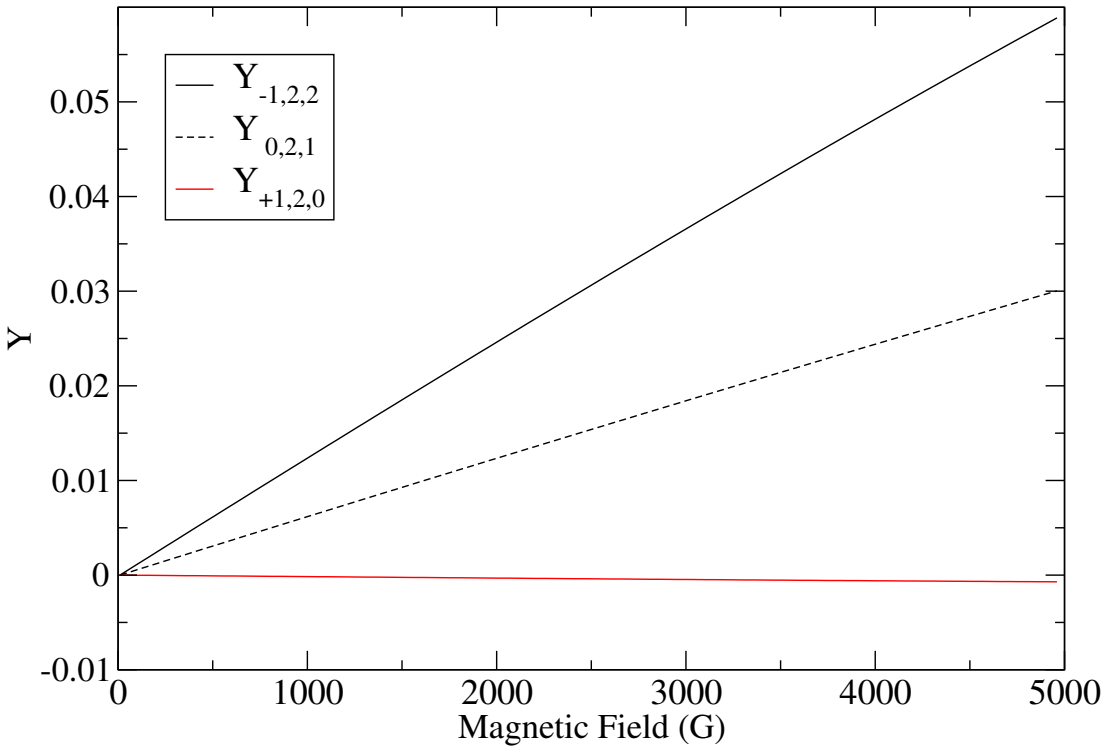

Figure 6.7: Representative $\boldsymbol{Y}^{\mathrm{opt}}$ matrix elements as a function of field at $E = 1$ mK.

Full MQDT calculations recalculating the $\boldsymbol{Y}$ matrix at every magnetic field give resonance positions accurate to 0.01 G. The remaining errors between the full coupled-channel calculations and the MQDT results will reduce with a larger choice of r_{match}. As seen in figure 6.4 the optimized $\boldsymbol{Y}$ matrices obtained at larger values of r_{match} are still amenable to interpolation, though over a more restricted energy range.

6.2 Conclusions

It has been shown that Multichannel Quantum Defect Theory can provide an efficient computational method for low-energy molecular collisions as a function

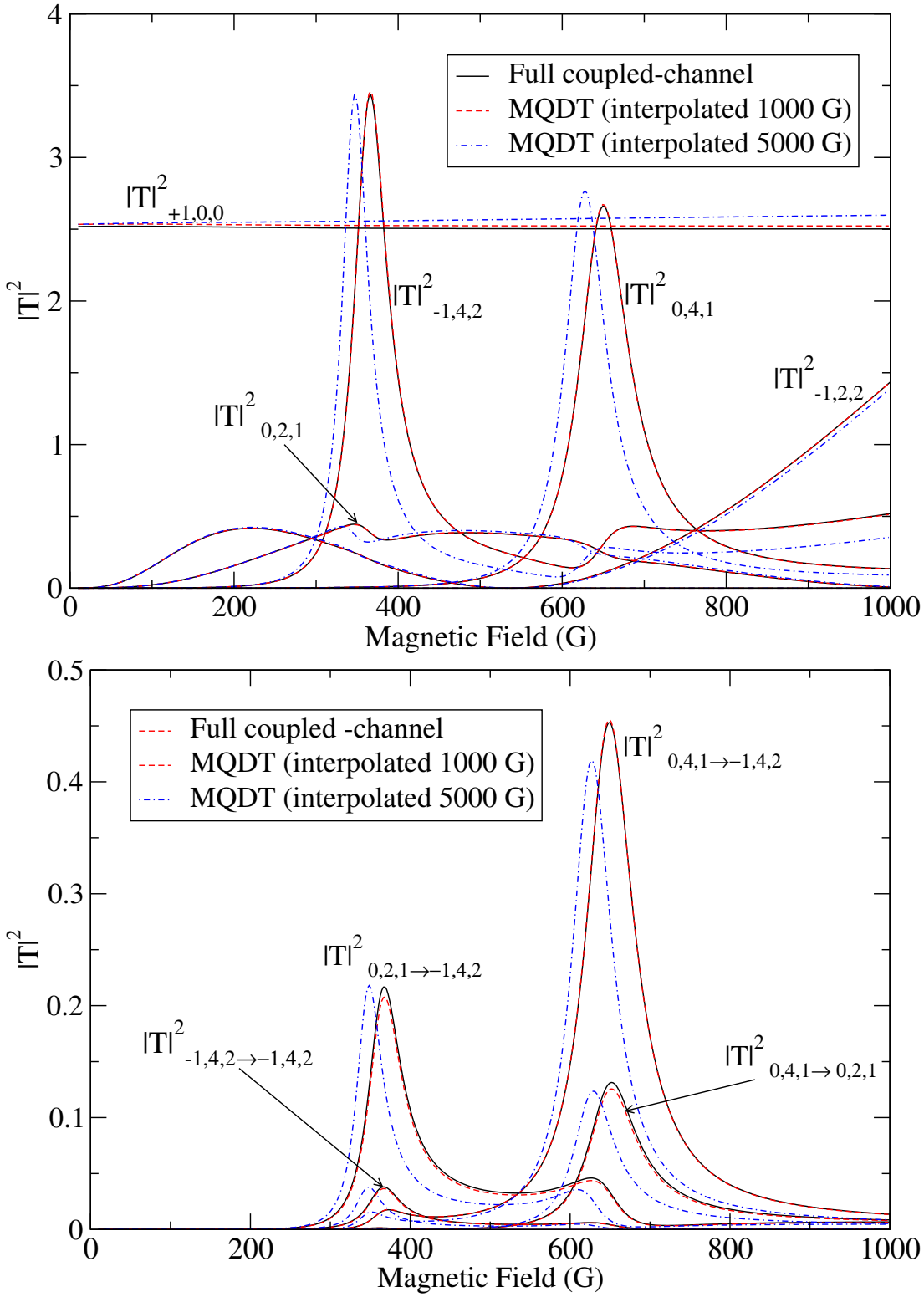

Figure 6.8: Squares of T-matrix elements at 1 mK as a function of field in the vicinity of a Feshbach resonance. Upper panel: diagonal elements; lower panel: off-diagonal elements.

of both energy and magnetic field. In particular, we have shown how a disposable parameter of MQDT, the phase of the short-range reference functions, may be chosen to make the MQDT $\boldsymbol{Y}$ matrix smooth and pole-free over a wide range of energy and field. This smooth variation allows the $\boldsymbol{Y}$ matrix to be evaluated from coupled-channel calculations at a few values of the energy and field and then to be obtained by interpolation at intermediate values. It is not necessary to repeat the expensive coupled-channel part of the calculation on a fine grid.

The procedure developed here is to choose the phase of the reference functions in each channel so that the diagonal $\boldsymbol{Y}$ matrix in each channel is zero at a reference energy and field. This ensures that there are no poles in the $\boldsymbol{Y}$ matrix, which would prevent smooth interpolation, close to the reference energy. Optimizing the phase in this way is very inexpensive, and once it is done the cost of calculations at additional energies and fields varies only linearly with the number of channels N, not as N^3 as for full coupled-channel calculations. MQDT with optimized $\boldsymbol{Y}$ matrices is thus a very promising alternative to full coupled-channel calculations for cold molecular collisions, particularly when fine scans over collision energy and magnetic field are required.

The $\boldsymbol{Y}$ matrix is defined to encapsulate all the collision dynamics that occurs inside a matching distance r_{match}, and the choice of this distance is important. There is a trade-off between the accuracy of the method and the size of the pole-free region of the optimized $\boldsymbol{Y}$ matrix. For large values of r_{match}, resonant features may appear in the $\boldsymbol{Y}$ matrix and prevent simple interpolation over large ranges of energy and field. For smaller values of r_{match}, optimizing the reference functions allows interpolation over many Kelvin, but the accuracy of MQDT is reduced because interchannel coupling is neglected outside r_{match}.

For the moderately anisotropic Mg + NH system studied here, optimized MQDT with an interpolated $\boldsymbol{Y}$ matrix can provide numerical results in quantitative agreement with fully converged coupled-channel calculations. In the subsequent chapters, we will investigate the extension of this approach to more strongly coupled systems, with larger anisotropy of the interaction potential and more closed channels that produce scattering resonances.

Chapter 7

Collisions of ^2S Atoms with $^3\Sigma$ Molecules

In order to study a strongly anisotropic system which has many closed channels that produce scattering resonances we choose Li(^2S)+NH($^3\Sigma$). The matrix elements for collisions of ^2S atoms with $^3\Sigma$ molecules shown in this chapter are given in (60, 114). The Hamiltonian for a ^{2}S atom colliding with a rigid-rotor $^3\Sigma$ diatomic molecule is given by

$$\hat{H} = -\frac{\hbar^2}{2\mu} r^{-1} \frac{d^2}{dr^2} r + \frac{\hat{L}^2}{2\mu r^2} + \hat{H}_{\rm mon} + \hat{H}_{\rm Z} + V_{\rm ss}(r) + V(r,\theta), \qquad (7.1)$$

which is exactly the same as equation 4.1, for the interaction of a ^1S atom with a $^3\Sigma$ molecule, with the addition of the anisotropic intermolecular spin-spin interaction, $V_{\rm ss}(r)$. The presence of an unpaired spin on the atom changes the Zeeman

operator, which is now given by

$$\hat{H}_{\mathrm{Z}} = g_e \mu_{\mathrm{B}} \hat{B} \cdot (\hat{s}_{\mathrm{NH}} + \hat{s}_{\mathrm{Li}}), \tag{7.2}$$

where $\hat{s}_{\mathrm{Li}}$ and $\hat{s}_{\mathrm{NH}}$ are the spin angular momentum operators for the Li atom and the NH molecule respectively. As in equation 4.9 g_{e} is the g-factor for the electron, μ_{B} the Bohr magneton and $\hat{B}$ is the magnetic field vector. The anisotropic intermolecular spin-spin interaction is given by

$$V_{\mathrm{ss}}(r) = \lambda(r) \left[\hat{s}_{\mathrm{Li}} \cdot \hat{s}_{\mathrm{NH}} - 3(\hat{s}_{\mathrm{Li}} \cdot \hat{e}_{\mathrm{r}})(\hat{s}_{\mathrm{NH}} \cdot \hat{e}_{\mathrm{r}}) \right], \tag{7.3}$$

where $\hat{e}_{\mathrm{r}}$ is a unit vector along r, $\lambda(r) = -E_{\mathrm{h}}\alpha^2/(r/a_0)^3$ and $\alpha \approx 1/137$ is the fine structure constant.

7.1 Matrix elements of the Hamiltonian

We construct the collision Hamiltonian in the fully uncoupled basis set $|nm_n\rangle|s_{\mathrm{NH}}m_{s_{\mathrm{NH}}}\rangle|s_{\mathrm{Li}}m_{s_{\mathrm{Li}}}\rangle|LM_L\rangle$, where the quantum numbers n and s_{NH} describe the rotation and electron spin of the NH molecule and s_{Li} describes the electron spin of the Li atom. The corresponding m quantum numbers are the projections onto the space-fixed magnetic field axis. The matrix elements for the NH monomer are the same as for scattering of NH from a closed-shell atom given in chapter 4, with the addition of factors $\delta_{m_{s\mathrm{A}}m'_{s\mathrm{A}}}$ given here.

7.1.1 Spin-spin interaction

The matrix elements for the intermolecular spin-spin interaction are given by

$$\begin{aligned}
\langle s_{\mathrm{A}} m_{s\mathrm{A}} s_{\mathrm{B}} m_{s\mathrm{B}} n_{\mathrm{B}} m_{n\mathrm{B}} L M_L | \quad & V_{\mathrm{ss}} \quad |s_{\mathrm{A}} m'_{s\mathrm{A}} s_{\mathrm{B}} m'_{s\mathrm{B}} n'_{\mathrm{B}} m'_{n\mathrm{B}} L' M'_L\rangle \\
&= \sqrt{30}\lambda(r)\delta_{n_{\mathrm{B}} n'_{\mathrm{B}}}\delta_{m_{n\mathrm{B}} m'_{n\mathrm{B}}}(-1)^{s_{\mathrm{A}}+s_{\mathrm{B}}-m_{s\mathrm{A}}-m_{s\mathrm{B}}-M_L} \\
&\times \left[s_{\mathrm{A}}(s_{\mathrm{A}}+1)(2s_{\mathrm{A}}+1)s_{\mathrm{B}}(s_{\mathrm{B}}+1)(2s_{\mathrm{B}}+1)(2L+1)(2L'+1)\right]^{\frac{1}{2}} \\
&\times \begin{pmatrix} L & 2 & L' \\ 0 & 0 & 0 \end{pmatrix} \sum_{q_1 q_2} \begin{pmatrix} L & 2 & L' \\ -M_L & -q_1-q_2 & M'_L \end{pmatrix} \\
&\times \begin{pmatrix} 1 & 1 & 2 \\ q_1 & q_2 & -q_1-q_2 \end{pmatrix} \begin{pmatrix} s_{\mathrm{A}} & 1 & s_{\mathrm{A}} \\ -m_{s\mathrm{A}} & q_1 & m'_{s\mathrm{A}} \end{pmatrix} \begin{pmatrix} s_{\mathrm{B}} & 1 & s_{\mathrm{B}} \\ -m_{s\mathrm{B}} & q_2 & m'_{s\mathrm{B}} \end{pmatrix}.
\end{aligned} \tag{7.4}$$

7.1.2 Expansion of the Potential

Spin changing collisions of Li with NH involve both the doublet ($S = \frac{1}{2}$) and quartet ($S = \frac{3}{2}$) potential energy surfaces, where S is the total spin of the system. The interaction potential $V_{\mathrm{int}}(r,\theta)$ written in terms of projection operators is given by,

$$V_{\mathrm{int}}(r,\theta) = \sum_{S=-|s_{\mathrm{A}}+s_{\mathrm{B}}|}^{s_{\mathrm{A}}+s_{\mathrm{B}}} |S\rangle V_S(r,\theta)\langle S|. \tag{7.5}$$

The matrix elements of $V_{\rm int}(r,\theta)$ are then

$$\begin{aligned}\langle s_{\rm A} m_{s{\rm A}} s_{\rm B} m_{s{\rm B}} n_{\rm B} m_{n{\rm B}} L M_L| \quad V_{\rm int}(r,\theta) \quad & |s_{\rm A} m'_{s_{\rm A}} s_{\rm B} m'_{s{\rm B}} n'_{\rm B} m'_{n{\rm B}} L' M'_L\rangle \\ = \quad & \sum_S (-1)^{2s_{\rm A}+2s_{\rm B}-m_{s{\rm A}}-m_{s{\rm B}}-M_L}(2S+1) \\ \times \quad & \langle n_{\rm B} m_{n{\rm B}} L M_L|V_S(r,\theta)|n'_{\rm B} m'_{n{\rm B}} L' M'_L\rangle \\ \times \quad & \begin{pmatrix} s_{\rm A} & s_{\rm B} & S \\ m_{s{\rm A}} & m_{s{\rm B}} & -m_{s{\rm A}}-m_{s{\rm B}} \end{pmatrix} \begin{pmatrix} s_{\rm A} & s_{\rm B} & S \\ m'_{s{\rm A}} & m'_{s{\rm B}} & -m'_{s{\rm A}}-m'_{s{\rm B}} \end{pmatrix}.\end{aligned} \tag{7.6}$$

In this work we are interested in collisions between atoms and molecules in spin-stretched states, of interest for sympathetic cooling. These states have no matrix elements, either diagonal or off-diagonal, which involve the doublet potential energy surface. In addition both the doublet and quartet interaction potentials become degenerate at long range when there is no overlap between the valence shells of the Li and NH. We thus approximate the operator $V_{\rm int}(r,\theta)$ by taking $V_S = V_{3/2}$ for both spin states, as in the work by Wallis *et al* on collisions of Li and NH (114). This approximation reduces equation 7.6 to a form diagonal both in $m_{s{\rm A}}$ and $m_{s{\rm B}}$.

Chapter 8

Multichannel Quantum Defect Theory for cold molecular collisions with a strongly anisotropic potential energy surface

8.1 Introduction

The application of MQDT to cold molecular collisions for the moderately anisotropic system Mg+NH($^3\Sigma^-$) has been demonstrated in the preceding chapters and also in (104, 106) . In order to study a more strongly anisotropic system with many more closed channels we choose Li+NH, which has been studied previously using full coupled-channels calculations by Wallis *et al.* (114). The potential energy

surface for this system is deep and highly anisotropic, with a well depth about 1800 cm^{-1} at the Li-NH geometry but only 113 cm^{-1} at the NH-Li geometry.

8.2 Theory

The phase of the short-range reference functions f_i and g_i is a disposable parameter of MQDT and may be chosen to generate a $\boldsymbol{Y}$ matrix smooth and pole-free over a wide range of energy and field. Equation 3.3 shows that the $\boldsymbol{Y}$ matrix has a pole whenever the component of the propagated multichannel wavefunction ψ_i in any channel i is proportional to the reference function g_i and has no contribution from f_i, i.e. when g_i and the full coupled-channels solution have the same phase at r_{match}. In ref. (106), we proposed rotating the reference functions f_i and g_i in channel i by an angle θ_i, chosen so that the diagonal matrix elements Y_{ii} are 0. This ensures that the reference function g_i and the full coupled-channels solution in channel i are perfectly out of phase at the chosen r_{match} for a particular E and B. The resulting $\boldsymbol{Y}$ matrix in that region is therefore pole-free (106).

The range of the pole-free region is dependent on where the matching occurs. When matching is in the classically allowed region, the phases of both the reference functions and the propagated coupled-channels solutions vary approximately linearly with energy and setting the diagonal $\boldsymbol{Y}$ matrix elements to zero is effective: the *relative* phase of the reference potentials and the coupled-channels solution is a slow function of energy. For a closed channel where matching is carried out in the classically forbidden region, however, there is resonance structure in both the coupled-channels solutions and the reference functions so that the phase of each is a fast (and nonlinear) function of energy. Fortunately, the

energies at which the resonance structure occurs depend on the choice of θ_i. In the present work we show that a more sophisticated choice of θ_i than that of ref. (106) can produce a larger pole-free region, and that this is important when the channels are strongly coupled.

8.2.1 Basis set and quantum numbers

As discussed in chapter 7 we construct the collision Hamiltonian in the fully uncoupled basis set $|nm_n\rangle|s_{\mathrm{NH}}m_{s_{\mathrm{NH}}}\rangle|s_{\mathrm{Li}}m_{s_{\mathrm{Li}}}\rangle|LM_L\rangle$. Hyperfine structure is neglected.

We label elements of $\boldsymbol{Y}$ and $\boldsymbol{S}$ by subscripts $n, m_n, m_{s_{\mathrm{NH}}}, m_{s_{\mathrm{Li}}}, L, M_L \rightarrow n', m'_n, m'_{s_{\mathrm{NH}}}, m'_{s_{\mathrm{Li}}}, L', M'_L$. For diagonal elements we suppress the second set of labels.

8.2.2 Numerical methods

The coupled-channel calculations required for both MQDT and the full coupled-channel approach were carried out using the MOLSCAT package (107), as described in section 5.1. As in the work by Wallis *et al.* (114) the full coupled-channels calculations use $r_{\mathrm{min}} = 1.8$ Å, $r_{\mathrm{mid}} = 12.5$ Å and $r_{\mathrm{max}} = 600$ Å (where 1 Å $= 10^{-10}$ m).

The MQDT reference functions and quantum defect parameters are obtained as described in section 3.1, using the renormalized Numerov method (63) to solve the 1-dimensional Schrödinger equations for the reference potentials. The MQDT $\boldsymbol{Y}$ matrix is then obtained by matching to the log-derivative matrix extracted from the coupled-channels propagation at a distance r_{match}. In this chapter all

MQDT calculations use the reference potential

$$U_i^{\mathrm{ref}}(r) = V_0(r) + \frac{\hbar^2 L_i(L_i+1)}{2\mu r^2} + E_i^{\infty}, \tag{8.1}$$

where $V_0(r)$ is the isotropic part of the interaction potential and L_i is the partial-wave quantum number for channel i. Figure 8.1 shows the reference potential for the ground and first rotational excited state. The reference potential contains a hard wall at $r = r_i^{\mathrm{wall}}$, so that $U_i^{\mathrm{ref}}(r) = \infty$ for $r < r_i^{\mathrm{wall}}$. In the chapter we choose $r_i^{\mathrm{wall}} = 4.0$ Å. This reference potential has been shown to produce quantitatively accurate results for Mg+NH (104, 106). All channels with $n \geq 2$ are treated as strongly closed and thus not included in the MQDT part of the calculation, but are included in the log-derivative propagation.

8.3 Results and discussion

In a magnetic field, the lowest Li-NH threshold ($n = 0, s_{\mathrm{NH}} = 1, s_{\mathrm{Li}} = \frac{1}{2}$) splits into 6 Zeeman sublevels, as shown in figure 8.2. We consider collisions between Li atoms and NH molecules that are both in their magnetically trappable low-field-seeking states, $m_{s,\mathrm{Li}} = +1/2$ and $m_{s,\mathrm{NH}} = +1$. This corresponds to the highest of the 6 thresholds.

Figure 8.3 shows the variation of the representative element $Y_{1,-1,-1,-\frac{1}{2},7,4}$ as a function of the matching distance and energy when the θ_i values are chosen to make all Y_{ii} matrix elements zero at collision energy $E_{\mathrm{ref}} = 0.5$ K. The basis set used for this Figure included all functions up to $n_{\mathrm{max}} = 3$ and $L_{\mathrm{max}} = 8$. This unconverged basis set was used due to the substantial computational cost

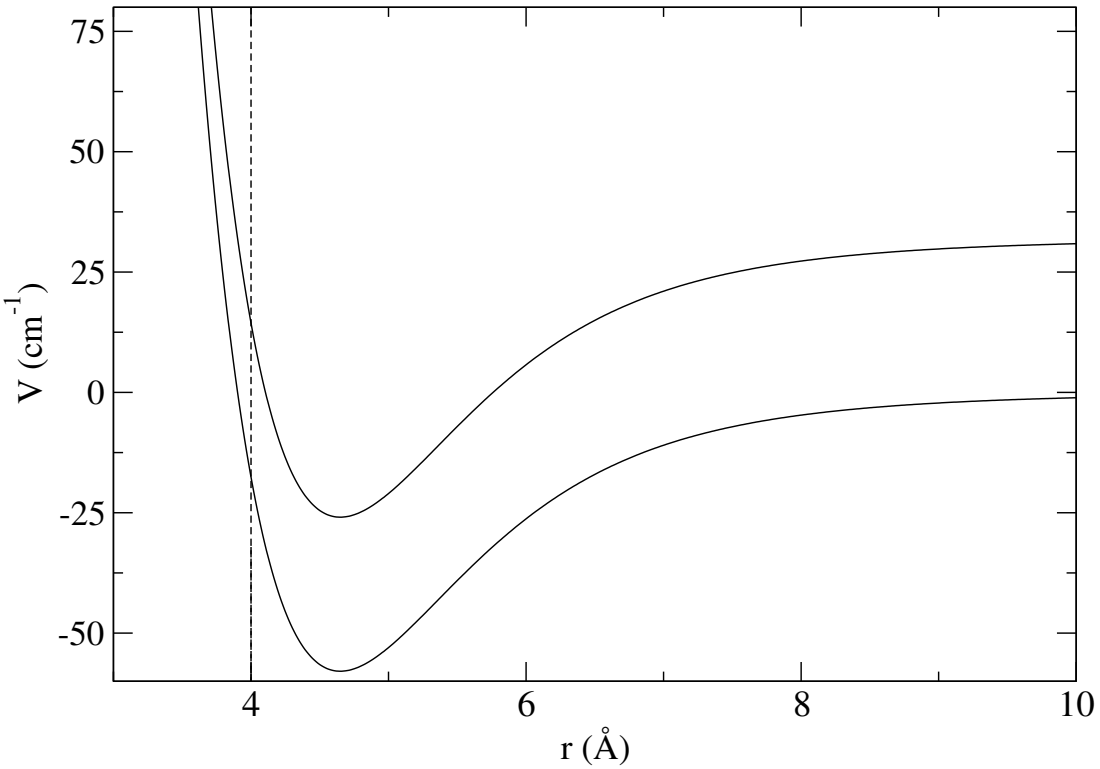

Figure 8.1: The V_0 reference potentials for Li + NH. The first rotational excited state is also shown ($n = 1$). The hard wall at $r = 4.0$ Å is shown as a vertical dashed line.

of performing a full coupled-channels calculation at every energy in the Figure. The outer turning point of the $n = 1$ reference potential is at 6.1 Å, and it may be seen that, for values of r_{match} inside this, the $\boldsymbol{Y}$ matrix is pole-free over many K. However, MQDT with such small values of r_{match} does not produce accurate results because it neglects all channel couplings that exist outside r_{match}. When $r_{\mathrm{match}} > 6.1$ Å, poles start to enter the $\boldsymbol{Y}$ matrix in the energy range of interest. As r_{match} increases further, the resonant structure reduces the pole-free region even further.

A contour plot such as Fig. 8.3 requires coupled-channels calculations at every energy, and producing it thus sacrifices most of the computational savings that

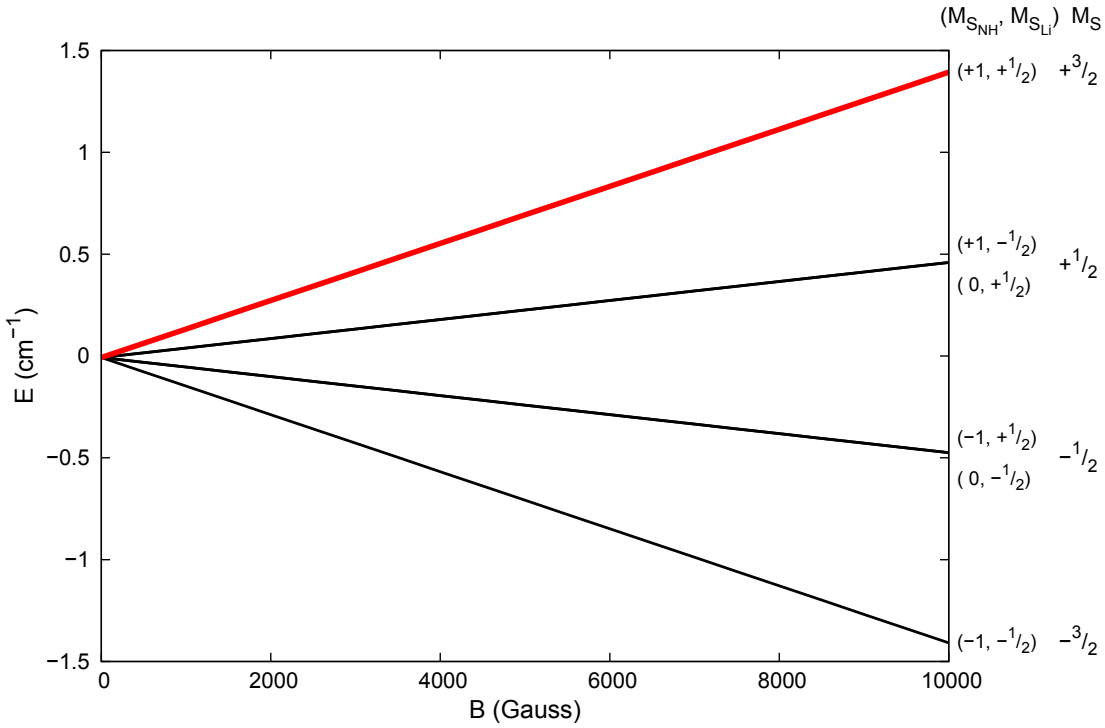

Figure 8.2: Li(^{2}S)+NH($^3\Sigma$) thresholds as a function of magnetic field. The spin-stretched state is shown in red. Image taken from (114).

MQDT is designed to achieve. In addition, we need a procedure for choosing the phases θ_i that will guarantee a large pole-free region for *any* choice of r_{match}. In the remainder of this chapter, we perform calculations at only a single value of $r_{\text{match}} = 6.5$ Å, deliberately chosen to be in a region where Fig. 8.3 shows that there are poles in $\boldsymbol{Y}$ at inconveniently low energies. In addition, the remaining calculations use a converged basis set including all functions up to $n_{\text{max}} = 8$ and $L_{\text{max}} = 8$.

For a closed channel that is capable of supporting resonances, the dependence of Y_{ii} on θ_i is

$$Y_{ii}(E) = \tan(\theta_i + \delta_i(E)), \tag{8.2}$$

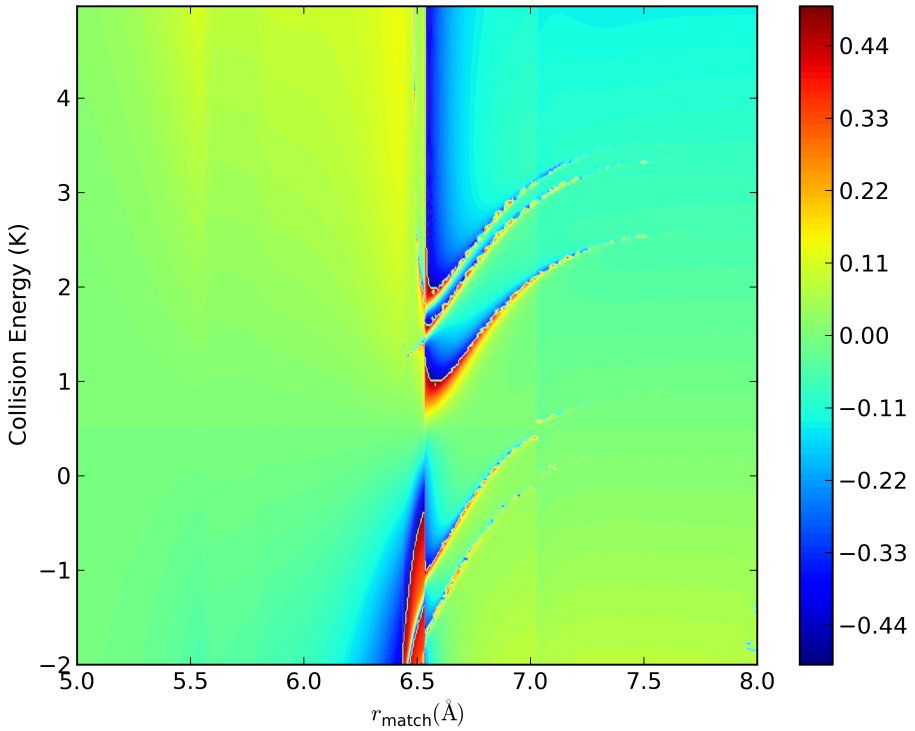

Figure 8.3: $\arctan Y_{ii}/\pi$ for a single representative diagonal $\boldsymbol{Y}$ matrix element, as a function of energy and r_{match} at for θ_i set so that $Y_{ii} = 0$ in all channels for $B = 10$ G and collision energy 0.5 K.

where the energy-dependent phase shift $\delta_i(E)$ is given by a Breit-Wigner form

$$\delta_i(E) = \bar{\delta}_i(E) + \arctan\left(\frac{E - E_i^{\mathrm{res}}}{\Gamma_i}\right), \tag{8.3}$$

where $\bar{\delta}_i$ is a slowly varying (non-resonant) background term. The resonant part of this function is shown in the lower panel of Fig. 8.4, for values of the parameters appropriate to one of the channels in Li+NH. It may be seen that choosing a value of θ_i that makes Y_{ii} zero (shown by the dashed vertical line) does not guarantee a large pole-free region in the case where E is close to E_{res}. A much better choice in

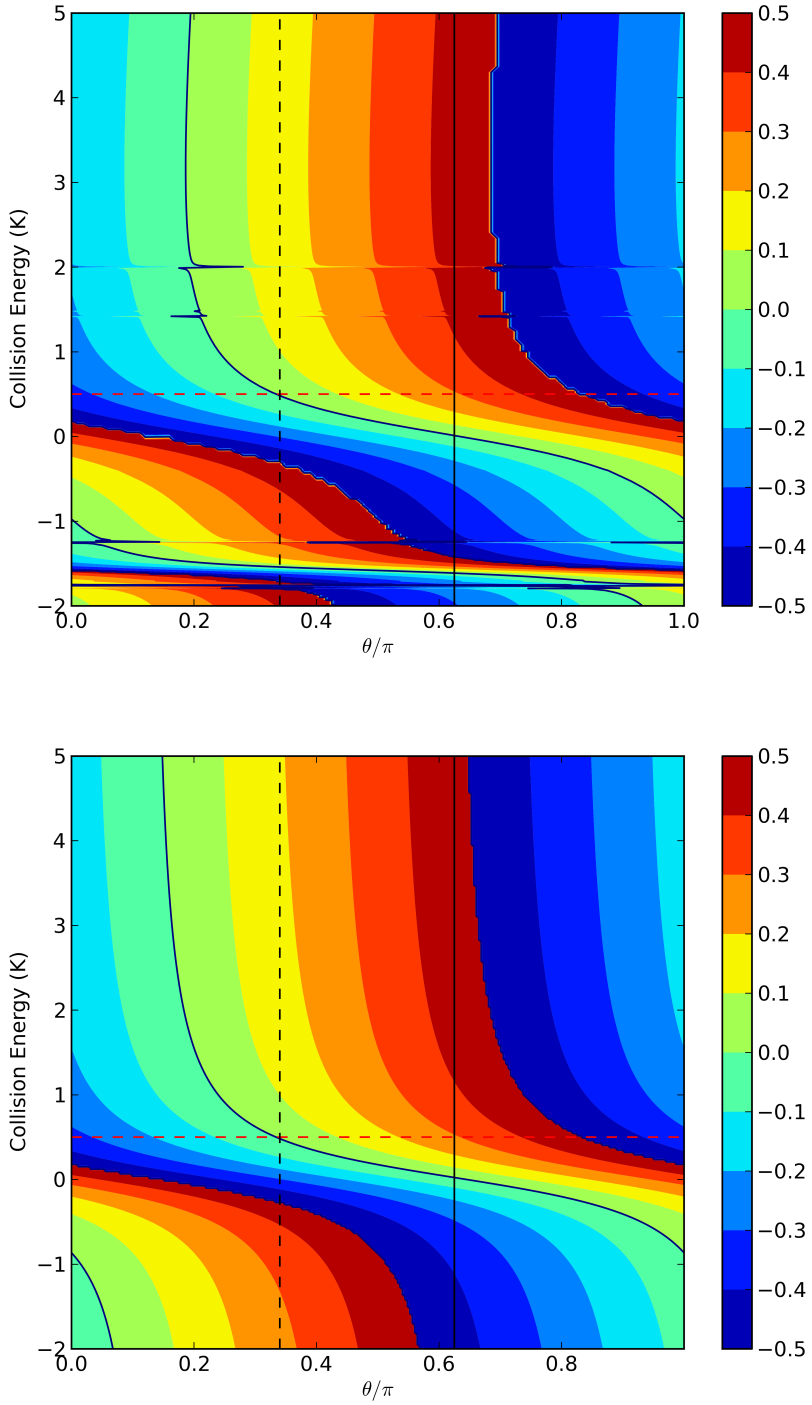

Figure 8.4: Lower panel: $\arctan Y_{ii}/\pi$ as a function of energy and θ_i for a single channel as given by equations 8.2 and 8.3. Upper panel: $\arctan Y_{ii}/\pi$ from coupled-channels calculations at $B = 10$ G for a single diagonal element, $Y_{1,-1,-1,-\frac{1}{2},7,4}$, with θ_j for all other channels set so that $Y_{jj} = 0$.

this case is to set θ_i to the value shown by the solid vertical line. In the following we will show how this can be achieved.

A basic problem of MQDT in coupled-channel problems is that a pole in $\boldsymbol{Y}$ that originates in *any* channel causes a pole in *every* channel. We refer to this as the *contamination* of one channel by another. The upper panel of Figure 8.4 shows $\arctan Y_{ii}/\pi$ for the single matrix element, $Y_{1,-1,-1,-\frac{1}{2},7,4}$, obtained from coupled-channels calculations as a function of θ_i and collision energy E. The phases θ_i in all other channels j are set to the values that produce $Y_{jj} = 0$ at 0.5 K. The broad horizontal sweep around 0.41 K arises from a resonance in channel i, while the narrower sweeps at -1.5 K, -1.2 K, 1.5 K and 2.1 K are poles due to contamination from other channels. Setting Y_{jj} to zero in all these other channels has shifted these contamination effects to energies either above about 2 K or below -1 K, leaving a region of about 3 K uncontaminated by other channels. For the specific circumstances shown in Figure 8.4, it is seen that choosing θ_i so that $Y_{ii} = 0$ results in a pole in Y_{ii} itself at 1.1 K, whereas a choice of $\theta_i = 0.6\pi$ would produce a much larger pole-free range, limited only by poles due to contamination effects in other channels. If an improved choice of θ_i can also be obtained for these contamination poles then there is clearly the prospect of achieving a much improved pole-free region.

The pole structure in channel i when uncontaminated by other channels is given by equations 8.2 and 8.3. We can thus use these to obtain a better choice of θ_i, but in order to do so we first need Γ_i, δ_i and E_i^{res}. To obtain them we first perform an optimization as in ref. (106), rotating the reference functions until $Y_{ii} = 0$ in all channels at energy E_{ref}. This provides at least a small region where Y_{ii} is uncontaminated by poles in other regions. We then carry out coupled-

channels calculations at 2 additional energies near E_{ref}, and use equations 8.2 and 8.3 to obtain the three parameters $\bar{\delta}_i$, E_i^{res} and Γ_i numerically, neglecting the slow variation of $\bar{\delta}_i$ with E. The optimum pole-free region for this channel is then achieved by setting $\theta_i = \bar{\delta}_i$.

The pole-free region for the entire $\boldsymbol{Y}$ matrix is optimized by applying this procedure in all channels where there is resonant structure close to the reference energy. We first calculate the numerical second derivative of the diagonal matrix elements Y_{ii} with respect to energy. We then select the channel with the largest second derivative, apply the procedure described above, and use the new set of phases to recalculate the three $\boldsymbol{Y}$ matrices. If this reduces $\sum_i |d^2Y_{ii}/dE^2|$ then we accept the new value of θ_i. We then loop over the closed channels in this manner until there is no channel for which changing θ_i to $\bar{\delta}_i$ reduces $\sum_i |d^2Y_{ii}/dE^2|$. This is an inexpensive procedure, as it uses the same 3 coupled-channels calculations as before. Only the closed channels need to be included in the loop since only these channels have resonance structure.

Figure 8.5 compares the final matrix elements Y_{ii} in all channels, obtained with the two optimization schemes. The dashed red lines show the result of choosing θ_i so that Y_{ii} is zero in every channel, while the solid black lines show the result of optimizing θ_i as described above. Both calculations use $r_{\mathrm{match}} = 6.5$ Å and optimize θ_i at 0.5 K and 10 G. It may be seen that the taking account of closed-channel resonances in optimizing θ_i greatly increases the pole-free range of $\boldsymbol{Y}$. Furthermore, it produces $\boldsymbol{Y}$ matrix elements that are considerably more linear between 0 and 1 K and may thus be interpolated more accurately.

Figure 8.6 compares diagonal T-matrix elements $|T_{ii}|^2$ (where $T_{ij} = \delta_{ij} - S_{ij}$) obtained from full coupled-channels calculations with those from the MQDT

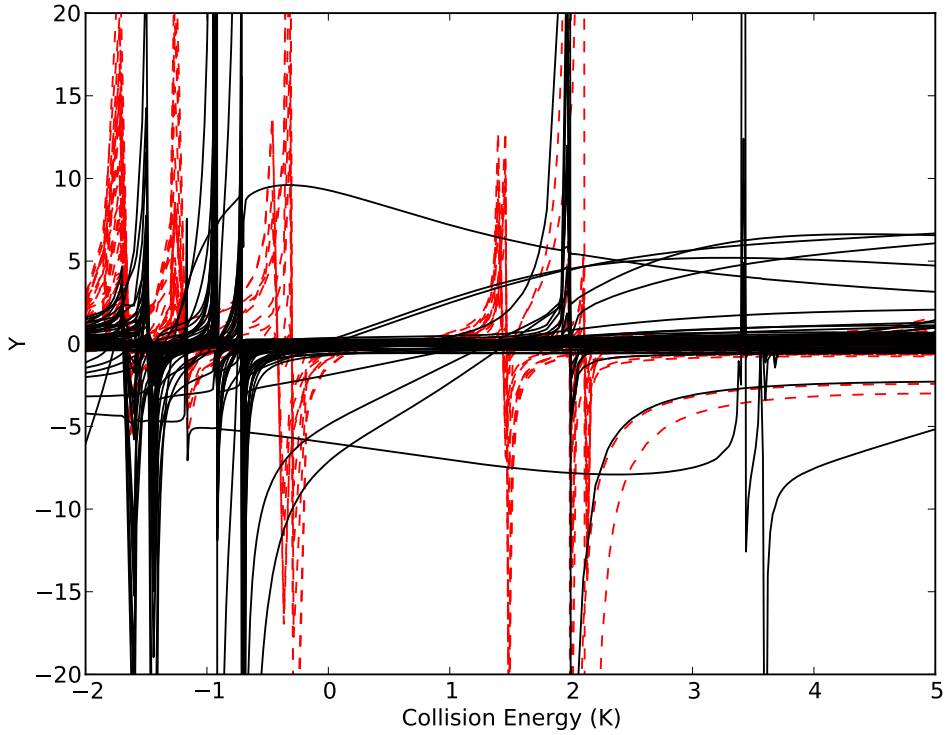

Figure 8.5: Lower panel: Y_{ii} as a function of energy for all channels, with all phases θ_i optimized as described in ref. (104) (dashed red lines) or using equations 8.2 and 8.3 (solid black lines).

method using interpolation. The MQDT results were obtained by interpolating (and extrapolating) $\boldsymbol{Y}$ quadratically using 3 points separated by 0.1 K around 0.5 K. The MQDT results obtained by interpolation are very similar to the full coupled-channels results except around the resonance features at $E \approx 0.7$ K, and even there they show a resonance of the correct shape with a slight shift in energy. The interpolated result could be improved simply by performing coupled-channels calculations to obtain $\boldsymbol{Y}$ at one or two extra energies across the range, to allow for a higher-order interpolation, or by using a linear interpolation over a smaller energy range.

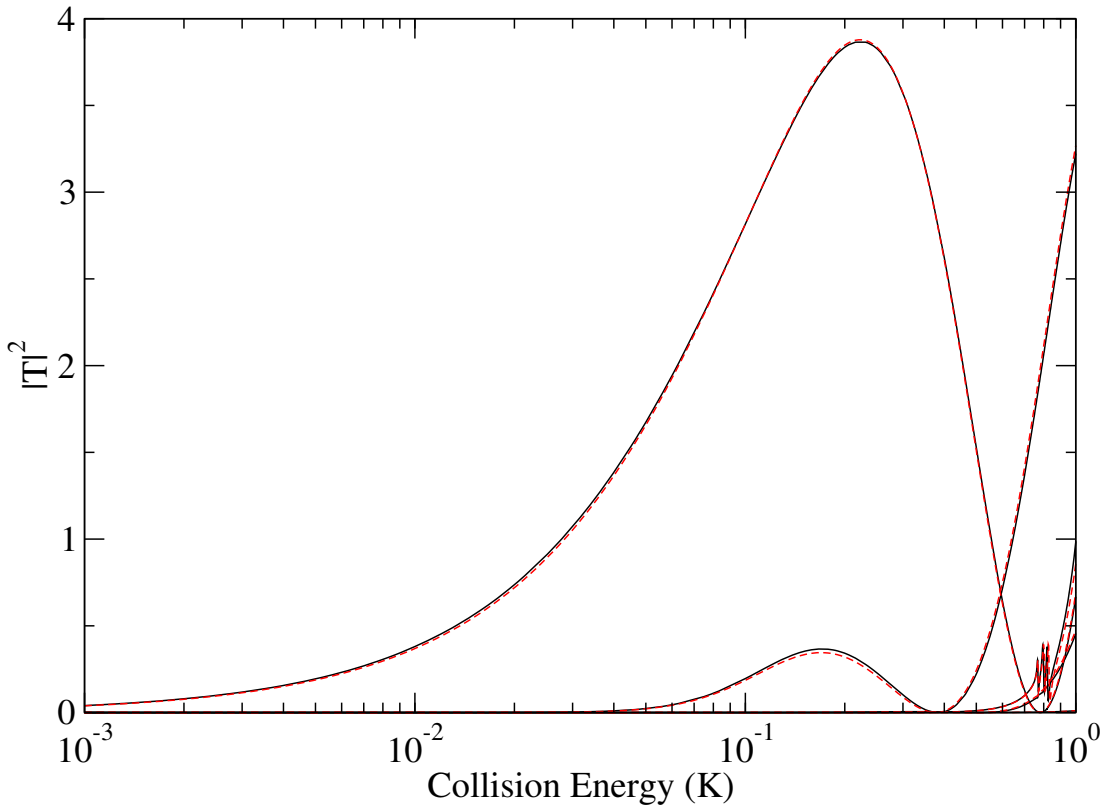

Figure 8.6: The squares of diagonal T-matrix elements T_{m_j}, L, M_L in the incoming channels for $m_j = +1$ and $L = 0$, 2 and 4 at $B = 10$ G, obtained from full coupled-channels calculations (solid, black) and MQDT using optimized reference functions for $r_{\mathrm{match}} = 6.5$ Å both with (dot-dash, blue) and without (dashed, red) interpolation.

8.4 Conclusions

It has been shown that Multichannel Quantum Defect Theory (MQDT) can provide an efficient computational method for low-energy molecular collisions, for the highly anisotropic Li + NH system.

The advantage of MQDT over the full coupled-channels method is predicated on the ability to obtain a Y matrix which can be interpolated over a wide range of fields and energies. Once such a Y matrix has been obtained the cost of calculations at additional energies and fields varies only linearly with the number

of channels N, not as N^3 as for full coupled-channels calculations. The $\boldsymbol{Y}$ matrix is defined to encapsulate all the collision dynamics that occurs inside a matching distance r_{match}. It is thus desirable to be able to match at as large a distance of r as possible. However molecular collisions often necessitate matching in the classically forbidden region for some channels where resonant features cause poles in the $\boldsymbol{Y}$ matrix, preventing interpolation over a wide range of energies. It has been shown how to define a $\boldsymbol{Y}$ matrix, taking resonant structure into account, such that it is amenable to interpolation over a wide range of energies.

MQDT with $\boldsymbol{Y}$ matrices optimized to take account of resonant structure thus provides a very promising alternative to full coupled-channels calculations for cold molecular collisions, particularly when fine scans over collision energy and magnetic field are required.

Chapter 9

Conclusions and further work

9.1 Conclusions

It has been shown that Multichannel Quantum Defect Theory (MQDT) can be applied to low-energy molecular collisions in applied magnetic fields. MQDT provides a matrix $\boldsymbol{Y}$, defined at a distance r_{match} at relatively short range, which encapsulates all the short-range dynamics of the system. For the two molecular systems Mg+NH and Li+NH, we have shown that MQDT can provide numerical results that are in quantitative agreement with full coupled-channel calculations if the MQDT reference functions are defined appropriately.

The effect of different choices of reference potential and values of r_{match} has been investigated. For molecular collisions, the most satisfactory procedure is to perform the matching at fairly short range (inside 7 Å) and use a reference potential that is defined to be the same as the true diagonal potential in the incoming channel.

Molecular collisions often necessitate matching in the classically forbidden re-

gion for some channels, where there is a significant likelihood of resonant features within the energy range that prevent simple interpolation of $\boldsymbol{Y}$. We have shown how a disposable parameter of MQDT, the phase of the short-range reference functions, may be chosen to make the MQDT $\boldsymbol{Y}$ matrix smooth and pole-free over a wide range of energy and field. This smooth variation allows the $\boldsymbol{Y}$ matrix to be evaluated from coupled-channel calculations at a few values of the energy and field and then to be obtained by interpolation at intermediate values. This allows very considerable computational efficiencies, because the expensive calculation to obtain $\boldsymbol{Y}$ needs to be carried out at only one or a few combinations of collision energy and field. The remaining calculations to obtain scattering properties on a fine grid of energies and fields are then computationally inexpensive, varying only linearly with the number of channels N. Full coupled-channel calculations, by contrast, scale as N^3.

MQDT is a promising alternative to full coupled-channel calculations for cold atom-molecule collisions, particularly when fine scans over collision energy and magnetic field are required.

9.2 Further work

In this thesis MQDT has been successfully applied to low-energy atom-molecule collisions in magnetic fields, however the range of collisions of interest to cold molecule studies is broad. MQDT posses an in-built flexibility which has led to its successful application to a wide variety of scattering problems as diverse as negative ion photodetachment (74), near-threshold predissociation of diatomic molecules (71, 75) and predissociation of atom-diatom Van der Waals complexes

(76, 77). More recently it has been applied to ultracold collisions between pairs of neutral atoms (78, 79, 80, 81, 82), between atoms and ions (83, 84), and between highly reactive molecules (85, 86, 87). This flexibility makes MQDT a promising method to attack the diverse range of computationally challenging problems being posed by cold molecule studies, such as molecule-molecule collisions, collisions in electric and/or magnetic fields and collision including nuclear hyperfine effects.

In this work all calculations have been performed using a diabatic basis. However, $\boldsymbol{Y}$ matrices corresponding to calculations in different bases may be more amenable to interpolation. The other obvious choice to investigate is the adiabatic basis, which is closer to the physical problem and thus could lead to a superior $\boldsymbol{Y}$ matrix for interpolating.

The method demonstrated here speeds up calculations when repeated calculations are required over a fine grid of energy and field, but does not remove the need to perform at least one expensive $\mathcal{O}(N^3)$ propagation. A large number of channels is required for collisions in an applied field because the total angular momentum J is not a good quantum number. In field-free scattering these large sets of coupled equations can be factorized neatly into smaller blocks for each J. An approximate $\boldsymbol{Y}$ matrix could thus be obtained from field-free calculations and then MQDT used for the long-range to give the correct threshold behavior. At very low energies, small splittings between molecular energy levels become important. This makes it necessary to include fine details of molecular energy level patterns, such as tunneling and nuclear hyperfine splitting (51, 54). The extra degrees of freedom require additional basis functions; in particular, including nuclear spins can multiply the number of equations by a substantial factor (sometimes 100 or more). This large multiplication in the number of channels

could be avoided by obtaining a $\boldsymbol{Y}$ matrix from a calculation without nuclear hyperfine included, then using MQDT to account correctly for the long-range form for each hyperfine threshold.

MQDT only includes scattering dynamics within r_{match} and so couplings that persist to long range are incompletely accounted for. Such couplings could be included using the Born approximation or the distorted wave Born approximation as demonstrated, for the intermolecular spin-spin interaction, in collisions of NH-NH (115).

In addition to the opportunities afforded by the flexibility of MQDT there are also a number of methods which could be beneficially combined with MQDT. Despite the total angular momentum, J, not being a good quantum number in fields, using the total angular momentum representation in the body-fixed coordinated frame has been shown to produce accurate $\boldsymbol{S}$ matrices (116). This approach has been successfully demonstrated for atom-molecule collisions in a magnetic field (117), atom-molecule collisions in a electric field (118) and molecule-molecule collisions in a magnetic field (119). Combining this approach with the MQDT approach developed here is a very promising approach to attacking currently intractable problems posed by ultracold molecular collision studies.

An iterative approach could be used to refine an approximate $\boldsymbol{S}$ matrix, following the method developed by Thomas (120). This method has the advantage that it can be applied to a single column of the $\boldsymbol{S}$ matrix, which is often precisely what we are interested in in cold molecule studies.

In this thesis methods have been developed to extend the range of interpolation by moving poles in the $\boldsymbol{Y}$ matrix. These poles are, however, a geometric feature rather then a necessary physical one, and are a consequence of our match-

ing to the log-derivative matrix. In doing so we obtain the ratio of the coefficients of the reference functions f_i and g_i, which is ∞ when the contribution from f_i is 0. These coefficients could be obtained separately by matching to the wavefunction and its derivative, avoiding the problems caused by poles in the $\boldsymbol{Y}$ matrix. This approach would, however, require the explicit propagation of the wavefunction which is less stable than the corresponding log-derivative propagation.

References

[1] N. S. Ginsberg, S. R. Garner, and L. V. Hau. Coherent control of optical information with matter wave dynamics. *Nature*, 445(7128):623–626 2007.

[2] H. Onnes. Further experiments with liquid helium D - On the change of the electrical resistance of pure metals at very low temperatures, etc V The disappearance of the resistance of mercury. *KNAW Proceedings*, 14(Part 1):113–115, 1911.

[3] H. G. Smith and J. O. Wilhelm. Superconductivity. *Rev. Mod. Phys.*, 7:237–271 1935.

[4] P. Kapitza. Viscosity of liquid helium below the lambda-point. *Nature*, 141:74 1938.

[5] J. Allen and A. Misener. Flow of liquid helium II. *Nature*, 141:75 1938.

[6] K. K. Darrow. Helium the superfluid. *Rev. Mod. Phys.*, 12:257–266 1940.

[7] S. N. Bose. Plancks law and light quantum hypothesis. *Z. Phys.*, 26:178, 1924.

[8] A. Einstein. Quantum theory of ideal gases. *Sitzungsber. Preuss. Akad. Wiss.*, page 18, 1925.

[9] M. H. Anderson, J. R. Ensher, M. R. Matthews, C. E. Wieman, and E. A. Cornell. Observation of bose-einstein condensation in a dilute atomic vapor. *Science*, 269(5221):198–201 1995.

[10] K. B. Davis, M.-O. Mewes, M. R. Andrews, N. J. van Druten, D. S. Durfee, D. M. Kurn, and W. Ketterle. Bose-einstein condensation in a gas of sodium atoms. *Phys. Rev. Lett.*, 75(22):3969–3973, 1995.

[11] M. Greiner, C. A. Regal, and D. S. Jin. Emergence of a molecular bose-einstein condensate from a fermi gas. *Nature*, 426(6966):537–540 2003.

[12] S. Jochim, M. Bartenstein, A. Altmeyer, G. Hendl, S. Riedl, C. Chin, J. Hecker Denschlag, and R. Grimm. Bose-einstein condensation of molecules. *Science*, 302(5653):2101–2103 2003.

[13] S. S. Kondov, W. R. McGehee, J. J. Zirbel, and B. DeMarco. Three-dimensional anderson localization of ultracold matter. *Science*, 334(6052):66–68, 2011.

[14] W. Hofstetter, J. I. Cirac, P. Zoller, E. Demler, and M. D. Lukin. High-temperature superfluidity of fermionic atoms in optical lattices. *Phys. Rev. Lett.*, 89:220407 2002.

[15] M. W. Zwierlein, J. R. Abo-Shaeer, A. Schirotzek, C. H. Schunck, and W. Ketterle. Vortices and superfluidity in a strongly interacting fermi gas. *Nature*, 435(7045):1047–1051 2005.

[16] L. D. Carr, D. DeMille, R. V. Krems, and J. Ye. Cold and ultracold

molecules: science, technology and applications. *New J. Phys.*, 11:055049, 2009.

[17] G. Quéméner and P. S. Julienne. Ultracold molecules under control! *Chemical Reviews*, 112(9):4949–5011, 2012.

[18] J. Doyle, B. Friedrich, R. V. Krems, and F. Masnou-Seeuws. Quo vadis, cold molecules? *Eur. Phys. J. D*, 31(2):149–164 2004.

[19] R. V. Krems. Molecules near absolute zero and external field control of atomic and molecular dynamics. *Int. Rev. Phys. Chem.*, 24(1):99–118 2005.

[20] B. Friedrich and J. M. Doyle. Why are cold molecules so hot? *ChemPhysChem*, 10(4):604–623, 2009.

[21] J. M. Hutson and P. Soldán. Molecule formation in ultracold atomic gases. *Int. Rev. Phys. Chem.*, 25(4):497–526, 2006.

[22] K.-K. Ni, S. Ospelkaus, M. H. G. de Miranda, A. Pe'er, B. Neyenhuis, J. J. Zirbel, S. Kotochigova, P. S. Julienne, D. S. Jin, and J. Ye. A high phase-space-density gas of polar molecules in the rovibrational ground state. *Science*, 322:231, 2008.

[23] S. Ospelkaus, K.-K. Ni, D. Wang, M. H. G. de Miranda, B. Neyenhuis, G. Quéméner, P. S. Julienne, J. L. Bohn, D. S. Jin, and J. Ye. Quantum-state controlled chemical reactions of ultracold KRb molecules. *Science*, 327:853–857, 2010.

[24] J. G. Danzl, M. J. Mark, E. Haller, M. Gustavsson, R. Hart, J. Aldegunde, J. M. Hutson, and H.-C. Nägerl. An ultracold, high-density sample of

rovibronic ground-state molecules in an optical lattice. *Nature Phys.*, 6:265–270, 2010.

[25] R. V. Krems. Cold controlled chemistry. *Phys. Chem. Chem. Phys.*, 10(28):4079–4092, 2008.

[26] E. R. Hudson, H. J. Lewandowski, B. C. Sawyer, and J. Ye. Cold molecule spectroscopy for constraining the evolution of the fine structure constant. *Phys. Rev. Lett.*, 96(14):143004 2006.

[27] J. J. Hudson, B. E. Sauer, M. R. Tarbutt, and E. A. Hinds. Measurement of the electron electric dipole moment using YbF molecules. *Phys. Rev. Lett.*, 89(2):023003, 2002.

[28] C. Chin, V. V. Flambaum, and M. G. Kozlov. Ultracold molecules: new probes on the variation of fundamental constants. *New J. Phys.*, 11(5):055048, 2009.

[29] H. L. Bethlem and W. Ubachs. Testing the time-invariance of fundamental constants using microwave spectroscopy on cold diatomic radicals. *Faraday Discuss.*, 142:25–36, 2009.

[30] M. L. Wall and L. D. Carr. Emergent timescales in entangled quantum dynamics of ultracold molecules in optical lattices. *New J. Phys.*, 11:055027, 2009.

[31] D. DeMille. Quantum computation with trapped polar molecules. *Phys. Rev. Lett.*, 88(6):067901 2002.

[32] M. Nielsen and I. Chuang. *Quantum Computation and Quantum Information*. Cambridge Series on Information and the Natural Sciences. Cambridge University Press, 2000.

[33] S. Chu. The manipulation of neutral particles. *Rev. Mod. Phys.*, 70(3):685–706 1998.

[34] C. N. Cohen-Tannoudji. Manipulating atoms with photons. *Rev. Mod. Phys.*, 70(3):707–719 1998.

[35] W. D. Phillips. Nobel lecture: Laser cooling and trapping of neutral atoms. *Rev. Mod. Phys.*, 70(3):721–741 1998.

[36] E. S. Shuman, J. F. Barry, and D. DeMille. Laser cooling of a diatomic molecule. *Nature*, 467(7317):820–823 2010.

[37] C. A. Regal, C. Ticknor, J. L. Bohn, and D. S. Jin. Creation of ultracold molecules from a fermi gas of atoms. *Nature*, 424(6944):47–50 2003.

[38] J. Herbig, T. Kraemer, M. Mark, T. Weber, C. Chin, H. C. Nägerl, and R. Grimm. Preparation of a pure molecular quantum gas. *Science*, 301(5639):1510–1513 2003.

[39] J. Cubizolles, T. Bourdel, S. J. J. M. F. Kokkelmans, G. V. Shlyapnikov, and C. Salomon. Production of long-lived ultracold Li_2 molecules from a fermi gas. *Phys. Rev. Lett.*, 91(24):240401 2003.

[40] K. E. Strecker, G. B. Partridge, and R. G. Hulet. Conversion of an atomic fermi gas to a long-lived molecular bose gas. *Phys. Rev. Lett.*, 91(8):080406 2003.

[41] H. Feshbach. Unified theory of nuclear reactions. *Ann. Phys.*, 5(4):357–390, 1958.

[42] A. Fioretti, D. Comparat, A. Crubellier, O. Dulieu, F. Masnou-Seeuws, and P. Pillet. Formation of cold Cs_2 molecules through photoassociation. *Phys. Rev. Lett.*, 80(20):4402–4405 1998.

[43] J. Ulmanis, J. Deiglmayr, M. Repp, R. Wester, and M. Weidemüller. Ultracold molecules formed by photoassociation: Heteronuclear dimers, inelastic collisions, and interactions with ultrashort laser pulses. *Chemical Reviews*, 112(9):4890–4927, 2012.

[44] J. G. Danzl, E. Haller, M. Gustavsson, M. J. Mark, R. Hart, N. Bouloufa, O. Dulieu, H. Ritsch, and H.-C. Nägerl. Quantum gas of deeply bound ground state molecules. *Science*, 321:1062–1066, 2008.

[45] F. Lang, K. Winkler, C. Strauss, R. Grimm, and J. Hecker Denschlag. Ultracold molecules in the rovibrational ground state. *Phys. Rev. Lett.*, 101:133005, 2008.

[46] J. D. Weinstein, R. deCarvalho, T. Guillet, B. Friedrich, and J. M. Doyle. Magnetic trapping of calcium monohydride molecules at millikelvin temperatures. *Nature*, 395(6698):148–150 1998.

[47] H. L. Bethlem and G. Meijer. Production and application of translationally cold molecules. *Int. Rev. Phys. Chem.*, 22(1):73–128 2003.

[48] E. Narevicius, A. Libson, C. G. Parthey, I. Chavez, J. Narevicius, U. Even,

and M. G. Raizen. Stopping supersonic oxygen with a series of pulsed electromagnetic coils: A molecular coilgun. *Phys. Rev. A*, 77:051401 2008.

[49] P. Soldán and J. M. Hutson. Interaction of NH($^3\Sigma^-$) molecules with rubidium atoms: Implications for sympathetic cooling and the formation of extremely polar molecules. *Phys. Rev. Lett.*, 92(16):163202 2004.

[50] R. deCarvalho, J. Kim, J. D. Weinstein, J. M. Doyle, B. Friedrich, T. Guillet, and D. Patterson. Buffer-gas loaded magnetic traps for atoms and molecules: A primer. *Eur. Phys. J. D*, 7:289–309, 1999.

[51] M. Lara, J. L. Bohn, D. E. Potter, P. Soldán, and J. M. Hutson. Cold collisions of OH and Rb. I: the field-free case. *Phys. Rev. A*, 75:012704, 2007.

[52] P. S. Żuchowski and J. M. Hutson. Low-energy collisions of NH_3 and ND_3 with ultracold Rb atoms. *Phys. Rev. A*, 79:062708, 2009.

[53] S. Tokunaga, W. Skomorowski, R. Moszynski, P. S. Żuchowski, J. M. Hutson, E. A. Hinds, and M. R. Tarbutt. Prospects for sympathetic cooling of molecules in electrostatic, ac and microwave traps. *Eur. Phys. J. D*, 65:141–149, 2011.

[54] M. L. González-Martínez and J. M. Hutson. Effect of hyperfine interactions on ultracold molecular collisions: NH($^3\Sigma^-$) with Mg(^1S) in magnetic fields. *Phys. Rev. A*, 84:052706, 2011.

[55] A. Volpi and J. L. Bohn. Magnetic-field effects in ultracold molecular collisions. *Phys. Rev. A*, 65(5):052712 2002.

[56] R. V. Krems and A. Dalgarno. Quantum-mechanical theory of atom-molecule and molecular collisions in a magnetic field: Spin depolarization. *J. Chem. Phys.*, 120(5):2296–2307 2004.

[57] A. M. Arthurs and A. Dalgarno. The theory of scattering by a rigid rotator. *Proc. Roy. Soc., Ser. A*, 256(1287):540–551, 1960.

[58] R. G. Gordon. A new method for constructing wavefunctions for bound states and scattering. *J. Chem. Phys.*, 51:14, 1969.

[59] B. R. Johnson. Multichannel log-derivative method for scattering calculations. *J. Comput. Phys.*, 13(3):445–449, 1973.

[60] M. L. González-Martínez and J. M. Hutson. Ultracold atom-molecule collisions and bound states in magnetic fields: zero-energy Feshbach resonances in He-NH ($^3\Sigma^-$). *Phys. Rev. A*, 75:022702, 2007.

[61] M. Abramowitz and I. A. Stegun. *Handbook of Mathematical Functions*. Dover, New York, 9th dover printing edition, 1964.

[62] B. Numerov. *Publs. Observatoire Central Astrophys. Russ.*, 2:188, 1933.

[63] B. R. Johnson. New numerical methods applied to solving one-dimensional eigenvalue problem. *J. Chem. Phys.*, 67:4086, 1977.

[64] J. M. Blatt. Practical points concerning the solution of the schrödinger equation. *Journal of Computational Physics*, 1(3):382 – 396, 1967.

[65] D. E. Manolopoulos. An improved log-derivative method for inelastic scattering. *J. Chem. Phys.*, 85(11):6425–6429 1986.

[66] M. H. Alexander and D. E. Manolopoulos. A stable linear reference potential algorithm for solution of the quantum close-coupled equations in molecular scattering theory. *J. Chem. Phys.*, 86:2044, 1987.

[67] M. J. Seaton. Quantum defect theory I. general formulation. *Proc. Phys. Soc. London*, 88:801, 1966.

[68] M. J. Seaton. Quantum defect theory. *Rep. Prog. Phys.*, 46(2):167, 1983.

[69] C. H. Greene, U. Fano, and G. Strinati. General form of the quantum-defect theory. *Phys. Rev. A*, 19:1485–1509, 1979.

[70] C. H. Greene, A. R. P. Rau, and U. Fano. General form of the quantum-defect theory. II. *Phys. Rev. A*, 26(5):2441–2459, 1982.

[71] F. H. Mies. A multichannel quantum defect analysis of diatomic predissociation and inelastic atomic scattering. *J. Chem. Phys.*, 80(6):2514–2525, 1984.

[72] B. Yoo and C. H. Greene. Implementation of the quantum-defect theory for arbitrary long-range potentials. *Phys. Rev. A*, 34:1635, 1986.

[73] B. Gao. General form of the quantum-defect theory for $-1/r^{\alpha}$ type of potentials with $\alpha > 2$. *Phys. Rev. A*, 78:012702, 2008.

[74] S. Watanabe and C. H. Greene. Atomic polarizability in negative-ion photodetachment. *Phys. Rev. A*, 22(1):158–169, 1980.

[75] F. H. Mies and P. S. Julienne. A multichannel quantum defect analysis of two-state couplings in diatomic molecules. *J. Chem. Phys.*, 80(6):2526–2536, 1984.

[76] M. Raoult and G. G. Balint-Kurti. Application of generalized quantum-defect theory to photodissociation processes: Predissociation of Ar-H_2. *Phys. Rev. Lett.*, 61(22):2538–2541, 1988.

[77] M. Raoult and G. G. Balint-Kurti. Frame transformation theory for heavy particle scattering: Application to the rotational predissociation of Ar-H_2. *J. Chem. Phys.*, 93:6508, 1990.

[78] P. S. Julienne and F. H. Mies. Collisions of ultracold trapped atoms. *J. Opt. Soc. Am. B*, 6(11):2257–2269, 1989.

[79] J. P. Burke, J. L. Bohn, B. D. Esry, and C. H. Greene. Prospects for mixed-isotope bose-einstein condensates in rubidium. *Phys. Rev. Lett.*, 80(10):2097, 1998.

[80] F. H. Mies and M. Raoult. Analysis of threshold effects in ultracold atomic collisions. *Phys. Rev. A*, 62(1):012708, 2000.

[81] M. Raoult and F. H. Mies. Feshbach resonance in atomic binary collisions in the wigner threshold law regime. *Phys. Rev. A*, 70(1):012710, 2004.

[82] B. Gao, E. Tiesinga, C. J. Williams, and P. S. Julienne. Multichannel quantum-defect theory for slow atomic collisions. *Phys. Rev. A*, 72(4):042719, 2005.

[83] Z. Idziaszek, T. Calarco, P. S. Julienne, and A. Simoni. Quantum theory of ultracold atom-ion collisions. *Phys. Rev. A*, 79(1):010702, 2009.

[84] B. Gao. Universal properties in ultracold ion-atom interactions. *Phys. Rev. Lett.*, 104(21):213201 2010.

[85] Z. Idziaszek and P. S. Julienne. Universal rate constants for reactive collisions of ultracold molecules. *Phys. Rev. Lett.*, 104:113202, 2010.

[86] Z. Idziaszek, G. Quéméner, J. L. Bohn, and P. S. Julienne. Simple quantum model of ultracold polar molecule collisions. *Phys. Rev. A*, 82:020703, 2010.

[87] B. Gao. Universal model for exoergic bimolecular reactions and inelastic processes. *Phys. Rev. Lett.*, 105(26):263203 2010.

[88] J. M. Vogels, R. S. Freeland, C. C. Tsai, B. J. Verhaar, and D. J. Heinzen. Coupled singlet-triplet analysis of two-color cold-atom photoassociation spectra. *Phys. Rev. A*, 61(4):043407, 2000.

[89] B. Gao. Angular-momentum-insensitive quantum-defect theory for diatomic systems. *Phys. Rev. A*, 64(1):010701, 2001.

[90] B. Gao. Solutions of the schrödinger equation for an attractive $1/r^6$ potential. *Phys. Rev. A*, 58(3):1728–1734, 1998.

[91] B. Gao. Quantum-defect theory of atomic collisions and molecular vibration spectra. *Phys. Rev. A*, 58(5):4222–4225, 1998.

[92] B. Gao. Analytic description of atomic interaction at ultracold temperatures: The case of a single channel. *Phys. Rev. A*, 80(1):012702, 2009.

[93] P. S. Julienne and B. Gao. Simple theoretical models for resonant cold atom interactions. *AIP Conference Proceedings*, 869:261–268, 2006.

[94] C. R. Brazier, R. S. Ram, and P. F. Bernath. Fourier transform spectroscopy of the $A^3\Pi$-$X^3\Sigma^-$ transition of NH. *J. Mol. Spectrosc.*, 120(2):381–402 1986.

[95] M. Mizushima. *Theory of Rotating Diatomic Molecules*. Wiley, New York, 1975.

[96] J. M. Brown and A. Carrington. *Rotational Spectroscopy of Diatomic Molecules*, page 646. Cambridge University Press, Cambridge, 2003.

[97] P. Soldán, P. S. Żuchowski, and J. M. Hutson. Prospects for sympathetic cooling of polar molecules: NH with alkali-metal and alkaline-earth atoms – a new hope. *Faraday Discuss.*, 142:191–201, 2009.

[98] A. O. G. Wallis and J. M. Hutson. Production of ultracold NH molecules by sympathetic cooling with Mg. *Phys. Rev. Lett.*, 103:183201, 2009.

[99] A. O. G. Wallis. Ultracold molecules: The effect of electromagnetic fields. *PhD Thesis, Durham University*, 2010.

[100] J. M. Hutson and S. Green. MOLSCAT computer program, version 14. distributed by Collaborative Computational Project No. 6 of the UK Engineering and Physical Sciences Research Council, 2006.

[101] J. M. Hutson. BOUND computer program, version 5. distributed by Collaborative Computational Project No. 6 of the UK Engineering and Physical Sciences Research Council, 1993.

[102] I. Fourré and M. Raoult. Application of generalized quantum defect theory to van der waals complex bound state calculations. *J. Chem. Phys.*, 101:8709–8725, 1994.

[103] K. M. Jones, E. Tiesinga, P. D. Lett, and P. S. Julienne. Ultracold photoas-

sociation spectroscopy: long-range molecules and atomic scattering. *Rev. Mod. Phys.*, 78:483–535 2006.

[104] J. F. E. Croft, A. O. G. Wallis, J. M. Hutson, and P. S. Julienne. Multichannel quantum defect theory for cold molecular collisions. *Phys. Rev. A*, 84:043703, 2011.

[105] M. J. Seaton. Quantum defect theory I. general formulation. *Proc. Phys. Soc.*, 88(4):801–814, 1966.

[106] J. F. E. Croft, J. M. Hutson, and P. S. Julienne. Optimized multichannel quantum defect theory for cold molecular collisions. *Phys. Rev. A*, 86:022711 2012.

[107] J. M. Hutson and S. Green. MOLSCAT computer program, version 14. distributed by Collaborative Computational Project No. 6 of the UK Engineering and Physical Sciences Research Council, 1994.

[108] A. Giusti-Suzor and U. Fano. Alternative parameters of channel interactions. I. symmetry analysis of the two-channel coupling. *J. Phys. B*, 17(2):215, 1984.

[109] A. Giusti-Suzor and U. Fano. Alternative parameters of channel interactions. II. a hamiltonian model. *J. Phys. B*, 17(21):4267, 1984.

[110] A. Giusti-Suzor and U. Fano. Alternative parameters of channel interactions. III. note on a narrow band in the Ba J=2 spectrum. *J. Phys. B*, 17(21):4277, 1984.

[111] W. E. Cooke and C. L. Cromer. Multichannel quantum-defect theory and an equivalent N-level system. *Phys. Rev. A*, 32 1985.

[112] W. Eissner, H. Nussbaumer, H. E. Saraph, and M. J. Seaton. Resonances in cross sections for excitation of forbidden lines in O_2+. *J. Phys. B*, 2(3):341, 1969.

[113] R. Ossni, O. Dulieu, and M. Raoult. Optimization of generalized multichannel quantum defect reference functions for feshbach resonance characterization. *J. Phys. B*, 42(18):185202, 2009.

[114] A. O. G. Wallis, E. J. J. Longdon, P. S. Żuchowski, and J. M. Hutson. The prospects of sympathetic cooling of NH molecules with Li atoms. *Eur. Phys. J. D*, 65:151–160, 2011.

[115] L. M. C. Janssen, A. van der Avoird, and G. C. Groenenboom. On the role of the magnetic dipolar interaction in cold and ultracold collisions: numerical and analytical results for NH($^3\Sigma^-$)+NH($^3\Sigma^-$). *Eur. Phys. J. D*, 65(1-2):177–187 2011.

[116] T. V. Tscherbul and A. Dalgarno. Quantum theory of molecular collisions in a magnetic field: Efficient calculations based on the total angular momentum representation. *J. Chem. Phys.*, 133(18) 2010.

[117] T. V. Tscherbul, J. Klos, and A. A. Buchachenko. Ultracold spin-polarized mixtures of $^2\Sigma$ molecules with S-state atoms: Collisional stability and implications for sympathetic cooling. *Phys. Rev. A*, 84(4) 2011.

[118] T. V. Tscherbul. Total-angular-momentum representation for atom-molecule collisions in electric fields. *Phys. Rev. A*, 85(5) 2012.

[119] Y. V. Suleimanov, T. V. Tscherbul, and R. V. Krems. Efficient method for quantum calculations of molecule-molecule scattering properties in a magnetic field. *J. Chem. Phys.*, 137(2) 2012.

[120] L. Thomas. Solution of the coupled equations of inelastic atom-moleucle scattering for a single initial state .2. use of nondiagonal matrix green-functions. *J. Chem. Phys.*, 76(10):4925–4935, 1982.